

# JUNO 水相实验中的太阳中微子观 测研究

**Research on Solar Neutrino Observation  
with JUNO Water Phase**

(申请清华大学理学博士学位论文)

培养单位：工程物理系

学 科：物理学

研 究 生：翁 俊

指 导 教 师：续 本 达 副教授

二〇二五年九月



# **Research on Solar Neutrino Observation with JUNO Water Phase**

Dissertation submitted to  
**Tsinghua University**  
in partial fulfillment of the requirement  
for the degree of  
**Doctor of Philosophy**  
in  
**Physics**

by

**Weng Jun**

Dissertation Supervisor: Associate Professor, Xu Benda

**September, 2025**

**TABLE OF CONTENTS**

TABLE OF CONTENTS .....	D
CHAPTER 1 INTRODUCTION.....	1
CHAPTER 2 THE JUNO DETECTOR .....	2
CHAPTER 3 THE PMT CALIBRATION IN WATER PHASE .....	3
3.1 The gain calibration .....	3
3.1.1 The traditional mixed Gaussian model.....	3
3.1.2 The difficulty of MCP-PMT gain calibration .....	6
3.1.3 Gamma-Distributed SER charges .....	6
3.1.4 Jumbo Charges through Extra Multiplication .....	7
3.1.5 Parameter Extraction from Data.....	17
3.1.6 Gamma-Tweedie model for MCP-PMT .....	20
3.1.7 The gain distribution of PMTs.....	21
3.2 The dark count rate.....	23
3.3 The timing calibration .....	25
3.4 The Photon Detection Efficiency .....	25
CHAPTER 4 THE RECONSTRUCTION FOR THE WATER-PHASE .....	27
4.1 The Likelihood function .....	27
4.2 Response of the water-phase detector .....	28
4.2.1 The Cherenkov emission profile.....	28
4.2.2 The calculation of direct light .....	31
4.2.3 The prediction of indirect light based on direct light.....	37
4.2.4 The timing response.....	39
4.2.5 The DCR in reconstruction .....	40
4.2.6 Use MCMC for extremization .....	41
4.2.7 The preliminary reconstruction.....	41
4.3 The parameters definition .....	42
4.3.1 The energy related parameters.....	42
4.3.2 The parameters for reconstruction quality .....	42
4.4 The performance of reconstruction in simulation .....	45

---

## TABLE OF CONTENTS

---

CHAPTER 5 THE SOURCE CALIBRATION IN WATER PHASE.....	47
5.0.1 The calibration information .....	47
5.1 JUNO's low-energy threshold in water phase.....	47
5.1.1 The reconstruction of the prompt signals .....	47
5.1.2 The search for delayed signals .....	53
5.1.3 The low-energy threshold in water phase .....	54
5.2 The neutron capture detecting ability of JUNO in water phase .....	56
5.2.1 The maximum neutron detection efficiency .....	58
5.2.2 The highest neutron detection signal-to-noise ratio .....	61
5.2.3 The balance between neutron detection efficiency and SNR .....	64
CHAPTER 6 THE MEASUREMENT OF SPALLATION NEUTRON YIELD IN WA- TER PHASE .....	65
6.1 The reconstruction of muon track .....	65
6.2 The search for spallation neutron.....	65
6.3 The spallation neutron yield calculation.....	70
6.3.1 Cross check using water-pool reconstructed muon .....	71
6.3.2 The prediction of $Y_n$ in water .....	72
CHAPTER 7 THE OBSERVATION OF SOLAR NEUTRINO.....	75
7.1 Searching for Solar neutrino signals .....	75
7.1.1 The dataset .....	75
7.1.2 The selection in preliminary reconstruction .....	75
7.1.3 The energy selection .....	76
7.1.4 The position selection.....	77
7.1.5 The muon spallation cut .....	77
7.1.6 The observation of solar neutrino signals .....	79
REFERENCES .....	80



## **CHAPTER 1 INTRODUCTION**

## CHAPTER 2 THE JUNO DETECTOR

The Jiangmen Underground Neutrino Observatory (JUNO) is a multipurpose neutrino experiment under construction in southern China. The primary scientific objective of JUNO is to determine the neutrino mass ordering and precisely measure neutrino oscillation parameters by detecting reactor antineutrinos from the Yangjiang and Taishan nuclear power plants, located approximately 53 km from the JUNO site. The JUNO detector consists of a central detector (CD) containing 20 kilotons of liquid scintillator (LS), a water Cherenkov detector (WCD) serving as a cosmic muon veto, and a top tracker (TT) for additional muon tracking. The CD is housed within a large acrylic sphere with a diameter of 35.4 m, which is further enclosed by a stainless steel lattice structure. The WCD surrounds the CD and is filled with 35 kilotons of ultrapure water, while the TT is positioned above the WCD. The entire detector assembly is situated approximately 700 m underground, equivalent to 1800 m of water overburden, to mitigate cosmic ray interference.

# CHAPTER 3 THE PMT CALIBRATION IN WATER PHASE

For the search of solar neutrinos in water phase, calibrating and understanding the detector is of crucial importance. First and foremost is to understand the behavior of photomultiplier tubes (PMTs). That is, we need to understand how PMTs convert the received photons into basic information for reconstruction. We need to extract from the output information of PMTs how many photons are captured and when they are captured. This requires systematic characterization of key parameters including the PMT timing response, gain stability, linearity, noise levels, and single-photon detection capability. Such calibration is also critical for achieving the high-precision energy resolution and vertex reconstruction necessary for JUNO’s physics goals during LS phase, particularly in the determination of neutrino mass ordering. In this chapter, we will investigate the performance characteristics of PMTs in the water phase.

## 3.1 The gain calibration

### 3.1.1 The traditional mixed Gaussian model

As outlined in foundational studies<sup>[1]</sup>, a PMT’s operational core comprises three functional stages:

- photon-to-electron conversion at the photocathode interface
- multi-stage electron amplification
- charge collection at the anode terminal

Photon arrivals at the photocathode exhibit Poissonian stochasticity. Through probabilistic photoelectric conversion<sup>[2]</sup>, a subset of incident photons liberates photoelectrons (PEs) that propagate toward the amplification region. These sequential conversion mechanisms constitute Bernoulli processes characterized by quantum efficiency (QE) and collection efficiency (CE) parameters, ultimately generating Poisson-distributed number of PEs ( $n_{\text{PE}}$ ) values within defined temporal windows<sup>[3]</sup>.

Electron multiplication relies fundamentally on secondary electron emission (SEE) dynamics. Primary particle impacts (electrons/ions) on solid targets induce secondary electron liberation<sup>[4]</sup>, with the emission yield (SEY,  $\delta$ ) quantifying the mean secondary-to-primary ratio. The energy spectrum of emitted secondaries ( $d\delta/dE$ ) exhibits dependence on:

- primary particle kinetic energy
- impact angle
- material composition<sup>[5]</sup>.

Early SEY characterization employed electron bombardment methodologies: Bruining and Boer<sup>[6]</sup>, Ushio et al.<sup>[7]</sup>, and Jokela et al.<sup>[8]</sup> obtained current-mode measurements, while Olano and Montero<sup>[9]</sup> derived  $d\delta/dE$  distributions for polymeric substrates (Kapton/Teflon/Ultem) via charge accumulation analysis, observing significantly attenuated secondary electron energies relative to primaries. These bulk-material SEE properties have subsequently informed PMT amplification models<sup>[10-11]</sup>.

Critically, the discrete electron regime governing PMT operation necessitates careful reinterpretation of current-mode SEY data when modeling single-electron amplification in pulse-mode scenarios.

Within the multiplier amplification process, a PE initiates an electron cascade, culminating in anode capture within several hundred picoseconds. The initial energy of PEs generated at the photocathode is approximately 1 eV<sup>[12]</sup>. The incident PE energy at the multiplier is governed primarily by the photocathode-multiplier potential difference. Consequently, the amplifier delivers nearly identical gain for all PEs.

Owing to the central limit theorem, the total charge collected at the anode typically follows a Gaussian distribution. Thus, the single electron response (SER) charge distribution PDF is defined as  $f_{\mathcal{N}}(Q; Q_1, \sigma_1^2)$ , where  $Q_1$  denotes the mean charge and  $\sigma_1$  its standard deviation. The PE count  $n_{\text{PE}}$  adheres to a Poisson distribution  $P_{\pi}(n_{\text{PE}}; \lambda)$ , with  $\lambda$  representing the expected count under specific light intensity. Post-amplification, the total charge distribution  $f(Q)$  constitutes a convolution of these distributions<sup>[3]</sup>. Background processes manifest in two categories:

- A low-charge Gaussian  $\mathcal{N}(0, \sigma_0^2)$  occurring without photocathode PE emission.
- Discrete events (e.g., thermoemission or light-induced noise) with probability  $w$ , following an exponential distribution  $\text{Exp}(\alpha)$  ( $\alpha$ : exponential decay rate).

Given the background charge distribution  $f_b(Q)$ , the overall charge distribution is expressed in Eq. 3.1:

$$\begin{aligned}
 f(Q) = & P_\pi(n_{\text{PE}} = 0; \lambda) f_b(Q) + \sum_{n_{\text{PE}}=1}^{\infty} P_\pi(n_{\text{PE}}; \lambda) f_{\mathcal{N}}(Q; n_{\text{PE}}Q_1, n_{\text{PE}}\sigma_1^2) \\
 \approx & \left\{ \frac{(1-w)}{\sigma_0 \sqrt{2\pi}} \exp\left(-\frac{Q^2}{2\sigma_0^2}\right) + w\theta(Q) \times \alpha \exp(-\alpha Q) \right\} e^{-\lambda} \\
 & + \sum_{n_{\text{PE}}=1}^{\infty} \frac{\lambda^{n_{\text{PE}}} e^{-\lambda}}{n_{\text{PE}}!} \times \frac{1}{\sigma_1 \sqrt{2\pi n_{\text{PE}}}} \times \exp\left(-\frac{(Q - n_{\text{PE}}Q_1)^2}{2n_{\text{PE}}\sigma_1^2}\right)
 \end{aligned} \quad (3.1)$$

The Heaviside function  $\theta(Q)$  serves as a critical component in this model. For  $\lambda < 0.1$ , the probability of detecting two or more PEs falls below one-tenth of the single-PE observation probability. Consequently, the charge distribution exhibits only two distinct peaks: the pedestal peak at  $Q = 0$  and the single-PE peak at  $Q = Q_1$ , as demonstrated by the blue histogram in Fig 3.1. An approximate SER charge spectrum can thus be derived through pedestal suppression via targeted cuts. To standardize gain calibration across different PMTs, we normalize the SER charge spectrum by dividing all charge values by  $Q_1$ , yielding the dimensionless ratio  $Q/Q_1$ .

### 3.1.1.1 The newly developed MCP-PMT

In contrast to traditional Dynode-PMTs that typically employ large-scale dynode chains for electron multiplication, MCP-PMTs implement microchannel plates (MCPs) as their amplification components. These devices are actively utilized or planned for deployment in major scientific initiatives, including neutrino experiments such as JUNO<sup>[13]</sup> and the Jinping Neutrino Experiment (JNE)<sup>[14]</sup>, collider facilities like the Belle II TOP detector<sup>[15]</sup> and PANDA's DIRC Cherenkov detector at FAIR<sup>[16]</sup>, as well as cosmic ray observatories exemplified by the Large High Altitude Air Shower Observatory<sup>[17]</sup>. Early operational challenges stemmed from ion feedback-induced photocathode degradation, imposing lifetime constraints on MCP-PMTs<sup>[18]</sup>.

Atomic layer deposition (ALD) technology<sup>[10]</sup> has been successfully implemented to address this longevity limitation during MCP-PMT manufacturing<sup>[19]</sup>. Research by Chen et al. established that applying high SEY materials (e.g., Al<sub>2</sub>O<sub>3</sub>) via ALD onto the first MCP's input electrode significantly increases secondary electron collection probability<sup>[2]</sup>. This enhancement elevates collection efficiency (CE) to nearly 100 %, thereby circumventing restrictions imposed by the MCP's geometric open-area ratio. Subsequent advancements by Cao et al. and Zhang et al. further optimized this technique through

composite  $\text{Al}_2\text{O}_3$ -MgO layers<sup>[20-21]</sup>, achieving measurable improvements in gain stability, single-electron resolution, and peak-to-valley ratios for MCP-PMTs<sup>[11]</sup>.

### 3.1.2 The difficulty of MCP-PMT gain calibration

In the mass testing of the 20-inch MCP-PMTs at Pan-Asia, a “long tail” in the SER charge distribution was found<sup>[22]</sup>. Similar structure was found in the performance tests to evaluate the 8-inch high-CE MCP-PMT by the Jinping Neutrino Experiment (JNE)<sup>[14]</sup> and we define those as ”jumbo charge”. Orlov et al.<sup>[23]</sup> reported that the pulse height distribution of the high-CE MCP-PMTs had a non-Gaussian long-tail structure. Zhang et al.<sup>[24]</sup> used the charge model in Eq. (3.1) for the jumbo charges and recommended an extra gain calibration. Yang et al.<sup>[25]</sup> conducted a voltage-division experiment to reveal that the MCP gain for the low-energy electrons is significantly smaller than that for the high-energy ones. Thus, the MCP gain for the secondaries differs from that for the PEs entering the channels directly. The SER charge model in Eq. (3.1) is no longer sufficient to accurately calibrate this type of PMT. Understanding the origin of the jumbo charges is necessary for an appropriate SER charge calibration. Considering the structural similarity of the MCP-PMT in the JNE and the fact that the 8-inch PMT is more flexible compared to the 20-inch PMT in JUNO, we take the MCP-PMT in JNE as the research object and extend the results to the 20-inch PMT in JUNO.

### 3.1.3 Gamma-Distributed SER charges

Electron multiplication at dynodes or MCP channels follows an approximately Poisson-distributed process<sup>[26]</sup>. Successive multiplications constitute a cascaded Poisson sequence<sup>[1]</sup>, representing a branching process<sup>[27]</sup> that poses significant challenges for analytical computation. Woodward<sup>[28]</sup> observed that the SER charge spectrum exhibits an intermediate morphology between Poissonian and Gaussian distributions. To characterize electron multiplication in PMTs, particularly accounting for dynode surface non-uniformity, Prescott<sup>[29]</sup> proposed a cascaded Polya distribution. Kalousis<sup>[30-31]</sup> subsequently approximated the Polya distribution as a Gamma form for PMT calibration, demonstrating enhanced performance compared to the Gaussian model in Eq. (3.1).

We adopt a Gamma distribution  $\Gamma(\alpha, \beta)$  parametrized by scale factor  $\alpha$  and rate factor  $\beta$  (Eq. (3.2)), thereby eliminating the nonphysical sub-zero tail inherent in Gaussian

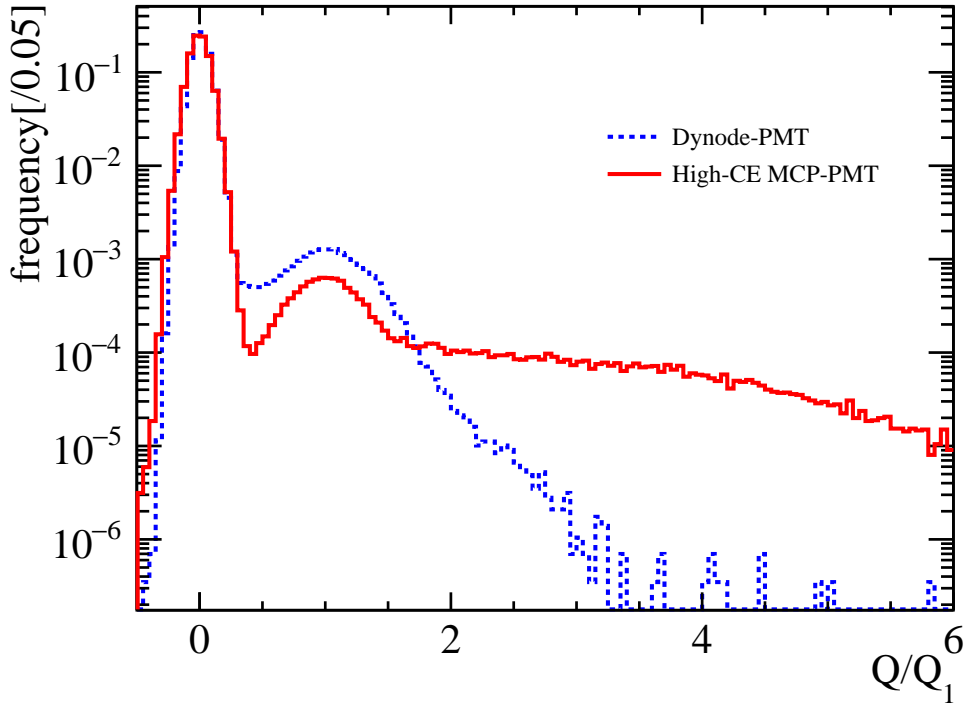


Figure 3.1 The charge spectrum of the high-CE MCP-PMT GDB-6082 (red) and a dynode-PMT (blue)<sup>[14]</sup>. The blue histogram consists of the pedestal  $Q = 0$  and the principal peak of  $Q = Q_1$ , while the red histogram includes jumbo charges.

representations.

$$f_{\Gamma}(x; \alpha, \beta) = \frac{x^{\alpha-1} e^{-\beta x} \beta^{\alpha}}{\Gamma(\alpha)} \quad \text{for } x > 0 \quad \alpha, \beta > 0 \quad (3.2)$$

where  $\Gamma(\alpha)$  is the Gamma function. A Gamma distribution is uniquely determined by its expectation value  $\alpha/\beta = Q_1$  and variance  $\alpha/\beta^2 = \sigma_1^2$ , which can be converted into the Gaussian counterparts in Eq. (3.1). The charge spectrum based on the Gamma distribution is,

$$f(Q) = P_{\pi}(n_{\text{PE}} = 0; \lambda) f_b(Q) + \sum_{n_{\text{PE}}=1}^{\infty} P_{\pi}(n_{\text{PE}}; \lambda) f_{\Gamma}(Q; n_{\text{PE}}\alpha, \beta). \quad (3.3)$$

### 3.1.4 Jumbo Charges through Extra Multiplication

SEE has garnered significant research interest due to its critical role in vacuum electronic devices. Bruining's seminal monograph *Physics and Applications of Secondary Electron Emission*<sup>[32]</sup> consolidated foundational methodologies, empirical findings, and technological implementations of SEE. Baroody<sup>[33]</sup> proposed a metallic SEE theory postulating that incident primary electrons interact exclusively with conduction-band free electrons, neglecting energy-dependent variations in secondary emission. Dekker et al.<sup>[34]</sup>

established a quantum theory addressing Coulomb interactions between incident primaries and lattice electrons. Wolff<sup>[35]</sup> developed the cascade theory describing secondary electron diffusion, energy dissipation, and multiplication within metals.

Under isotropic conditions for incident and backscattered electrons, Kanaya et al.<sup>[36]</sup> derived SEY values for insulators incorporating ionization potentials, valence electron contributions, backscattering coefficients, and free-electron density effects. Vaughan<sup>[37]</sup> empirically expressed SEY as a function of impact energy and direction (the Vaughan model), enabling computational implementation. Furman and Pivi<sup>[5]</sup> created a mathematically self-consistent Monte Carlo framework (the Furman model) characterizing SEE from solid surfaces. This model probabilistically describes secondary emission statistics, treating emitted electron energies as independent, identically distributed random variables governed by material properties and primary energies.

Whereas early theoretical models emphasized mechanistic explanations, the Vaughan and Furman frameworks prioritize Monte Carlo computational methods. The Furman model achieves superior physical consistency and experimental agreement, justifying its selection for precision applications requiring adaptable parameters and enhanced accuracy.

### 3.1.4.1 Furman probabilistic model

In the Furman model<sup>[5]</sup>, there are three kinds of secondary electrons, as shown in Fig. 3.2. The first type is the backscattered electrons emitted through elastic scattering on

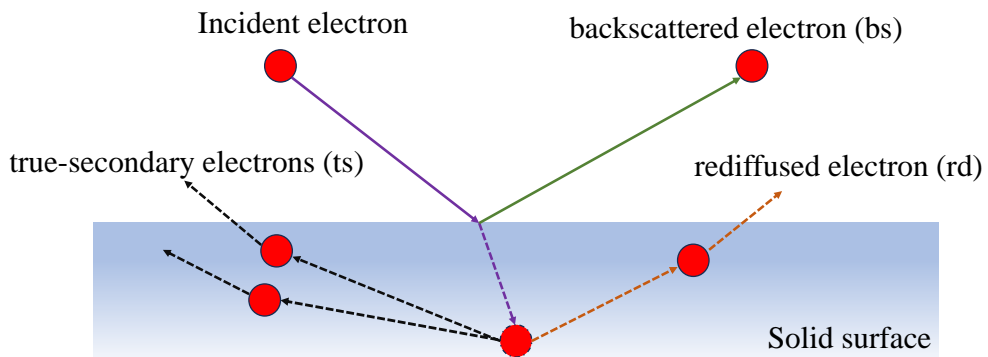


Figure 3.2 The three kinds of secondary electrons in Furman model.

the surface of the target material. Its energy distribution  $d\delta_{bs}/dE$  is given by Eq. (3.4), where  $\delta_{bs}$  represents the yield of backscattered electrons, the Heaviside function  $\theta(E)$

ensures that  $E < E_0$ ,  $E_0$  is the energy of the incident primary electrons,  $\theta_0$  is the incident angle, and  $\sigma_{\text{bs}}$  is the adjustable standard deviation.

$$\frac{d\delta_{\text{bs}}}{dE} = \theta(E)\theta(E_0 - E)\delta_{\text{bs}}(E_0, \theta_0) \frac{2 \exp(-(E - E_0)^2/2\sigma_{\text{bs}}^2)}{\sqrt{2\pi}\sigma_{\text{bs}} \operatorname{erf}(E_0/\sqrt{2}\sigma_{\text{bs}})} \quad (3.4)$$

After penetrating the target material, some electrons are inelastically scattered by atoms and reflected out, forming the second type of electrons. Leonard referred to the bending of the electron trajectory as “diffusion”, and in German literature, a 90° turn of the trajectory is called “Rückdiffusion” in German literature<sup>[32]</sup>. Furman and Pivi<sup>[5]</sup> adopted this convention and named them *rediffused electrons*. The energy distribution of rediffused electrons is defined by Eq. (3.5), where  $\delta_{\text{rd}}$  is the yield of rediffused electrons and  $q$  is an adjustable parameter.

$$\frac{d\delta_{\text{rd}}}{dE} = \theta(E)\theta(E_0 - E)\delta_{\text{rd}}(E_0, \theta_0) \frac{(q + 1)E^q}{E_0^{q+1}} \quad (3.5)$$

The last but the most important kind is the true-secondary electrons. Upon deeper penetration of electrons into the target material, intricate physical processes ensue, generating one or more secondaries. This is the process of multiplying electrons. The spectrum is defined as Eq. (3.6).

$$\begin{aligned} \frac{d\delta_{\text{ts}}}{dE} = & \sum_{n=1}^{\infty} \frac{n P_{n,\text{ts}}(n; \delta_{\text{ts}}(E_0, \theta_0)) (E/\epsilon_n)^{p_n-1} e^{-E/\epsilon_n}}{\epsilon_n \Gamma(p_n) \Upsilon(np_n, E_0/\epsilon_n)} \\ & \times \Upsilon[(n-1)p_n, (E_0 - E)/\epsilon_n] \end{aligned} \quad (3.6)$$

where  $\delta_{\text{ts}}(E_0, \theta_0)$  is the yield of the true-secondary electrons when the incident energy is  $E_0$  and the incident angle is  $\theta_0$ ,  $\epsilon_n > 0$  and  $p_n > 0$  are the phenomenological parameters.  $\gamma(z, x)$  is the incomplete gamma function, and  $\Upsilon(z, x) = \gamma(z, x)/\Gamma(z)$  is the normalized form satisfying  $\Upsilon(0, x) = 1$ .  $n$ , the number of the true-secondary electrons, follows a Poisson distribution ( $\delta_{\text{ts}}(E_0, \theta_0)$ ).  $P_{n,\text{ts}}$  is its probability mass function.

where  $\delta_{\text{ts}}(E_0, \theta_0)$  represents the yield of the true-secondary electrons under the conditions that  $E_0$  is the incident energy and  $\theta_0$  is the incident angle. Here,  $\epsilon_n > 0$  and  $p_n > 0$  work as the phenomenological parameters.  $\gamma(z, x)$  is the incomplete gamma function, and its normalized form is  $\Upsilon(z, x) = \gamma(z, x)/\Gamma(z)$  satisfying  $\Upsilon(0, x) = 1$ . The number of the true-secondary electrons  $n$  follows the Poisson distribution ( $\delta_{\text{ts}}(E_0, \theta_0)$ ), and its probability mass function is  $P_{n,\text{ts}}$ .

As illustrated in Fig. 3.3, the parameters<sup>[11]</sup> are setted as  $\delta_{\text{bs}} = 0.05$ ,  $\delta_{\text{rd}} = 0.5$ ,

$\delta_{ts} = 5$ ,  $\theta_0 = 0^\circ$  and  $E_0 = 650$  eV. The total spectrum is the sum of three components.

$$\frac{d\delta}{dE} = \frac{d\delta_{bs}}{dE} + \frac{d\delta_{rd}}{dE} + \frac{d\delta_{ts}}{dE} \quad (3.7)$$

When the incident energy  $E_0$  is around 650 eV, the energies of the secondaries are usually less than 100 eV .

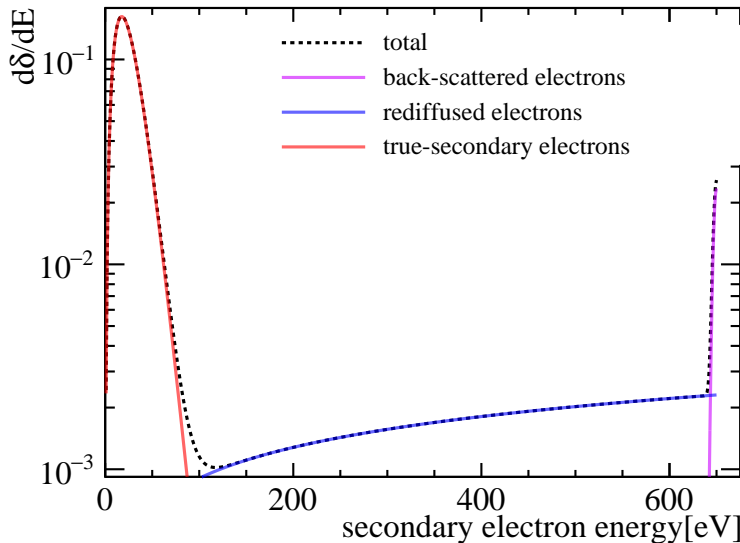


Figure 3.3 The total energy spectrum of the secondary electrons when the incident energy is 650 eV. The violet, blue, and red lines represent  $d\delta_{bs}/dE$ ,  $d\delta_{rd}/dE$ , and  $d\delta_{ts}/dE$ , respectively. The black dashed line is  $d\delta/dE$ .

### 3.1.4.2 An extra multiplication mode

A Chevron stack of two MCPs as the electron multiplier is used in the MCP-PMT both in JUNO and JNE. As shown in Fig. 3.4, through the ALD technology, an  $\text{Al}_2\text{O}_3$ - $\text{MgO}$ - $\text{Al}_2\text{O}_3$  layer<sup>[21]</sup> is deposited not only on the channel surface of the lead glass body but also on the entrance electrode M1 of the first MCP.

Such a design enables each PE to have two potential amplification methods, as shown in Fig. 3.4. In the channel mode, they directly penetrate the channels; in the surface mode, they strike M1, generating secondary electrons that subsequently enter the channels, as detailed in <sup>[2]</sup>. Once inside the MCP channel, the electrons undergo multiple collisions with the channel wall, leading to amplification through a series of multiplicative processes, as described in<sup>[1]</sup>

The choice of these two routes constitutes a Bernoulli trial<sup>[1]</sup>. Regarding those low-energy secondary electrons in the surface mode, the MCP gain is significantly lower than that of the primary PEs in the channel mode, as reported in Ref.<sup>[10]</sup>.

### 3.1.4.3 Voltage-division Experiment

The dependence of the MCP gain for an electron versus its incident energy at the channel entrance is crucial to understanding the jumbo charges. We designed a voltage-division experiment to measure such a relationship. It is of critical importance for the origin of the jumbo charges to understand the dependence of the MCP gain for an electron on its incident energy at the channel entrance. To measure such a relationship, we devised a voltage-division experiment.

As shown in Fig 3.4, a positive high-voltage power supply (positive HV) was utilized to keep the potentials applied to the MCPs stable through the circuit<sup>[38]</sup>. In parallel, a negative high-voltage power supply (negative HV) was taken to vary the electric potential difference between the photocathode and M1, which can help get PEs at different incident energies. Our circuit design was adapted from the circuit implementation presented in<sup>[38]</sup>. In our modification, we eliminated the redundant resistors R1 and R2, while keeping the remaining resistors unaltered. In comparison with the experiment conducted by Yang et al.<sup>[25]</sup>, in which the potentials of all electrodes M1 - 4 are controllable, our design represents a simplified adaptation. This adaptation is specifically aimed at tuning the energies of the PEs using commercially available HV products.

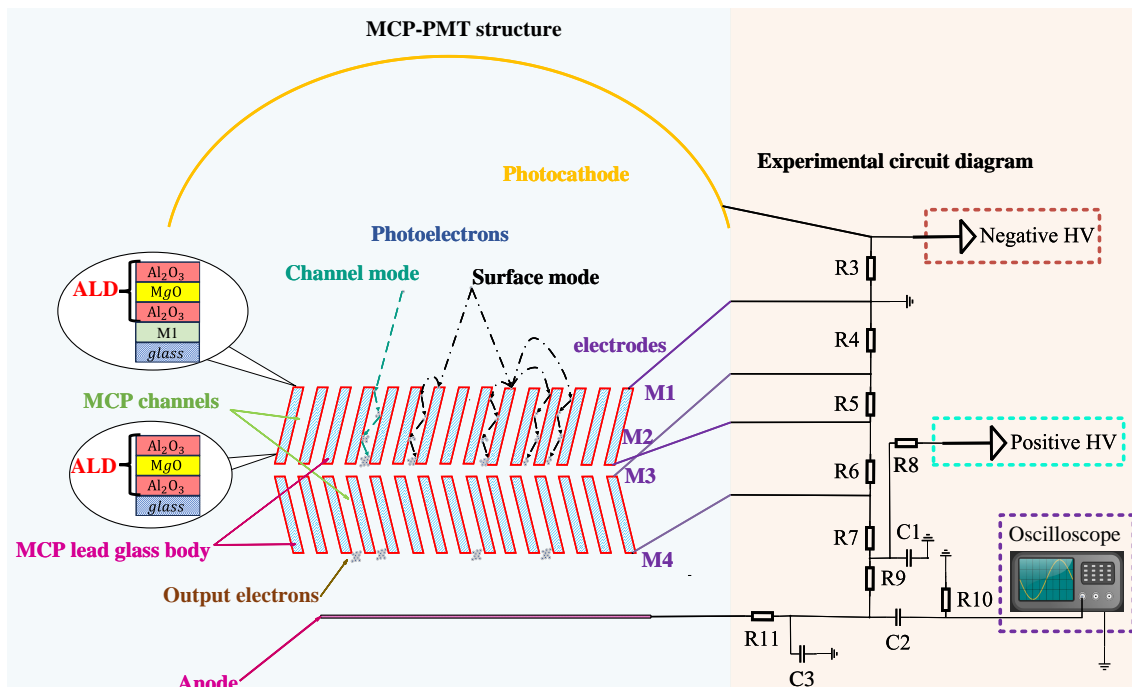


Figure 3.4 In the context of MCP operation, M1 and M3 serve as the input electrodes, while M2 and M4 function as the output electrodes. These four electrodes establish the potential differences essential for the device's operation.

A picosecond laser with a wavelength of 405 nm was used to illuminate the MCP-

PMT at 1 kHz rate. The laser also feed an electronic trigger signal to capture waveform data. We adjusted the intensity of the picosecond laser until the occupancy was below 0.1 to obtain the single PE.

A 10-bit oscilloscope (HDO9000 with HD1024 Technology)<sup>[39]</sup> was utilized to capture the 100 ns waveform. This oscilloscope worked at a sampling rate of 40 GS/s and a range of [-20, 60] mV.

We obtained the MCP gain at different incident energies of the electrons by fitting the Gaussian on the charge distribution. To control the experimental variables and contrast the effect of the surface mode, the same experiment were conducted on two MCP-PMTs with (Fig. 3.5(b)) and without (Fig. 3.5(a)) Al<sub>2</sub>O<sub>3</sub>-MgO deposited on M1. The positive voltage for the MCP-PMT with Al<sub>2</sub>O<sub>3</sub>-MgO on M1 was +1205 V after calculation and for that without Al<sub>2</sub>O<sub>3</sub>-MgO on M1 was +1240 V, respectively. The energies of the PEs when generated at the photocathod are  $\sim 1$  eV<sup>[12]</sup> and the error of the negative HV itself is within 2 V. The incident energies ( $E_0$ ) can be treated as the energies that the PEs get in the electric field, numerically equal to the voltage between the photocathode and M1, with a systematic error of  $\pm 2$  eV. The MCP gain was scanned every 10 eV when  $10 \leq E_0 < 100$  eV, every 20 eV when  $100 \leq E_0 < 200$  eV and every 50 eV when  $200 \leq E_0 \leq 650$  eV. The scan range is  $10 \leq E_0 \leq 600$  eV for the MCP-PMT with Al<sub>2</sub>O<sub>3</sub>-MgO deposited on M1 and  $10 \leq E_0 \leq 680$  eV for that without.

The charges of the captured waveforms were measured using *fast stochastic matching pursuit* (FSMP)<sup>[40-41]</sup>. This method can suppress the interference of electronic noise, enabling the acquisition of accurate charge spectra across a wide range of gain. Due to FSMP's capacity to PEs, the charge is zero when  $n_{PE} = 0$ , and the pedestal is clearly removed from the charge distribution. In Fig. 3.5, the peaks are associated with the channel mode. The jumbo charges coming from the surface mode are located to the right of the peaks, while the insufficient amplifications are to the left. For the MCP-PMT without Al<sub>2</sub>O<sub>3</sub>-MgO deposited on M1, since the contribution of secondaries from the surface mode is minimal, there are no large charges in the charge spectrum, as depicted in Fig. 3.5(a). To determine the MCP gain for electrons in channel mode, only the peak was fitted to eliminate the influence of the surface mode.

We acquired approximate values of  $\mu_p$  and  $\sigma_p$  for the charge distribution. These values were used to supply initial values and ranges for a detailed fitting process. The fitting ranges were decided based on the incident energies of the PEs. Specifically, when  $E_0 >$

100 eV, the range was set as  $[\mu_p - 1.3\sigma_p, \mu_p + 1.6\sigma_p]$ ; when  $30 < E_0 \leq 100$  eV, it was  $[\mu_p - 0.8\sigma_p, \mu_p + 1.6\sigma_p]$ ; and when  $E_0 \leq 30$  eV, the range became  $[\mu_p - 1.5\sigma_p, \mu_p + 1.8\sigma_p]$ . To measure the MCP gain for electrons at various energies, it suffices to extract the mean charge  $\mu(E_0)$  and the standard deviation  $\sigma(E_0)$  of the channel - mode peak.

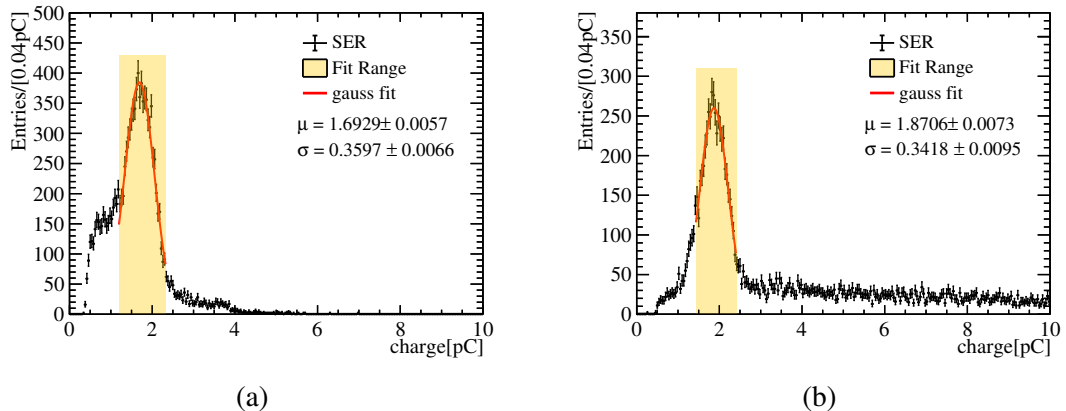


Figure 3.5 The fit of the charge spectrum of the MCP-PMT is presented both without (a) and with (b)  $\text{Al}_2\text{O}_3$ -MgO deposited on M1. It was noticed that (a) does not show jumbo charges. The yellow regions represent intervals that depend on the incident energy, and the red lines are the fitting outcomes of the Gaussian functions within these intervals.

After performing Gaussian fitting, we conduct linear interpolation and extrapolation to acquire the relationships of  $\mu(E_0)$  and  $\sigma(E_0)$  presented in Fig. 3.6. The disparity in the relationships of MCP-PMTs with and without  $\text{Al}_2\text{O}_3$ -MgO deposited on M1 stems from the impact of the charge contributed by the surface mode. When  $E_0 < 200$  eV,  $\mu(E_0)$  experiences a rapid increase. Once  $E_0 > 200$  eV,  $\mu(E_0)$  gradually reaches a stable state. The  $\sigma(E_0)$  generally increases in a manner similar to  $\mu(E_0)$ , yet it shows a decrease around 200 eV. Yang et al.<sup>[25]</sup> reported a similar tendency for  $\mu(E_0)$ . In our study, the optimal relative resolution  $\sigma/\mu$  occurs at approximately 600 eV, while the results of Yang et al. indicated 200 eV. Cao et al.<sup>[20]</sup> discovered that the SEY of  $\text{Al}_2\text{O}_3$ -MgO rises with the incident energy within the range of 100 - 600 eV. Even though the film structure and thickness we employed are different, taking into account the variation curves of the SEY of  $\text{Al}_2\text{O}_3$  and MgO with energy, we can still make a rough evaluation that the trend of  $\sigma/\mu$  obtained herein is reasonable.

#### 3.1.4.4 Charge-Spectra Decomposition

The Furman model presented in Sec. 3.1.4.1 forecasts the energies of the secondaries. In our voltage-division experiment detailed in Sec. 3.1.4.3, we measured the correlation between the MCP gain and the incident energies of electrons. We calculate the charge dis-

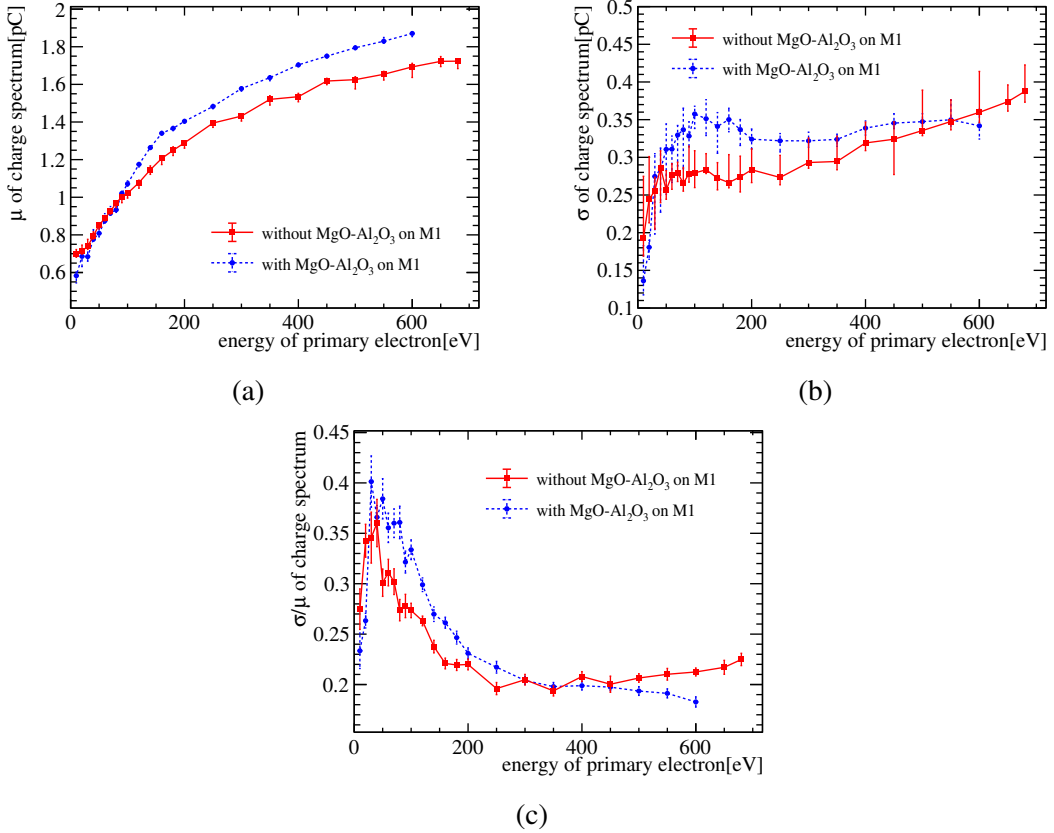


Figure 3.6 In (a), the mean value  $\mu$  rises as the incoming electron energy  $E_0$  goes up. Regarding (b), the standard deviation  $\sigma$  varies with energy. The MCP - PMT with Al<sub>2</sub>O<sub>3</sub>-MgO deposited on M1 (represented by the red line) exhibits a variation trend similar to that of the one without such deposition (represented by the blue line). In (c), the resolution  $\sigma/\mu$  increases in the range of 0 - 50 eV, decreases between 50-400 eV, and after 400 eV, for the MCP-PMT with Al<sub>2</sub>O<sub>3</sub>-MgO deposited on M1 (the blue line), there is a slight decline, while for the one without such deposition (the red line), there is a slight increase.

tribution using Monte Carlo following the flowchart shown in Fig. 3.7. In this research, we directed the laser at the apex of the photocathode hemisphere, and the PEs struck M1 with an incident angle of  $\theta_0 = 0^\circ$ . The intricate amplification process within the channels is characterized by the incident energy-dependent Gamma distributions  $\Gamma(\alpha(E), \beta(E))$  as described in Sec. 3.1.3. The values of  $\alpha(E)$  and  $\beta(E)$  are estimated based on the relationships of  $\mu(E)$  and  $\sigma(E)$  of an MCP-PMT without an Al<sub>2</sub>O<sub>3</sub>-MgO coating on the input electrode. This approach removes the influence of the surface mode. Considering the light intensity, we sample  $n_{\text{PE}}$  from the Poisson distribution multiple times. Then, we sum up  $n_{\text{PE}}$  SER charges for the output to obtain a spectrum. When sampling an SER charge, for a Bernoulli trial, we assign the probabilities of the channel and surface modes as  $p$  and  $1-p$  respectively. The SER charge spectrum  $f_{\text{MCP-PMT}}(Q)$  is given by the following equation:

$$f_{\text{MCP-PMT}}(Q) = p f_{\text{ch}}(Q) + (1-p) f_{\text{surf}}(Q) \quad (3.8)$$

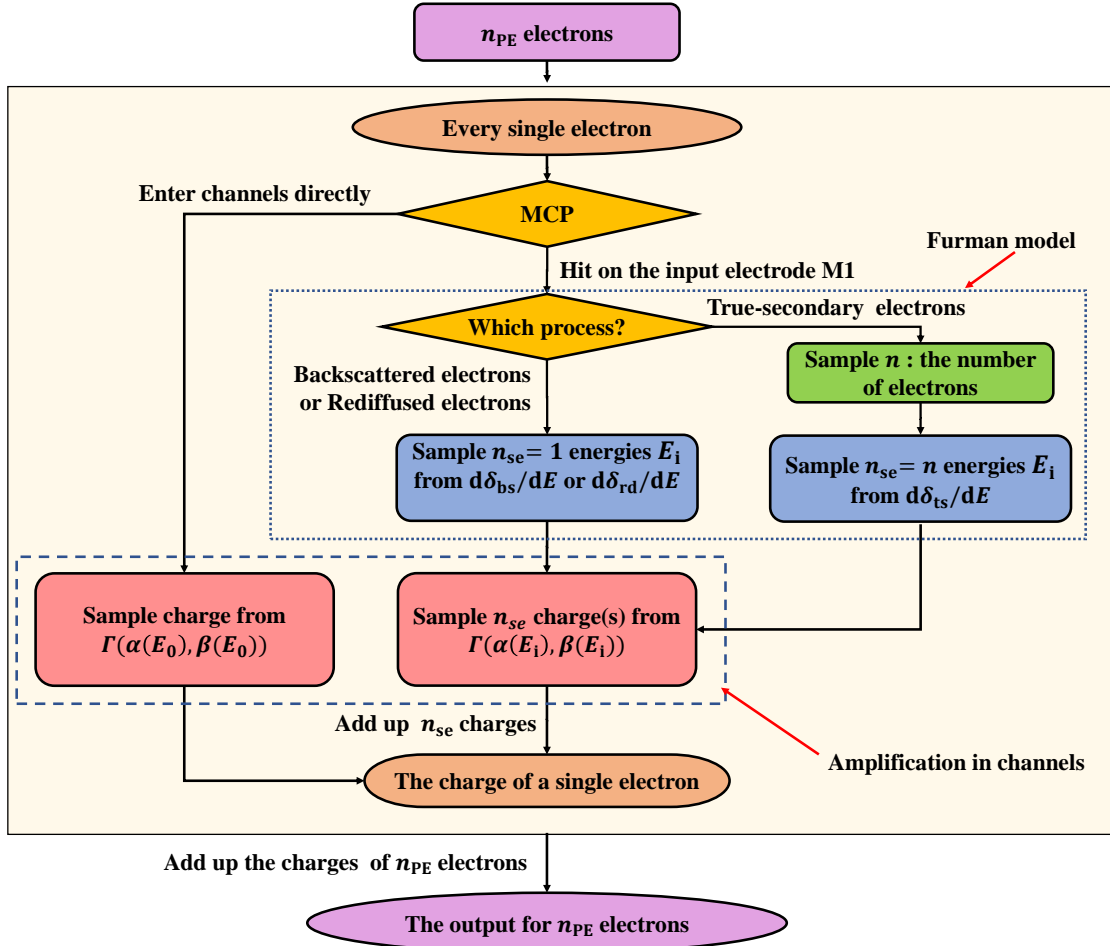


Figure 3.7 The flowchart of Monte Carlo for calculating the charge spectrum is presented. The output charge is composed of  $n_{PE}$  SER charges. In the channel mode, the PEs directly enter the channels, whereas in the surface mode, the PEs strike the input electrode. The energies of the  $n_{se}$  secondaries in the surface mode are sampled according to the Furman model. The amplification in the channels is modeled using the incident energy-dependent Gamma distribution.

Here,  $f_{ch}(Q)$  and  $f_{surf}(Q)$  represent the charge distributions of the channel and surface modes.  $f_{ch}(Q)$  is set to  $f_{\Gamma}(Q; \alpha(E_0), \beta(E_0))$ , where the incident energy is 650 eV. The factors  $\alpha(E_0), \beta(E_0)$  are derived from  $\mu(E_0)$  and  $\sigma(E_0)$  without the Al<sub>2</sub>O<sub>3</sub>-MgO coating as shown in Fig. 3.6. According to the Furman model,  $f_{surf}(Q)$  is divided into three components corresponding to Eqs. (3.4)–(3.6). Specifically,  $f_{bs}(Q)$  is for the back-scattered electrons,  $f_{rd}(Q)$  is for the redifused electrons, and  $f_{ts}(Q)$  is for the true-secondary electrons.

$$\begin{aligned}
 f_{surf}(Q) &= p_{bs}f_{bs}(Q) + p_{rd}f_{rd}(Q) + (1 - p_{bs} - p_{rd})f_{ts}(Q) \\
 &= \delta_{bs}f_{bs}(Q) + \delta_{rd}f_{rd}(Q) + (1 - \delta_{bs} - \delta_{rd})f_{ts}(Q)
 \end{aligned} \tag{3.9}$$

In this context,  $p_{bs}$  and  $p_{rd}$  represent the mixture ratios. These ratios are decided by the composition and thickness of the surface emissive material, which can differ among the

PMTs. According to Furman and Pivi in reference<sup>[5]</sup>, it is assumed that in the back-scattered mode and rediffused mode, only one electron is emitted. As a result,  $\delta_{\text{bs}} = p_{\text{bs}}$  and  $\delta_{\text{rd}} = p_{\text{rd}}$ . During the calculation process, we set  $\delta_{\text{rd}} = 0.09$  and  $\delta_{\text{bs}} = 0.01$ . The energy of the back-scattered electron is approximately the same as that of the PEs in the channel mode. Consequently, the MCP gain for the back-scattered electron is also similar to that in the channel mode. In contrast, the energy of the rediffused electron is in the range of 100 eV to 600 eV, which is relatively lower. Due to the relatively slow increase of the gain in this energy range as shown in Fig. 3.6(a), the charge after MCP multiplication for the rediffused electron is slightly smaller. Both the back-scattered and rediffused electrons contribute a single electron each. In the charge spectra, they are virtually indistinguishable from the channel mode. This degeneracy phenomenon is concisely presented in Eq. (3.10).

$$\begin{aligned} f_{\text{MCP-PMT}}(Q) &= pf_{\text{ch}}(Q) + (1-p)f_{\text{surf}}(Q) \\ &= pf_{\text{ch}}(Q) + (1-p)[\delta_{\text{bs}}f_{\text{bs}}(Q) + \delta_{\text{rd}}f_{\text{rd}}(Q) + (1-\delta_{\text{bs}}-\delta_{\text{rd}})f_{\text{ts}}(Q)] \\ &= [p + (1-p)(\delta_{\text{bs}} + \delta_{\text{rd}})]f_{\text{ch}}(Q) + (1-p)(1-\delta_{\text{bs}}-\delta_{\text{rd}})f_{\text{ts}}(Q) \end{aligned} \quad (3.10)$$

In this situation, the spectra  $f_{\text{ch}}(Q)$ ,  $f_{\text{rd}}(Q)$ , and  $f_{\text{bs}}(Q)$  are combined into  $f_{\text{ch}}(Q)$ . However, Eq. (3.10) is not complete. We need to take into account the scenario where the secondaries strike the MCP surface once more. The round trip does not introduce additional energy. A back-scattered or rediffused secondary is amplified in a manner that is essentially the same as a primary PE. On the other hand, a true-secondary electron has an energy that is too low to undergo multiplication again. Consequently,  $p_0$ , which is the net contribution to  $f_{\text{ch}}(Q)$ , forms a geometric series.

$$p_0 = p \sum_{i=0}^{\infty} [(1-p)(\delta_{\text{bs}} + \delta_{\text{rd}})]^i = \frac{p}{1 - (1-p)(\delta_{\text{bs}} + \delta_{\text{rd}})} \quad (3.11)$$

and  $f_{\text{ts}}(Q)$  gets  $\frac{(1-p)(1-\delta_{\text{bs}}-\delta_{\text{rd}})}{1-(1-p)(\delta_{\text{bs}}+\delta_{\text{rd}})}$  or  $1 - p_0$ . Eq. (3.10) is remarkably reduced to

$$f_{\text{MCP-PMT}}(Q) = p_0 f_{\text{ch}}(Q) + (1 - p_0) f_{\text{ts}}(Q). \quad (3.12)$$

For the true-secondary electrons, the count  $n$  follows a Poissonian. The sum of the sampled  $n$  charges serves as the output  $Q_{\text{ts}}$ ,

$$\begin{aligned} Q_{\text{ts}} &= \sum_{i=1}^n Q_i \\ n &\sim (\delta'_{\text{ts}}) \end{aligned} \quad (3.13)$$

$$Q_i \sim \Gamma[\alpha(E_i), \beta(E_i)]$$

where  $E_i$  is sampled from Eq. (3.6). The values of  $\alpha(E_i)$  and  $\beta(E_i)$  are derived from  $\mu(E_i)$  and  $\sigma(E_i)$  as presented in Fig. 3.6. For the sake of comprehensiveness,  $\delta_{ts} = (1 - \delta_{bs} - \delta_{rd})\delta'_{ts}$  represents the ratio of the electric current of the true-secondary electrons to that of the primary electrons. The charge spectra corresponding to different values of  $n$  are depicted in Fig. 3.8(a). Owing to the relatively lower energies of the secondary electrons, their charges are smaller. Differentiating each charge formed at the anode is a difficult task because multiple secondary electrons enter the MCP channels at the same time. A larger value of  $n$  leads to a greater charge.

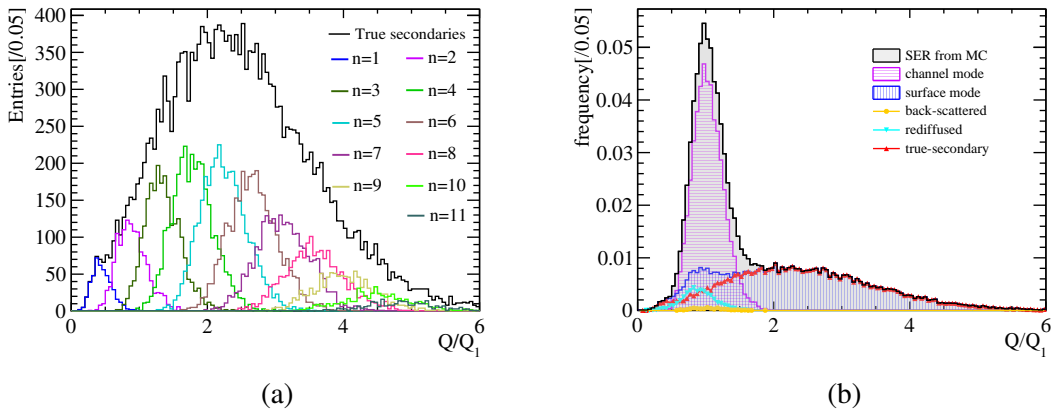


Figure 3.8 (a): In the MC calculation, when  $\delta'_{ts} = 5.5$  and  $p_0 = 0.55$ , this shows the charge distribution of the true-secondary electrons mode. The black histogram represents the sum of all distributions. (b): The charge distribution formed in the channel mode is centered around the peak. Meanwhile, the tail part is mainly produced by the true-secondary electrons in the surface mode.

Fig. 3.8(b) presents a typical decomposition of the SER charge spectra. The jumbo charges, which are also referred to as the “long tail,” result from the true secondaries generated by the surface mode.

### 3.1.5 Parameter Extraction from Data

From Eq. (3.12) and (3.13), it can be clearly seen that  $\delta'_{ts}$  and  $p_0$  have a substantial influence on the SER charge distribution, as shown in Fig. 3.9. To determine these two parameters, we utilize the MCP - PMT test data provided by Zhang et al.<sup>[14]</sup>.

We conduct a chi-square test for each pair of the predicted and measured charge distributions. The same binning approach is used to divide these two histograms into  $r$  bins. Let the number of entries in the  $i$ -th bin be  $n_i$  and  $m_i$ , where  $N = \sum_{i=1}^r n_i$  and  $M = \sum_{i=1}^r m_i$ . As stated in reference<sup>[42]</sup>, the chi-square test serves to show the similarity between the

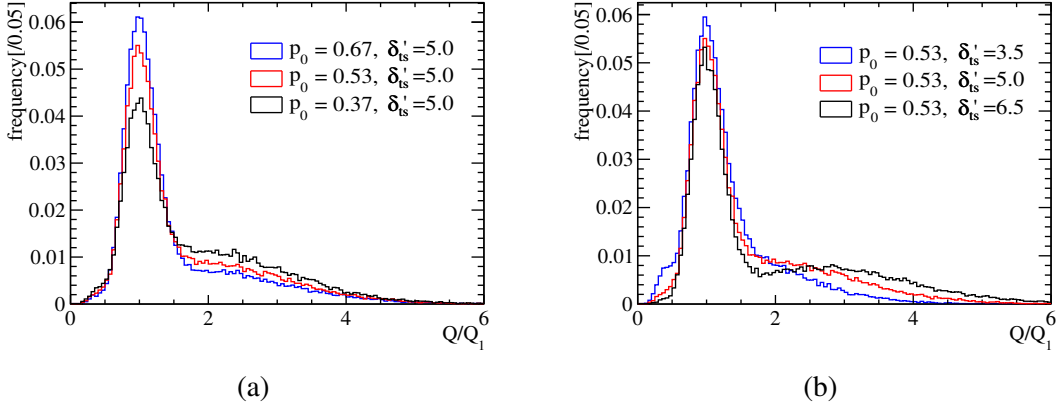


Figure 3.9 The shape of the SER charge spectrum obtained from MC is affected by  $\delta'_{ts}$  and  $p_0$ . When  $\delta'_{ts}$  rises, the tail region extends more. When  $p_0$  increases, the height of the principal peak region goes up, and the tail becomes narrower.

two histograms.

$$\begin{aligned} \chi^2_{r-1} &= \sum_{i=1}^r \frac{(n_i - N\hat{k}_i)^2}{N\hat{k}_i} + \sum_{i=1}^r \frac{(m_i - M\hat{k}_i)^2}{M\hat{k}_i} \\ &= \frac{1}{MN} \sum_{i=1}^r \frac{(Mn_i - Nm_i)^2}{n_i + m_i} \end{aligned} \quad (3.14)$$

where  $\hat{k}_i = \frac{n_i+m_i}{N+M}$ .

The  $\chi^2_{r-1}$  values are scanned across the  $(p_0, \delta'_{ts})$  grid. An example is presented in Fig. 3.10(a). We adopt a linear model<sup>[43]</sup> to smooth the approximately parabolic relationship between the  $\chi^2_{r-1}$  and  $(p_0, \delta'_{ts})$ . Subsequently, we extract the  $(\hat{p}_0, \hat{\delta}'_{ts})$  values that minimize  $\chi^2_{r-1}$ , along with intervals at 68.3 % confidence levels<sup>[44]</sup>.

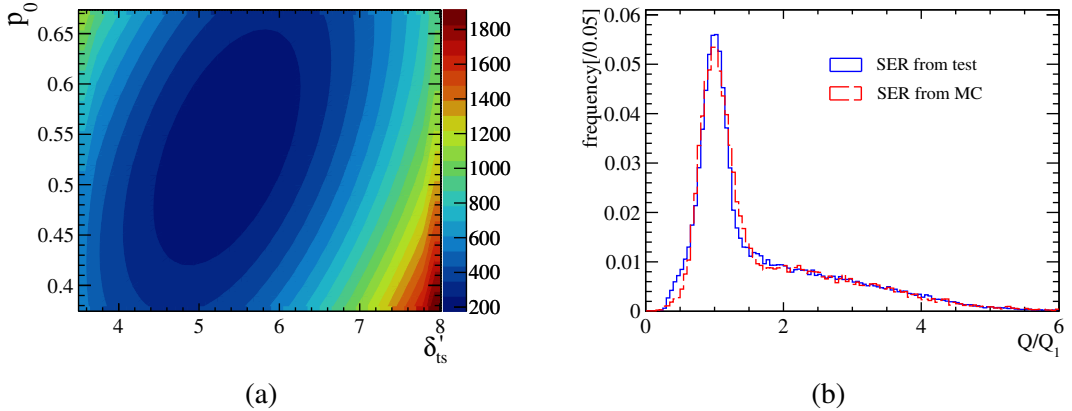


Figure 3.10 The plot in (a) is a contour plot of the chi-square test. Here,  $p_0$  and  $\delta'_{ts}$  are used as parameters, and the chi-square values represent the height. The plot in (b) shows an example of the Monte Carlo (MC) histogram (depicted by the red line) and the histogram obtained from the test (represented by the blue line).

The scatter plot of  $\hat{\delta}'_{ts}$  versus  $\hat{p}_0$  for 9 MCP-PMTs shown in Fig. 3.11 does not suggest a

strong correlation. This is because they are decided by independent manufacturing steps. On an average basis, the value of  $\delta'_{ts}$  is 5.979 and that of  $p_0$  is 0.5341. The PEs of the channel, back-scattered, and rediffused surface modes make up 53.41 %, forming the peak. For each of the remaining cases, when hitting the surface, it induces 5.979 true-secondary electrons on average.

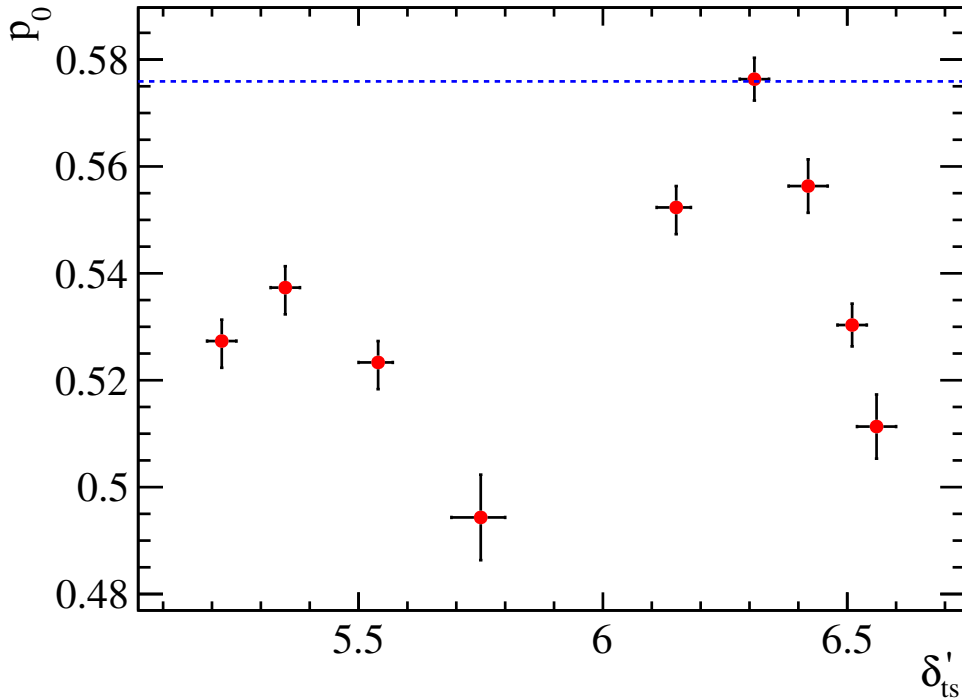


Figure 3.11 When performing convolution with 9 MCP-PMTs, the distribution of  $\delta'_{ts}$  and  $p_0$  takes place at the point of minimum chi-square. The blue dashed line represents the expected  $\hat{p}_0$  that is estimated from<sup>[45]</sup>.

To make a comparison between our measurement and previous studies, we transform  $\delta'_{ts}$  into the SEY  $\delta$ .

$$\delta = \delta_{bs} + \delta_{rd} + (1 - \delta_{bs} - \delta_{rd})\delta'_{ts} \quad (3.15)$$

and the fraction  $p_0$  to  $p$  is determined by Eq. (3.11). Cao et al.<sup>[20]</sup> measured the secondary electron yield (SEY) of the Al<sub>2</sub>O<sub>3</sub>-MgO double - layered film to be in the range of 4 - 5. Chen et al.<sup>[2]</sup> noted that there exists an electrostatic lens effect at the entrances of the microchannel plate (MCP) channels. This effect results in the ratio of the PEs entering the MCP channels being smaller than the open - area ratio. When the incident angle of the PEs is  $\theta_0 = 0^\circ$ , when the open - area ratio of the MCP is 74.9 %, the proportion of PEs directly entering the MCP channels is approximately 60 %. Chen et al.<sup>[45]</sup> showed that when the open - area ratio is 65 %, this proportion is around 55 %. In our study, the

MCPs have pore diameters of 12 m, the spacing between pores is 14 m, and the open-area ratio is 66.6 %. For  $\delta_{\text{rd}} + \delta_{\text{bs}} = 0.1$ , the expected value of  $\hat{p}_0$  is calculated as

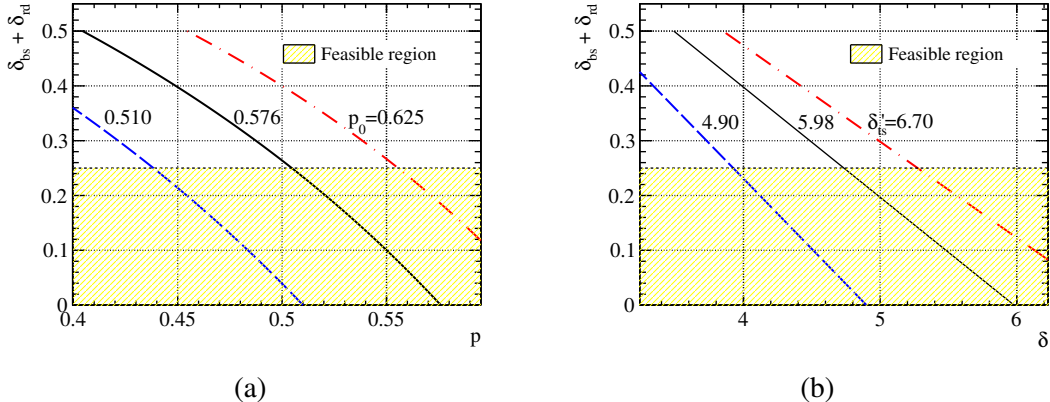
$$\hat{p}_0 = \frac{55\%}{1-(1-55\%) \delta_{\text{rd}} + \delta_{\text{bs}}} \approx 57.6\%.$$


Figure 3.12 Relations of  $\delta_{\text{bs}} + \delta_{\text{rd}}$  vs. the SEY  $\delta$  and the fraction of channel mode  $p$ . The feasible region shows the consistency of our measurement to the literature.

In Fig. 3.12, when considering the typical values of  $\delta = 5$  and  $p = 0.55$ , our measurement aligns with the assumption that  $\delta_{\text{bs}} + \delta_{\text{rd}} < 0.25$ . Beck<sup>[46]</sup> indicated that the minor contribution of back-scattered and rediffused electrons in SEE holds particularly true for insulators featuring a high SEY.

### 3.1.6 Gamma-Tweedie model for MCP-PMT

In our computations, the distribution of the MCP charge response to the true-secondary electrons, denoted as  $\Gamma(\alpha_i, \beta_i)$ , is dictated by their energies  $E_i$ . These energies  $E_i$  meet the condition  $\sum_i^n E_i < E_0$ . The incident energy  $E_0$  of the PEs is 650 eV, which is over ten times the energies of the true secondaries. Since  $n$  adheres to a Poisson distribution with an expected value ranging from 5 to 6.5, the probability that  $n$  is greater than 10 is extremely low and can be disregarded. Consequently, the influence of  $n$  on  $E_i$  can be neglected, and the energy  $E_i$  has an independent and identical distribution, as illustrated in Fig. 3.13(a). Correspondingly, the charge response of the MCP to a single true-secondary electron can be treated in the same manner, as presented in Fig. 3.13(b). Moreover, a single Gamma distribution  $\Gamma(\alpha', \beta')$  is sufficiently adaptable to depict the continuous mixture of  $\int dE_i \frac{1}{\delta_{\text{ts}}} \frac{d\delta_{\text{ts}}}{dE_i} \Gamma[\alpha(E_i), \beta(E_i)]$ .

When we employ such a single  $\Gamma(\alpha', \beta')$  in Equation (3.13), the resulting Poisson-Gamma compound represents a particular instance of the Tweedie distribution  $\text{Tw}_{\xi}(\alpha, \beta)$

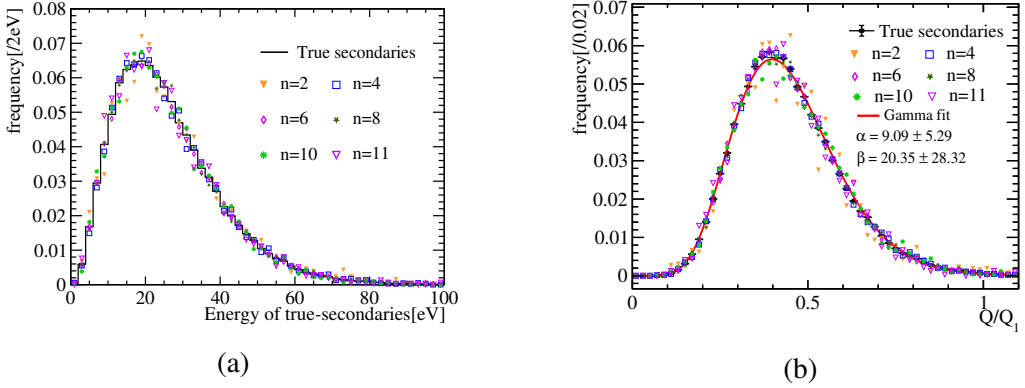


Figure 3.13 The energy distribution and the charge distribution of MCP to a single true-secondary electron vary with different values of  $n$ . (a): Even when  $n$  takes different values, all the energies of the true secondaries follow the same distribution pattern. (b): The charge response of MCP to a single true-secondary electron remains the same. Moreover, the fitting with the Gamma distribution  $\Gamma(\alpha', \beta')$  attains an adequate level of goodness.

with  $1 < \xi < 2$  as stated in<sup>[47]</sup>.

$$\left. \begin{array}{l} Q_{ts} = \sum_{i=1}^n Q_i \\ n \sim (\delta'_{ts}) \\ Q_i \sim \Gamma(\alpha', \beta') \end{array} \right\} \Rightarrow Q_{ts} \sim \text{Tw}_\xi(\alpha', \beta') \quad (3.16)$$

A phenomenological joint fit of the  $f_{ch}$  Gamma and  $f_{ts}$  Tweedie mixture, using Eq. (3.12) and (3.16), is adequate for calibrating the SER charge spectrum and measuring  $p_0$  and  $\delta'_{ts}$ . The relations  $\mu(E_i)/\sigma(E_i)$  from the voltage division experiment (Sec. 3.1.4.3) and the Furman model help us understand the jumbo charges and justify the phenomenological Gamma - Tweedie mixture. However, they are less useful in practical PMT calibrations. The number of parameters, two for  $f_{ch}$  Gamma and three for  $f_{ts}$  Tweedie, can cause difficulties in achieving convergence. This issue can be addressed by applying physical constraints. Usually,  $\frac{\alpha'}{\beta'} \approx 0.45Q_1$  and  $\sqrt{\frac{\alpha'}{\beta'^2}} \approx 0.15Q_1$ . When the incident energy  $E_0$  is much larger than  $E_i$ , it is practical to set bounds for them in the ranges of  $[0.3, 0.7]Q_1$  and  $[0.05, 0.3]Q_1$ . We have also examined the chi-square results in the Gamma-Tweedie fitting, and the obtained  $\chi^2/\text{ndf} < 10$  indicates a good fit. Under these circumstances, we are able to formulate the mathematical model for the SER of the MCP-PMT:

$$f_{\text{MCP-PMT}}(Q) = p_0 \Gamma(Q; \alpha, \beta) + (1 - p_0) \text{Tw}_\xi(Q; \alpha', \beta') \quad (3.17)$$

### 3.1.7 The gain distribution of PMTs

We used the charge spectrum of dark noise for gain calibration. As shown in the Fig. 3.14, we only utilized the information within the first 100 ns of each event to en-

sure obtaining a clean dark noise signal. For the Dynode-PMTs in JUNO, we deploy the Gamma distribution ( $\Gamma(Q; \alpha, \beta)$ ) for the gain calculation and Gamma-Tweedie distribution ( $p_0\Gamma(Q; \alpha, \beta) + (1 - p_0)\text{Tw}_\xi(Q; \alpha', \beta')$ ) for MCP-PMTs. As shown in Fig. 3.15, for Dynode-PMT, the Gamma distribution can already depict the properties of the main peak extremely clearly. For MCP-PMT, the Gamma-Tweedie distribution can not only clearly describe the long-tail structure, but also demonstrates excellent performance during the fitting process. In addition to defining the gain of the main peak ( $G_p$ ), we also need to define the average gain ( $G_m$ ) that describes the mean of the entire SER for MCP-PMTs. Therefore, in our work, we have defined the gain of each of the two distributions respectively.

- For Dynode-PMTs,  $G_m = G_p = \frac{\alpha}{\beta}$
- For MCP-PMTs,  $G_p = \frac{\alpha}{\beta}$  and  $G_m = p_0 \frac{\alpha}{\beta} + \lambda \frac{\alpha'}{\beta'}$

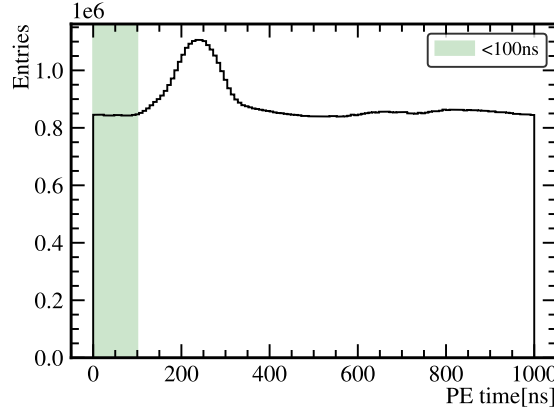


Figure 3.14 The range of PE time for gain and calibration. Only the PEs in the first 100 ns are used.

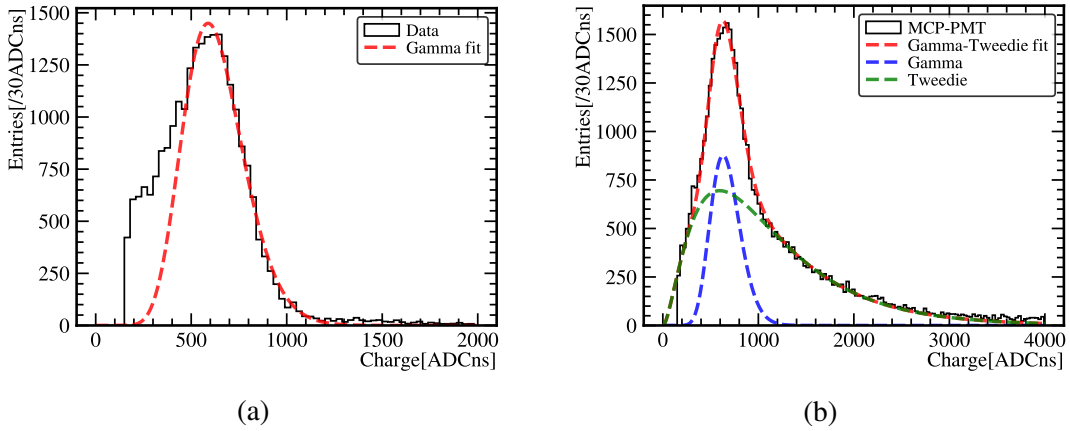


Figure 3.15 The gain fit of PMTs. (a) shows the Gamma distribution fit of Dynode-PMTs, and (b) shows the Gamma-Tweedie fit of MCP-PMTs.

As illustrated in Fig. 3.16, for the two types of PMTs, the fitted  $G_p$  values are already aligned quite well. However, regarding  $G_m$ , the value of MCP-PMT is significantly higher than that of Dynode-PMT. Also, the average gain of MCP-PMTs is much larger than the peak gain. This indicates that in the long-tail structure,  $\lambda \frac{\alpha'}{\beta'}$  is greater than  $\frac{\alpha}{\beta}$ , which is consistent with our experimental conclusion.

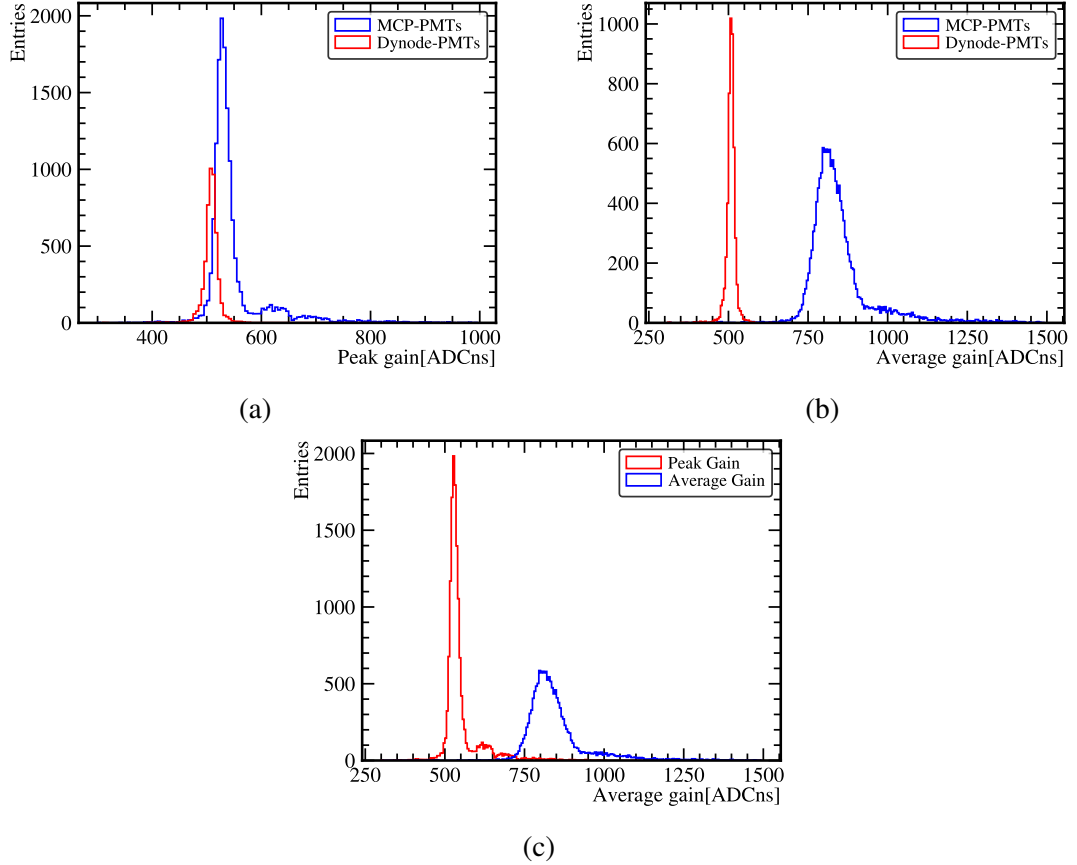


Figure 3.16 The gain distribution of PMTs. (a) shows the peak gain distribution, (b) indicated the average gain distribution, and (c) illustrates the peak gain and average gain of MCP-PMTs.

### 3.2 The dark count rate

Since we imposed restrictions on the selection of dark noise when performing gain calibration, on this basis, the dark noise count rate (DCR) of the PMT can be calibrated. The formula used to calculate the DCR is Eq. (3.18).  $n_{PE,100}$  is the number of PEs in first 100 ns and  $n_w$  is the number of events.

$$DCR = \frac{n_{PE,100}}{n_w * 100} \quad (3.18)$$

Taking Run 3279 on February 2nd as an example, the distribution of the DCR obtained from the calibration is shown in the Fig. 3.17. It can be seen that the mean dark noise rate

of the MCP-PMT is about 33 kHz, which is about 5 kHz higher than that of the Dynode-PMT. At the same time, from the perspective of the position distribution, the distribution of the DCR is relatively uniform and there is no obvious asymmetry. For each analyzed

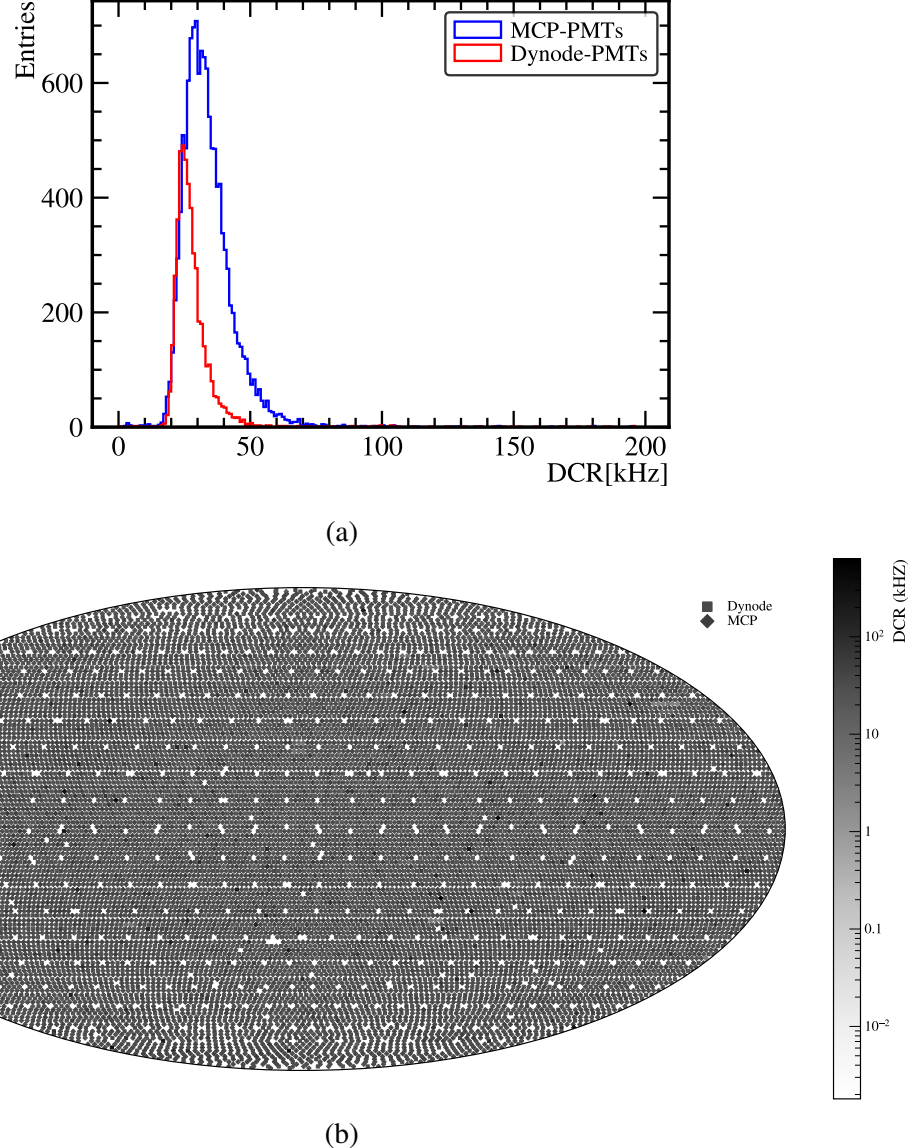


Figure 3.17 The DCR distribution of PMTs. In (a), the blue line shows the DCR of MCP-PMTs and the red one shows that of Dynode-PMTs. (b) shows the position distribution of DCR.

run, the DCR was calibrated independently. Consequently, the variation law of DCR with the data acquisition time can be straightforwardly investigated, as shown in Fig. 3.18. It has been observed that as the detector is in operation, the DCR initially increased, then gradually decreased, and ultimately stabilized. Throughout this transformation process, the DCR of the MCP-PMT consistently remained approximately 5 kHz higher than that of the Dynode-PMT. Simultaneously, the DCRs of both PMTs consistently exceeded 20 kHz.

This situation exerted a certain influence on and presents challenges to the Cherenkov reconstruction of the water phase. Thus, it was essential to develop a mathematical model of the dark noise and apply it to the reconstruction.

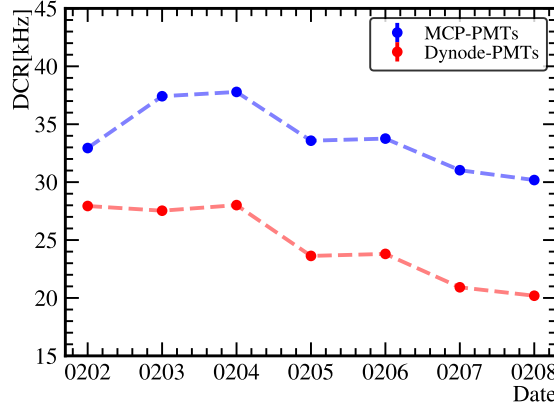


Figure 3.18 The curve of DCR changing with time.

### 3.3 The timing calibration

In the water phase, the time characteristics are calibrated by laser. What has a relatively large impact on the subsequent reconstruction are the time starting point of each PMT, that is, the time-offset, and the transit time spread (TTS) of the PMT. In this work, we use the standard deviation to represent TTS instead of using the full width at half maximum. The distribution of time-offset is as shown in Fig. 3.19(a) and that of TTS is as illustrated in Fig. 3.19(b). The timing jitter (TTS) of the MCP-PMT is around 10 ns, which is significantly higher than that of the Dynode-PMT (around 2.5 ns). Therefore, in the reconstruction, the impact of TTS cannot be ignored, and modeling and application are required.

### 3.4 The Photon Detection Efficiency

The Photon Detection Efficiency (PDE,  $\epsilon$ ) is an important parameter for measuring the photon detection ability of a PMT. Numerically, it is equal to the product of QE and CE. In this work, we directly use the results obtained from the batch tests at Pan-Asia<sup>[22]</sup>, as shown in Fig. 3.20.

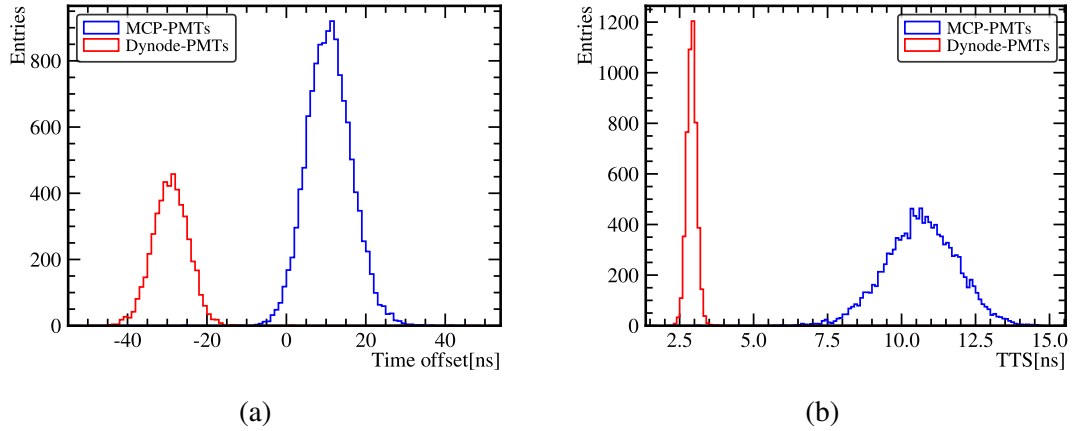


Figure 3.19 The timing characteristics in water phase. (a) shows the distribution of time-offset and (b) illustrates the distribution of TTS.

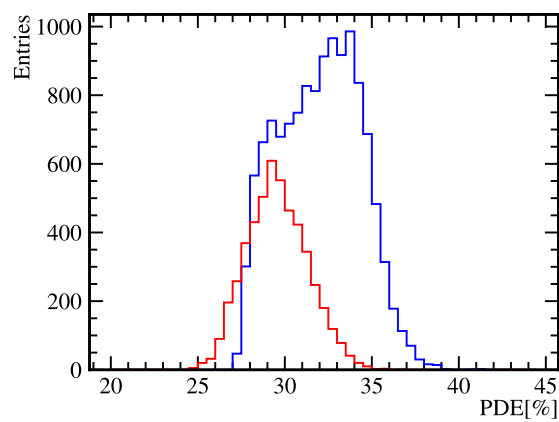


Figure 3.20 The distribution of PDE.

## CHAPTER 4 THE RECONSTRUCTION FOR THE WATER-PHASE

After carefully calibrating the PMTs, we can obtain the number of photons hitting the PMT and their arrival times for each event. Based on these information, we will use statistical methods to infer information such as the position, energy, and direction of the physical events that produced these photons. In the field of Cherenkov reconstruction, the Super-Kamiokande (SK) experiment is the most worthy of reference. SK stands as the world’s largest pure water Cherenkov detector, housing 50 kilotons of ultrapure water<sup>[48]</sup>. Building upon the liquid scintillator-Cherenkov combined track reconstruction technique developed for the MiniBooNE experiment<sup>[49]</sup>, SK collaboration has advanced a likelihood-based reconstruction method, utilizing PMT charge and time information<sup>[50]</sup>, named as fiTQun. For JUNO water-phase, we have implemented targeted improvements to the fiTQun and extended its application to low-energy event reconstruction at the MeV scale.

### 4.1 The Likelihood function

FiTQun simultaneously determines particle types, vertex positions, momentums, event times. In JUNO water-phase, we just need to determine the vertex position, momentums and event times. The likelihood function of fiTQun is defined as:

$$\begin{aligned} \log \mathcal{L}(\mathbf{x}; q, t) = & \sum_{j \in \{q=0\}} \log P_j(q = 0 \mid \mu_j) \\ & + \sum_{i \in \{q>0\}} \log(f_q(q_i \mid \mu_i)) \\ & + \sum_{i \in \{q>0\}} \log(f_t(t_i \mid \mathbf{x})) \end{aligned} \quad (4.1)$$

- $\mathbf{x} = (t_0, x, y, z, p_x, p_y, p_z)$ : Event vertex containing time  $t_0$ , position  $(x, y, z)$ , and momentum  $(p_x, p_y, p_z)$ .
- $\mu_i(\mathbf{x})$ : Expected PEs at the  $i$ -th PMT, computed from the vertex  $\mathbf{x}$ .
- $q_i$ : Charge observed at the  $i$ -th PMT,  $\{q\}$  is the sequence of  $q_i$ , when  $q_i = 0$ , the PMT is unhit.
- $t_i$ : Hit time of the  $i$ -th PMT,  $\{t\}$  is the sequence of  $t_i$ .

The first term is the unhit likelihood, which is the probability of no hit in the PMT.

The second term is the hit likelihood, which is the probability of detecting hits in the PMT. The third term is the time likelihood, which is the probability of detecting a hit at a certain time.

Since in the operation of the detector, only TQ information (time and charge) is recorded for low-energy events, waveform information is unavailable. At the same time only the first hit time can be obtained. Therefore, it is necessary to reformulate the likelihood to adopt a first-hit-time-based reconstruction approach. Xuewei Liu et.al developed a first-principles-based reconstruction method using time-charge information or time-PE information in liquid scintillator detectors<sup>[51]</sup>. We adapt their methodology to reformulate the likelihood function for JUNO water-phase. In low-energy events, where each PMT typically detects only few photon, the number of hits can be directly approximated as NPE ( $N_{PE}$ ). We can reformulate the likelihood function as Eq. (4.2):

$$\begin{aligned} \log \mathcal{L}(\mathbf{x}; q, t) = & \sum_{j \in \{q=0\}} \log P_j(q = 0 \mid \mu_j) + \\ & \sum_{i \in \{q>0\}} \log(f_q(0 \mid \mu_{i,\underline{t}}^{t_i}) f_t(t_i) f_q(N_{PE,i} - 1 \mid \bar{\mu}_{i,t_i}^{\bar{t}})) \end{aligned} \quad (4.2)$$

In this case, we define the data taking as  $[\underline{t}, \bar{t}]$ , and the first hit time of the  $i$ -th PMT as  $t_i$ ,  $\mu_{i,\underline{t}}^{t_i}$  is the expected PEs in  $[\underline{T}, T_i]$ , same as  $\bar{\mu}_{i,t_i}^{\bar{t}}$ .

## 4.2 Response of the water-phase detector

To compute the likelihood, we need to predict how many photons each PMT will detect when given a vertex. The more accurate the predictions are, the better the reconstruction performances. Therefore, we need a comprehensive understanding of the detector response and develop accurate models for it. It naturally comes to mind that when a charged particle enters water, emits Cherenkov photons, and triggers the PMT, this process can be divided into two parts. One pertains to how Cherenkov light is emitted, while the other concerns how the Cherenkov photons propagate and are detected.

### 4.2.1 The Cherenkov emission profile

When a charged particle travels through a medium at a speed exceeding that of light, it emits Cherenkov photons within a specific solid angle range. The phenomenon arises from local polarization occurring along the charged particle's trajectory: when polarized molecules return to their ground state, they emit electromagnetic radiation. When the

refractive index of the medium is  $n$ , and the speed of light in vacuum is  $c_0$ , the condition of particle speed  $v_p$  for Cherenkov emmision is  $\beta = v_p/c_0 > 1/n$ . When in pure water, whose refractive index is  $n_w = 1.333$ , and the paitical is electron ( $m_0 = 0.511 \text{ MeV}$ ), the energy threthold is  $E_{th} = m_0 \times (\sqrt{1 - 1/n_w^2} - 1) = 0.262 \text{ MeV}$ . That means, only when the energy of electron is larger than 0.262 MeV, the Cherenkov photons will emit.

The direction of Cherenkov photons can be discribed as:  $\cos \theta = \frac{1}{\beta n_w}$  as Fig 4.1 shown.

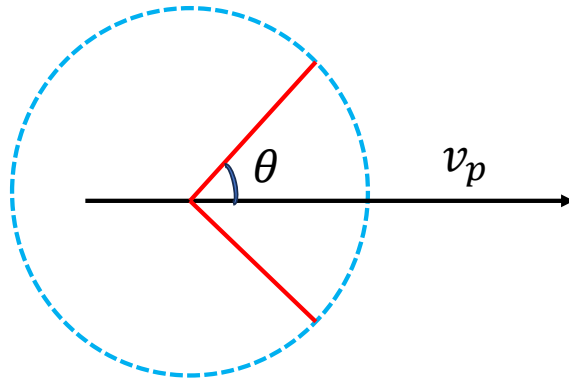


Figure 4.1 The direction of Cherenkov photons.  $\theta$  is the angle between the photon emission direction and the direction of particle motion.

When in water,  $\cos \theta \approx 0.75$ . We can use simulation to get the emmision profile of Cherenkov photons. Also, we consider the light yield of Cherenkov by simulating electron with momentum from 2 MeV to 30 MeV. Our simulation is based on JUNO software (JUNOsw)<sup>[52]</sup>, and the version is J24.2.1. We simulated electrons with momenta ranging from 2 to 50 MeV, uniformly distributed within the detector, while their emission directions were randomly oriented.

We extended Dou Wei's angular coordinate definition method for liquid scintillator detectors<sup>[53]</sup> to Cherenkov radiation detection by incorporating momentum direction degrees of freedom, resulting in the coordinate system illustrated in the figure.

In this simulation, we recorded the angles between the emission directions of all Cherenkov photons and the incident direction of the electron, and we do not care the photons are detected or not. Simultaneously, a crucial parameter is the distance between the photon generation point and the origin position of the charged particle.

- From Fig 4.3, most photons are emitted along the Cherenkov angle ( $\cos \theta = 0.75$ ), while a minority exhibit significant angular deviations from the electron's direction. When calculating the emission angle distribution, it must be analyzed separately

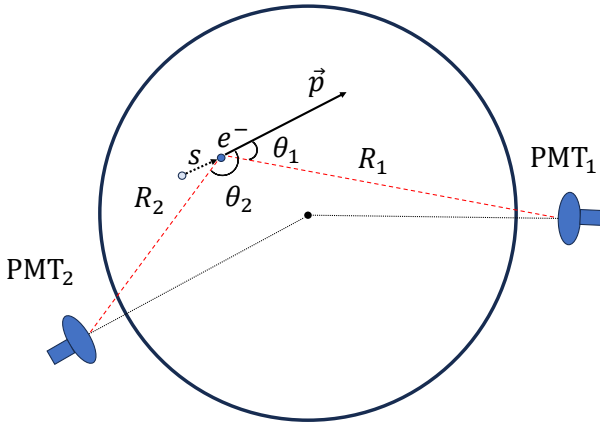


Figure 4.2 Coordinate system definition:  $\theta$  is the angle of the emission direction of Cherenkov photon and the incident direction of the electron,  $s$  is the distance from the position where the particle emits light to its initial position.  $R$  is the distance of PMT to the position of electron.

for different particle energies rather than applying a single angular distribution to electrons of all energies.

- From Fig 4.4, as the particle moves, Cherenkov photons emitted along the initial segment of its trajectory exhibit a uniform distribution. When the particle's velocity significantly decreases, photon emission drops markedly, with the vast majority of photons being emitted within the first half of the trajectory.
- From Fig 4.5, after traveling some distance, the probability of photons deviating from the Cherenkov angle gradually increases due to multiple scattering. As illustrated in the figure, when electrons undergo multiple scattering, their direction changes significantly, as Fig 4.6 shown. However, when calculating the Cherenkov emission angle, we still use the initial incident direction, thereby producing photons emitted at angles far from the ideal Cherenkov angle.
- In this case, we get the Cherenkov emmision profile ( $g(p, s, \theta)$ ) which describes the proportion of Cherenkov photons emitted at specific locations and directions along the trajectory of a charged particle with a given energy, relative to the total number of emitted photons. For the convenience of research, we use momentum ( $p$ ) instead of energy ( $E$ ).

Through Gaussian fitting as shown in Fig 4.7(a) in simulation, we obtain the total number of photons emitted at various energies and calculate the Cherenkov photon yield. After linear fitting, we obtain the relationship between light yield and momentum:  $\phi(p) = 1182 \times p - 956$ .

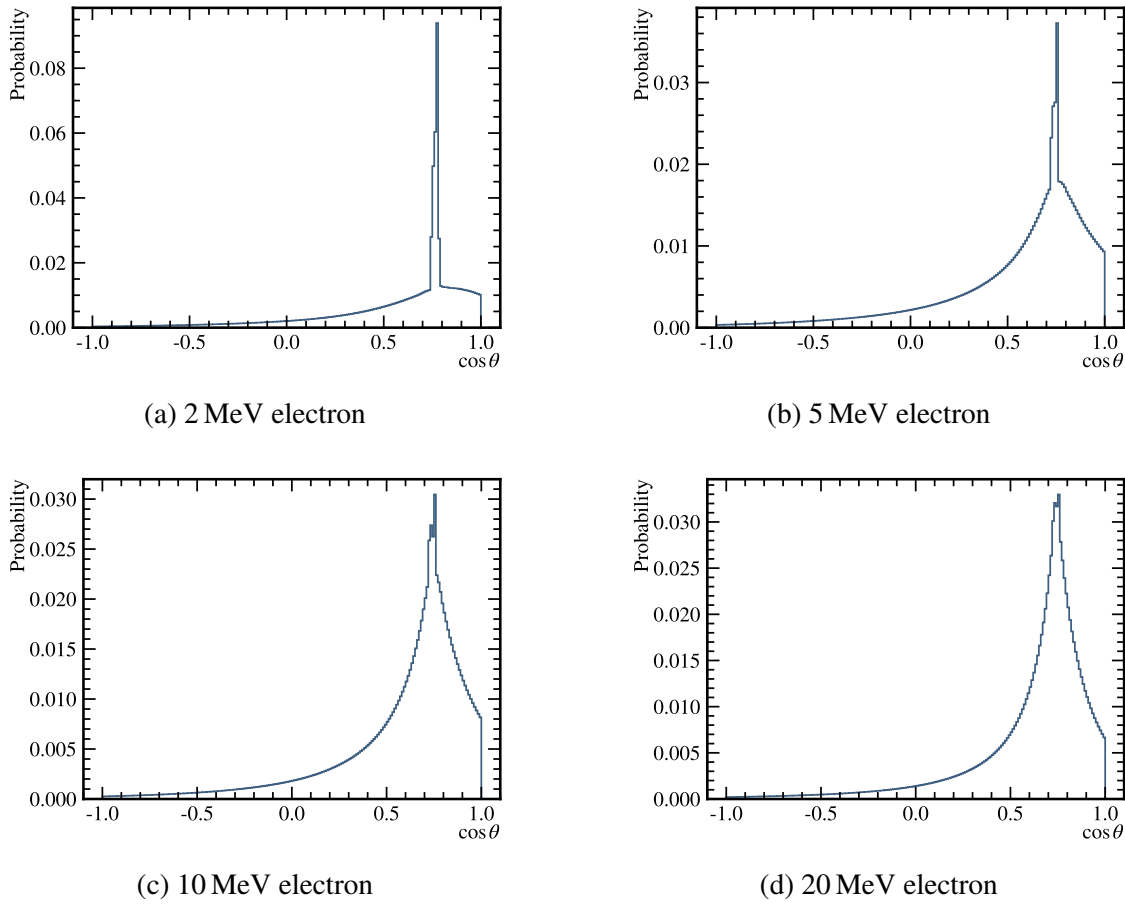


Figure 4.3 The relationship of emission probability with  $\cos \theta$ .

#### 4.2.2 The calculation of direct light

After establishing the coordinate system, we can readily determine the number of photons received by a specific PMT when an electron is incident.

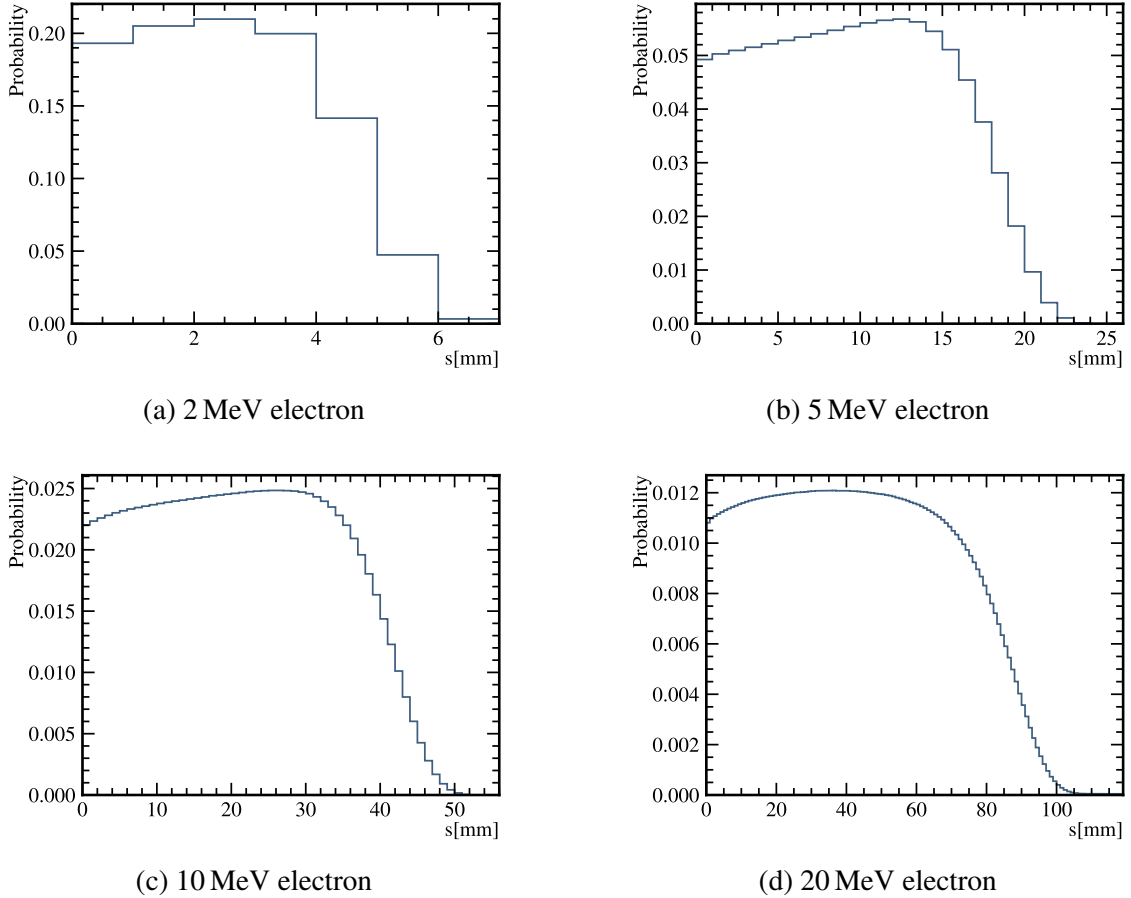
$$\mu_{\text{dir}} = \int dsg(p, s, \cos \theta) \phi(p) \Omega(R) T(R) \epsilon(\eta) \quad (4.3)$$

- $R$  is the distance between the position of electron and the PMT.
  - $\Omega(R)$  is the solid angle factor of PMT.
  - $T(R)$  is the light transmission factor.
  - $\epsilon(\eta)$  is the PMT angular acceptance of PMT, and  $\eta$  is the incident angle of light when captured by PMT.

#### 4.2.2.1 The solid angle factor

The main PMTs employed in JUNO are 20-inch with a radius of  $a = 10.622\text{m}$ . And we can calculate the solid angle of PMT by Eq. (4.4).

$$\Omega(R) = \frac{\pi a^2}{4\pi(R^2 + a^2)} \times (4\pi) = \frac{\pi a^2}{R^2 + a^2} \quad (4.4)$$


 Figure 4.4 The relationship of emission probability with  $s$ .

In this approximation, the geometric shape of the PMT is ignored and approximated by a circular wafer. This approximation remains valid only when PMTs are sufficiently distant from the particle. In JUNO, PMTs are mounted at around 19.5 m , while our region of interest lies within 17.7 m. Based on SK's experience, the approximation holds effectively at radial distances  $R > 1.5$  m.

#### 4.2.2.2 The transmission factor

In our work, we just use Eq. (4.5), and the attenuation length  $L^a$  is 75 m.

$$T(R) = \exp(-R/L^a) \quad (4.5)$$

#### 4.2.2.3 PMT angular acceptance

$\epsilon(\cos \eta)$  serves as a correction term for the approximation of the PMT wafer, describing the probability of photons being received by the PMT when incident from different directions. We extracted the particles at the same distance from the PMT in the simulation and counted the number of photons received by the PMT, as shown in Fig. 4.8. We

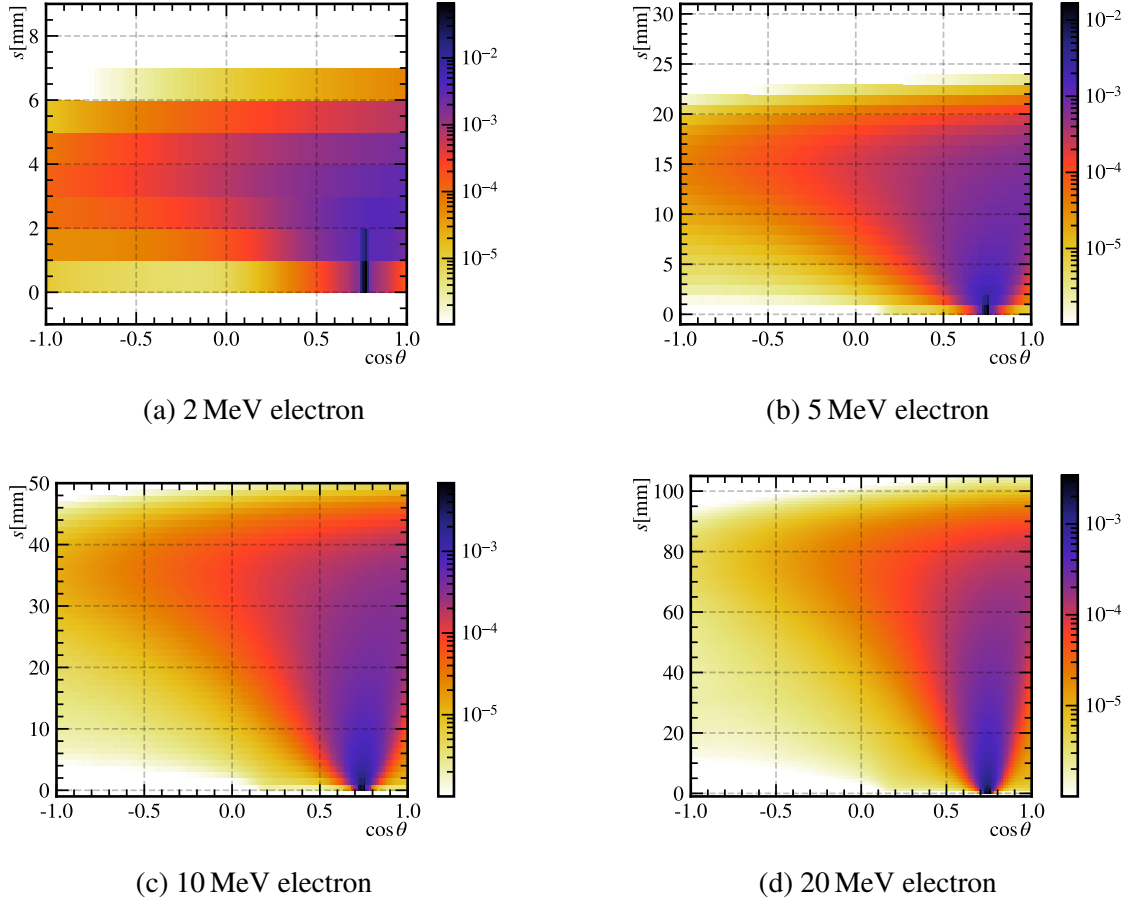


Figure 4.5 The relationship of emission probability with  $s$  and  $\cos \theta$ .

performed a "normalization" calculation of the probability using the number of photons directly incident on the PMT, as shown in Fig. 4.9(a) and 4.9(b). Then we extracted the probability distributions at different  $\cos \eta$  values and fitted them with a Gaussian distribution, as shown in Fig. 4.9(c). Thus, we obtained the variation curve of  $\epsilon(\cos \eta)$  and fitted it with a polynomial, as illustrated in Fig. 4.10. Whether it is in CD or buffer, a cut-off point can be observed. This is due to the mutual occlusion between the boundary of the detector and the PMT.

#### 4.2.2.4 The prediction of direct light

For a single photon, we can combine its propagation process and the process of being captured by the PMT and define it as the photon reception function  $J = \Omega(R)T(R)\epsilon(\eta)$ . Given the vertex and direction, this propagation process is only related to the generation position of the photon, that is, the distance from the photon generation point to the vertex. We can write  $J$  as a function of  $s$  and perform a polynomial expansion, retaining the second-order approximation, as Eq. (4.6) and the approximate performance is as shown

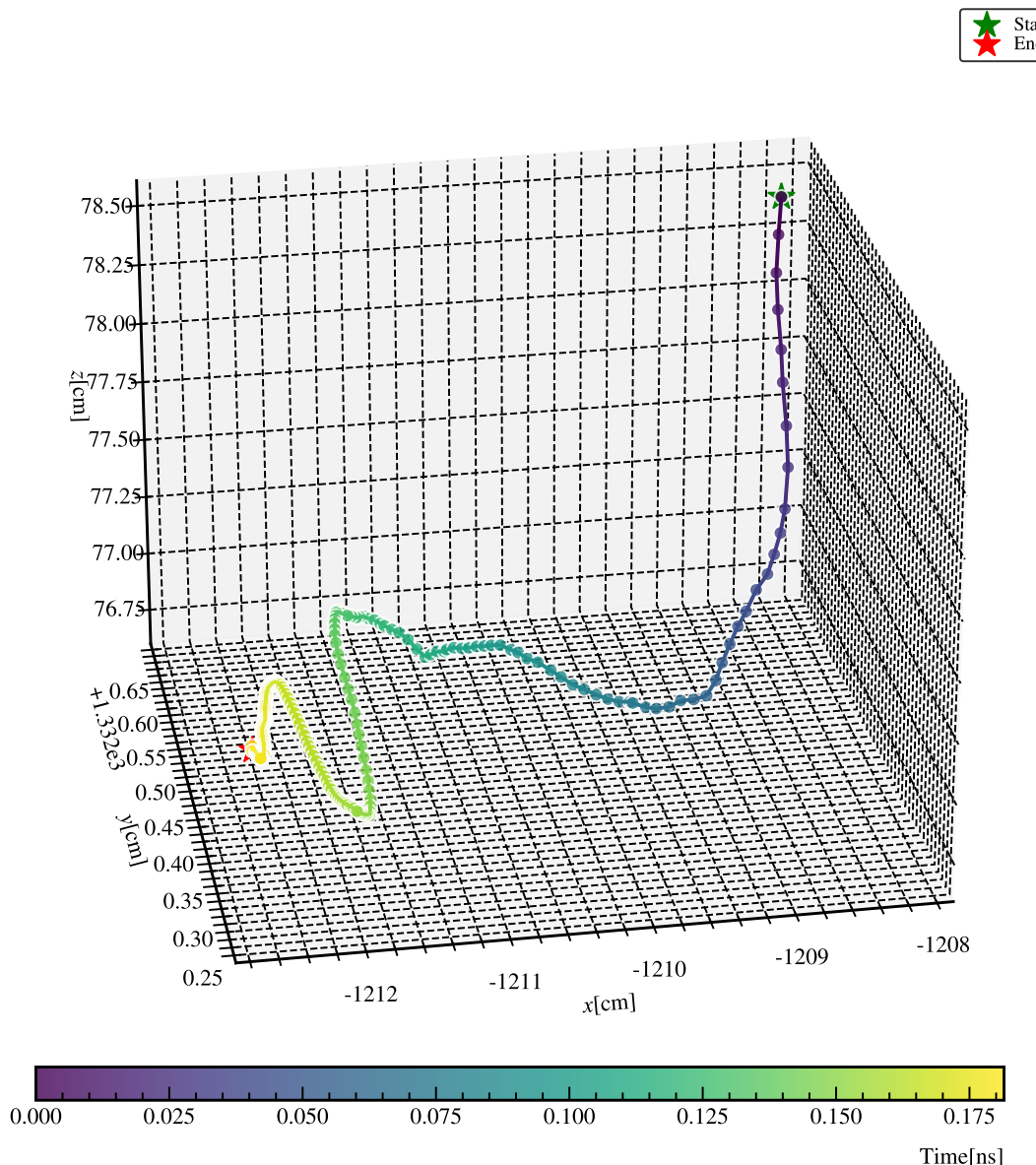
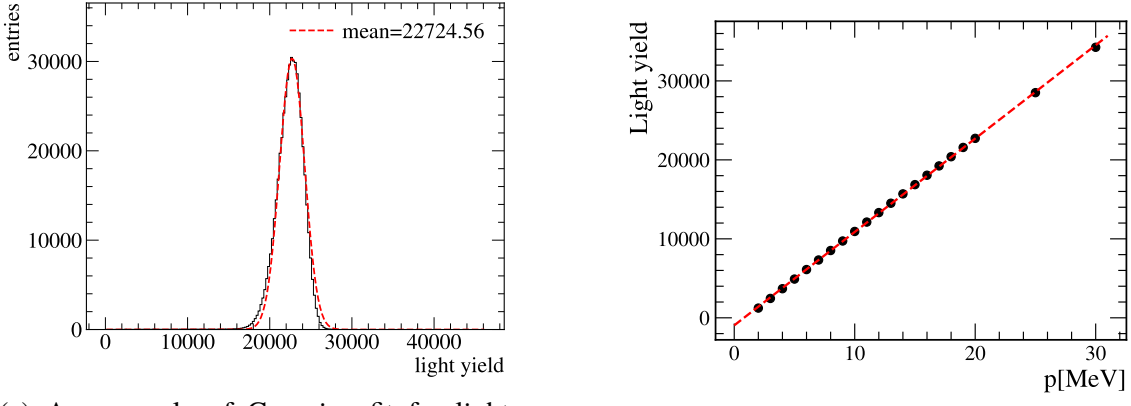


Figure 4.6 An example of a 10 MeV electron undergoing multiple scattering.



(a) An example of Gaussian fit for light yield.

(b) 5 MeV electron

Figure 4.7 The relationship of emission probability with  $s$  and .

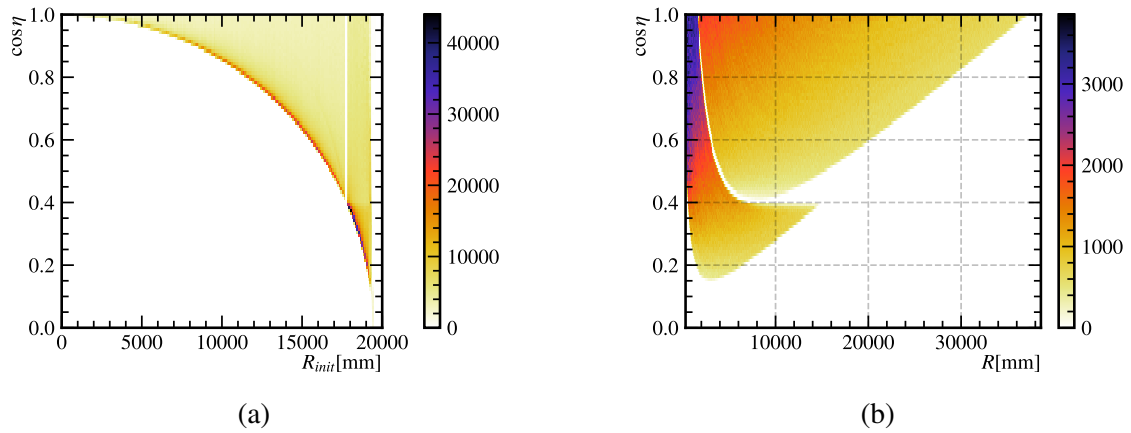


Figure 4.8 (a) is the position distribution,  $R_{init}$  is the initial position of 4 MeV electron. The boundary of the detector is at 17.7 m. There is an acrylic spherical shell with a thickness of 12 cm. The area between 17.7 and 19.5 m is the buffer. (b) shows the relationship between  $R$  and  $\cos \eta$ . The boundary of the two distributions is the acrylic spherical shell.

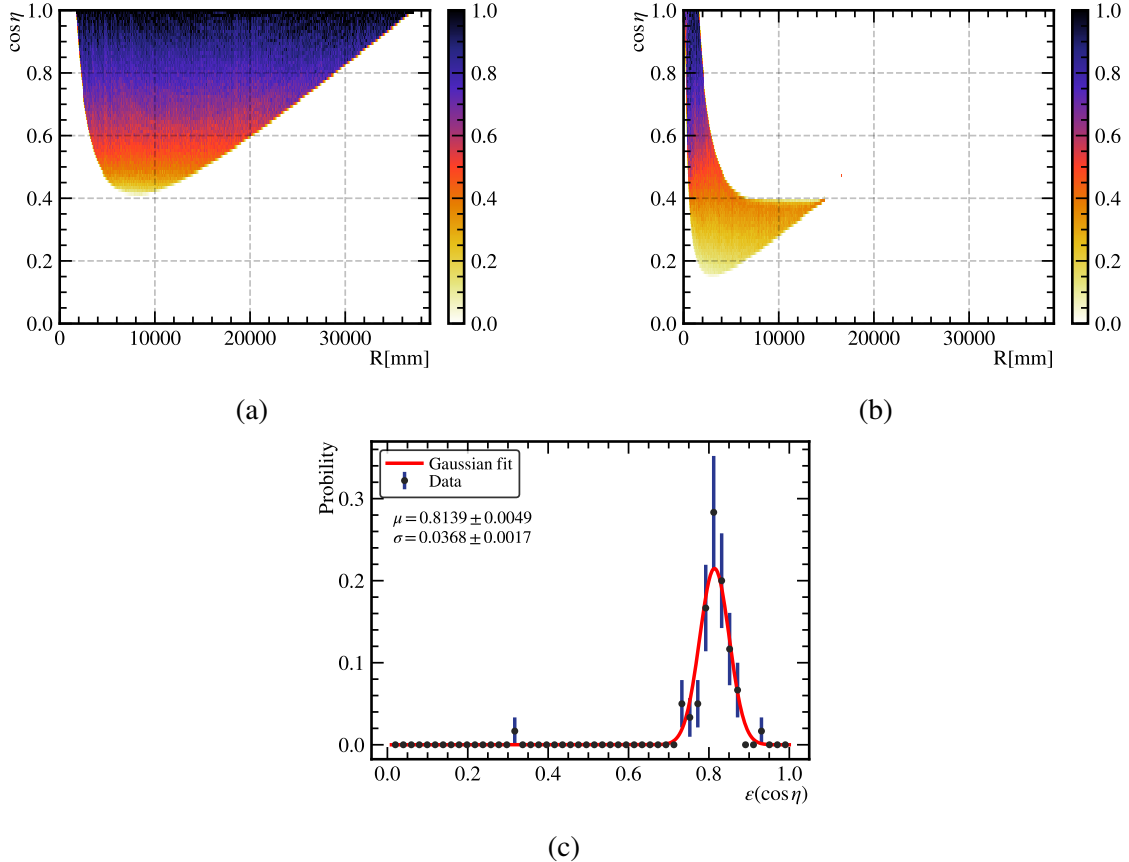


Figure 4.9 (a) and (b) are the normalized probability distribution. (c) is an example of Gaussian fit.

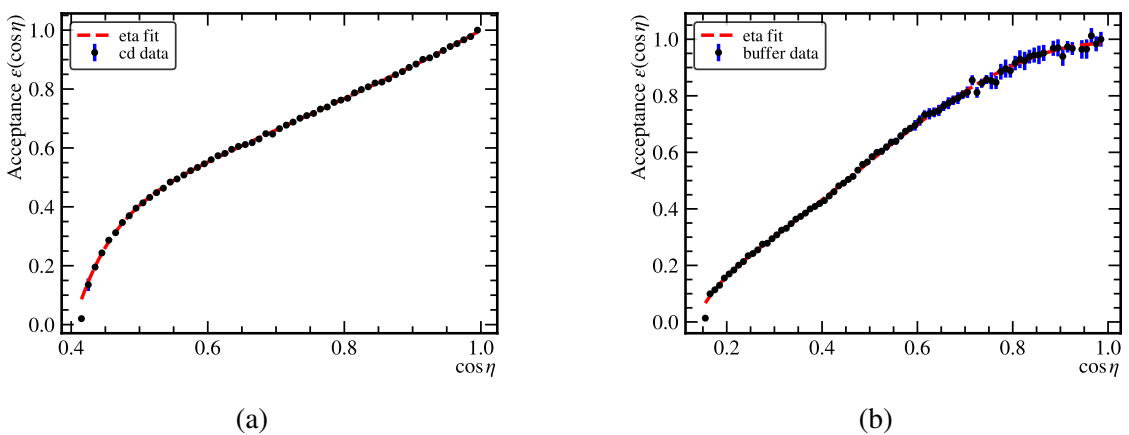


Figure 4.10 The relationship between acceptance  $\epsilon$  and  $\cos \eta$  of when event in CD (a) and in buffer (b).

in Fig. 4.11. Under this approximation, we can select 3 points to calculate the line. In the algorithm implementation, this can be quickly solved through methods such as matrix inversion.

$$J(s) = \Omega(R)T(R)\epsilon(\eta) \approx j_0 + j_1 s + j_2 s^2 \quad (4.6)$$

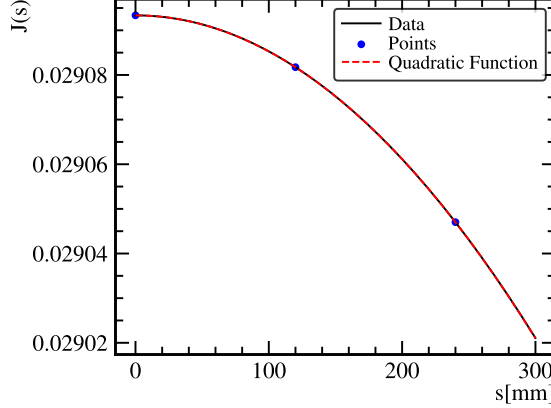


Figure 4.11 An example of second-order approximation to calculate  $J(s)$ .

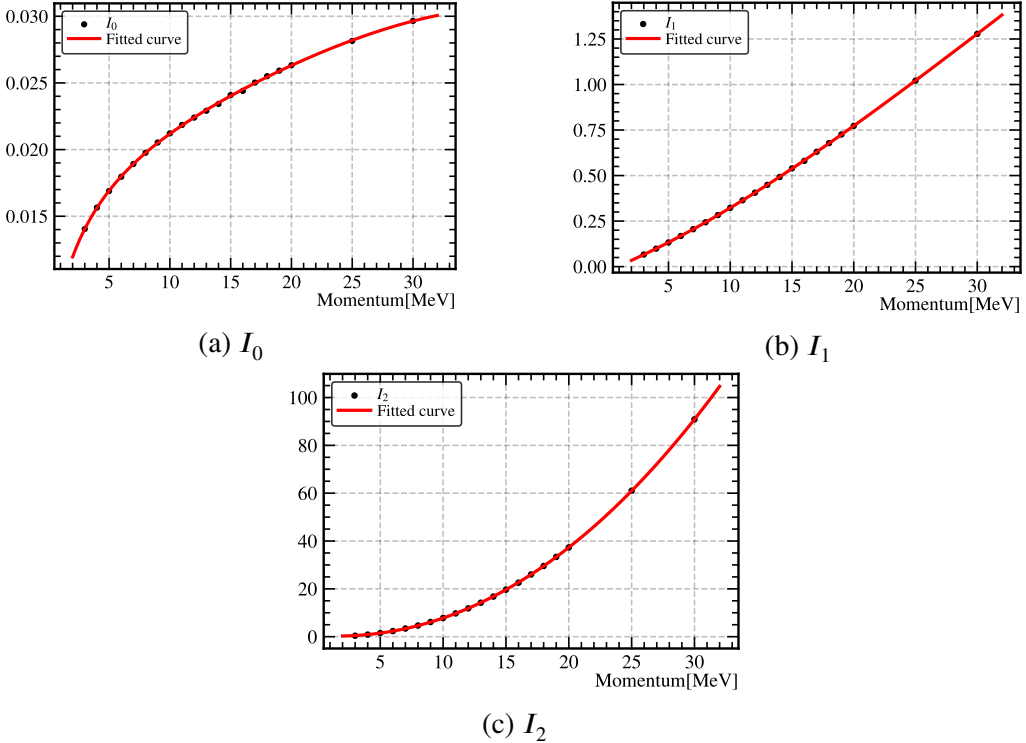
Thus far, we can decouple the process of photon generation from the process of photon capture, as shown in Eq. (4.7).

$$\begin{aligned} \mu_{\text{dir}} &= \int dsg(p, s, \cos \theta) \phi(p) \Omega(R) T(R) \epsilon(\eta) \\ &\approx \int dsg(p, s, \cos \theta) \phi(p) (j_0 + j_1 s + j_2 s^2) \\ &= \phi(p) (I_0 j_0 + I_1 j_1 + I_2 j_2) \end{aligned} \quad (4.7)$$

Where  $I_i = \int dsg(p, s, \cos \theta) s^i$  is a function of  $p, R, \cos \theta$  and represents the emission proportion of Cherenkov photons at a certain relative position. We can complete this integral calculation before the reconstruction. Due to the relatively large differences in the integration range and emission spectrum at different momenta, we calculate the value of  $I$  for each momentum. Then, we perform a polynomial approximation fitting for momentum and  $I$ , as shown in Fig. 4.12. We create a grid with the fitting coefficients in terms of  $R$  and  $\cos \theta$ . During the reconstruction process, by looking up different values of  $R$  and  $\cos \theta$  and invoking the corresponding polynomials for calculation, the reconstruction efficiency can be significantly improved.

### 4.2.3 The prediction of indirect light based on direct light

During the propagation of Cherenkov light, scattering and refraction inevitably occur. Perhaps after a long propagation process, these photons finally reach PMTs and are cap-


 Figure 4.12 The fit of  $I_i, i = 0, 1, 2$  when  $R = 15$  m,  $\cos \theta = 0.72$ 

tured. This makes it necessary to take into account the indirect photons when considering the expected number of photons. For a given vertex and momentum, we can perform an integration along the particle track for indirect light, just as we do for direct light. Since indirect light evolves from directly incident light, we can use a proportionality ratio  $A(s)$  to characterize the indirect light component.

$$\begin{aligned} \mu_{\text{ind}} &= \int dsg(p, s, \cos \theta) \phi(p) \Omega(R) T(R) \epsilon(\eta) A(s) \\ &\approx \int dsg(p, s, \cos \theta) \phi(p) (j_0 + j_1 s + j_2 s^2) A(s) \end{aligned} \quad (4.8)$$

Through ray tracing in the simulation, we are able to differentiate between direct light and indirect light. We perform binning statistics using  $R$  and  $\cos \theta$ , as shown in the Fig. ?? and 4.13(b). At the same time, it is sufficient to depict the corresponding relationship between  $A$  and the relative positions  $R$  and  $\cos \theta$  to make a scatter table, as illustrated in Fig. 4.13(c). Near the vertex and around the Cherenkov angle, the ratio of indirect light to direct light is about 0.1. When far from the vertex and the Cherenkov angle, indirect light is dominant. For low-energy electrons, the track length of their motion typically ranges from several centimeters to over ten centimeters. In the scattering table employed, the bin width of  $R$  is set to 10 cm. Under such circumstances, the approximation  $A(s) = A(s = 0)$  is highly adequate. Consequently, the integral of the indirect light can be expressed as

Eq. (4.9).

$$\begin{aligned}\mu_{\text{ind}} &\approx \int dsg(p, s, \cos \theta) \phi(p) (j_0 + j_1 s + j_2 s^2) A(s) \\ &\approx \phi(p) (I_0 j_0 + I_1 j_1 + I_2 j_2) A(s = 0)\end{aligned}\quad (4.9)$$

The final light prediction can be  $\mu_p = \mu_{\text{dir}} + \mu_{\text{ind}} = \phi(p)(I_0 j_0 + I_1 j_1 + I_2 j_2)(1 + A(s = 0))$ .

After considering the PDE of PMT, the prediction of PE should be  $\mu = \varepsilon \mu_p = \varepsilon \phi(p)(I_0 j_0 + I_1 j_1 + I_2 j_2)(1 + A(s = 0))$

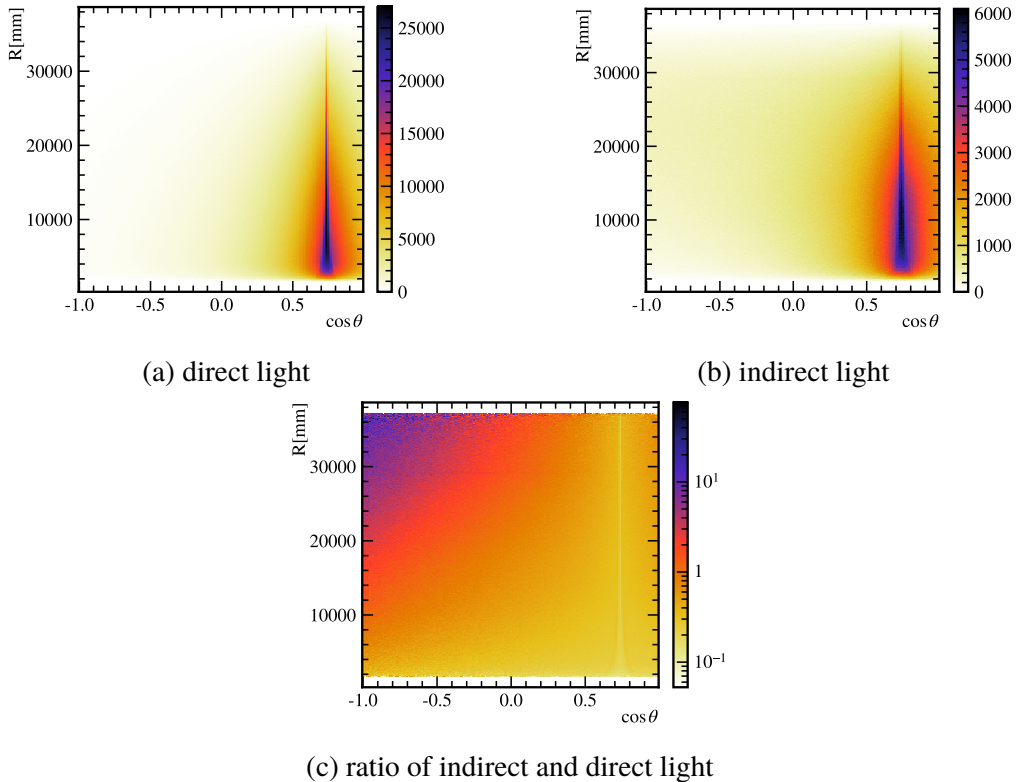


Figure 4.13 The scatter table

#### 4.2.4 The timing response

In Cherenkov reconstruction, photons are emitted along the Cherenkov angle rather than isotropically. Consequently, when only charge information is utilized for reconstruction, accurately determining the position becomes challenging. Time serves to characterize both the emission properties and the distance characteristics during propagation. To a certain degree, it offsets the limitations of relying solely on charge information. Thus, in the detector response, time is an essential parameter. As depicted in Fig. 4.14, in the reconstruction process, we employ the residual time obtained by subtracting the time of

flight, as defined in Eq. (4.10).

$$t_{\text{res},i} = t_i - t - s_{\text{mid}}/c - \frac{|\mathbf{P}_{\text{PMT}}^i - \mathbf{x} - s_{\text{mid}} \hat{\vec{d}}|}{c_w} \quad (4.10)$$

Where  $t$  is the event time,  $\mathbf{x}$  is the vertex,  $t_i$  is the hit time at  $i$ -th PMT and  $\mathbf{P}_{\text{PMT}}^i$  is the position of  $i$ -th PMT. In fiTQun, following the classification of the residual time of the

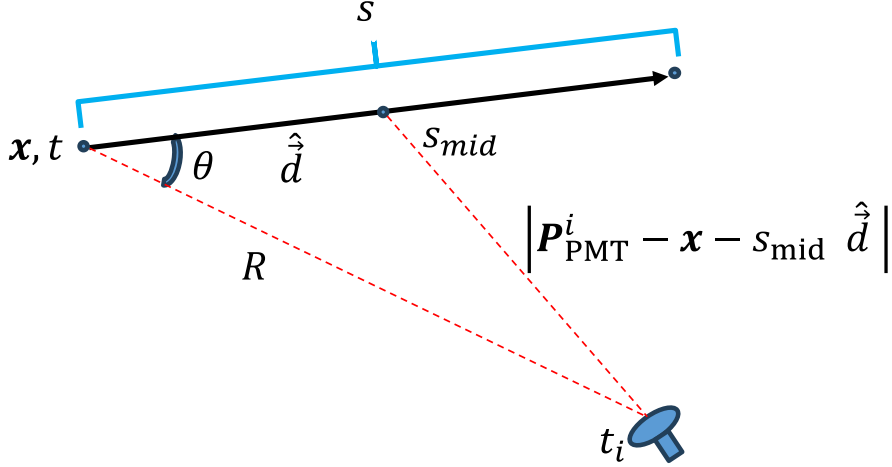
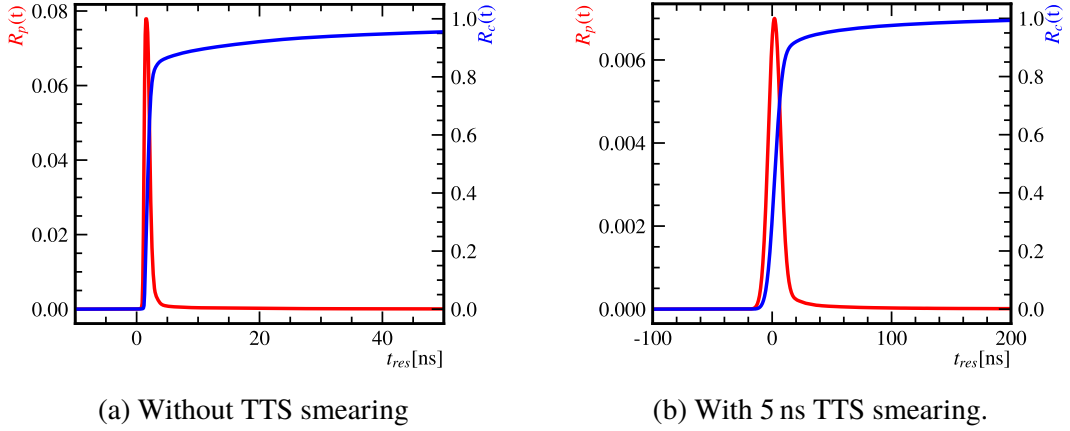


Figure 4.14 The definition of residual time.

direct light according to the expected number, the mean and standard deviation of the residual time distribution are derived through Gaussian fitting. Subsequently, the means and variances under different expectations are fitted to accomplish the parameterization of the time response. However, this approach is not conducive to considering factors such as TTS. In this study, we directly classify the residual time using the relative distance, approximate the probability density function ( $R_p(t)$ ) with a histogram, and carry out integration to obtain the corresponding cumulative distribution function ( $R_c(t)$ ), as shown in Fig. 4.15(a). Analogously, by leveraging the histogram, we accomplished the time smearing of the TTS response through convolution, as depicted in Fig. 4.15(b). Given that the maximum TTS of the PMT can attain up to 15 ns, we carried out the time convolution smearing for the TTS within the range of 0–15 ns.

#### 4.2.5 The DCR in reconstruction

From PMT calibration in Sec. 3.2, the DCR is determined to be exceedingly high. In the course of the reconstruction process, considering that the dark noise adheres to a homogeneous Poisson intensity process within the time window, the probability of occurrence within a unit time window can be approximated by DCR. Given an intensity of  $b$ , the predicted PE should be  $\mu + b(\bar{t} - t)$ , and the time PDF should be  $f_t(t_i) = \mu R_p(t_{\text{res},i}) + b$ .


 Figure 4.15 The PDF and CDF of  $t_{\text{res}}$ .

And our likelihood is as shown in Eq. (4.11).

$$\begin{aligned} \mathcal{L} = \prod_{j \in \{N_j > 0\}} \frac{1}{(N_j - 1)!} & \exp \left[ -\mu_j (R_c(\bar{t}_{\text{res},j}) - R_c(t_{\text{res},j})) - b(\bar{t}_{\text{res},j} - t_{\text{res},j}) \right] \\ & \times (\mu R_p(t_{\text{res},j}) + b) \quad \times \left( \mu (R_c(\bar{t}_{\text{res},j}) - R_c(t_{\text{res},j})) + b(\bar{t}_{\text{res},j} - t_{\text{res},j}) \right)^{N_j - 1} \quad (4.11) \\ & \times \prod_{j \in \{N_j = 0\}} \exp \left[ -\mu (R_c(\bar{t}_{\text{res},j}) - R_T(t_{\text{res},j})) - b(\bar{t}_{\text{res},j} - t_{\text{res},j}) \right] \end{aligned}$$

#### 4.2.6 Use MCMC for extremization

To avoid the influence of local extrema, we use Markov Chain Monte Carlo (MCMC) for extremization<sup>[54]</sup>. To expedite convergence, we employ the simulated annealing method<sup>[55]</sup>. Specifically, we anneal the TTS from 50 ns to the actual calibrated result in Sec. 3.3. In each event, we sample a total of 3,000 steps. We use the results of the last 300 steps and calculate the average as the reconstruction result.

#### 4.2.7 The preliminary reconstruction

Prior to the likelihood-based reconstruction, a faster preliminary reconstruction based on timing information and gridded vertex map is performed to reject unphysical events to reduce the data volume. In the preliminary reconstruction, two parameters are defined:

- score: Dark noise event filter based on residual time distribution and charge-weighted vectors from CD center to PMTs. The closer score is to 0, the more likely the event is a dark noise event
- isglass: Glass radioactive event filter developed from the decision tree. Its range is from 0 to 1, and the closer the result is to 1, the more likely the event is a glass radioactive event.

## 4.3 The parameters definition

### 4.3.1 The energy related parameters

For a more accurate description, we define several parameters as shown in Fig. 4.16.

- $n_{10}$ : The maximum count of residual time  $t_{\text{res}}$  within a 10 ns bin width
- $n_b$ : The average count of  $t_{\text{res}}$  in [-20, -10] and [30,40]ns.
- $n_{20}$ : The total count of  $t_{\text{res}}$  in [-20, 20]ns, it is the primary estimation of energy.
- $n_c$ : The count of  $\cos \theta$  in [0.65, 0.85], and the definition of  $\theta$  is shown in Fig. 4.2.

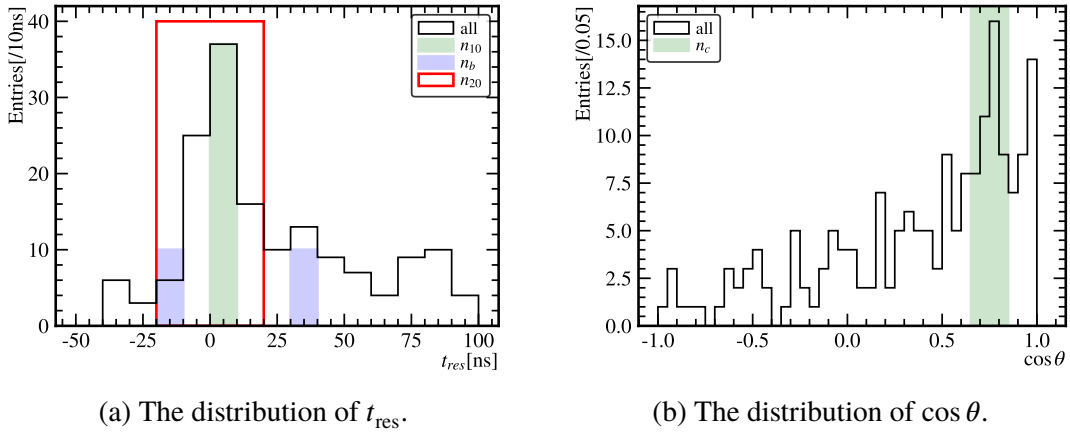


Figure 4.16 The definition of parameters related to energy.

### 4.3.2 The parameters for reconstruction quality

There exist two types of background, which can exert a significant impact on our analysis. These include the trigger stemming from pure dark noise and the events originating from PMT radioactivity. To eliminate these backgrounds, we introduce several parameters. To comprehensively assess the performance of each parameter, we simulate the uniform distribution of 2.2 MeV Gamma, radioactive events from PMTs, and dark noise trigger events within the detector. Subsequently, reconstruction is performed following the MM trigger.

#### 4.3.2.1 Kurtosis test ( $k$ )

The value obtained from the Kurtosis test on the residual time distribution is employed to assess the quality of the signal. In the case where the trigger originates from dark noise, the value should be -1.

### 4.3.2.2 Akaike Information Criterion

Akaike Information Criterion (AIC) is frequently employed in model selection<sup>[56]</sup>. In the context of reconstruction, it is utilized to determine whether the trigger originates from noise or a physical event. This Criterion is defined as Eq. (4.12)

$$\begin{aligned} \text{AIC}_v &= -2 \ln \mathcal{L}_v + 2k_p \\ \text{AIC}_0 &= -2 \ln \mathcal{L}_0 \end{aligned} \quad (4.12)$$

Where  $\mathcal{L}$  represents the likelihood of the event with a single vertex, and  $k_p$  denotes the number of reconstructed parameters. During the reconstruction process, we also calculate the likelihood of non-vertex events ( $\mathcal{L}_0$ ). In this scenario, we can obtain the AIC criterion:

$$\delta A = \text{AIC}_v - \text{AIC}_0 = 14 - 2 \ln \mathcal{L}_v + \ln \mathcal{L}_0 \quad (4.13)$$

By comparing  $\delta A$  of dark noise events and 2.2 MeV Gamma events, it can be seen that most dark noise events are eliminated, while less than 10 % of Gamma events are removed.

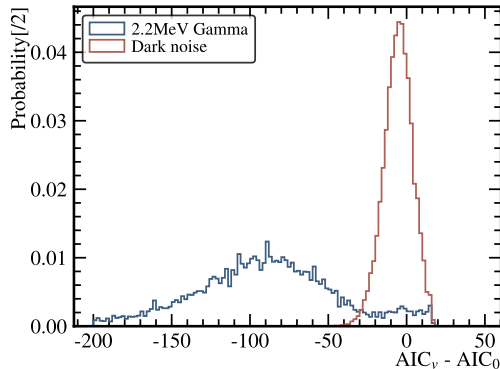


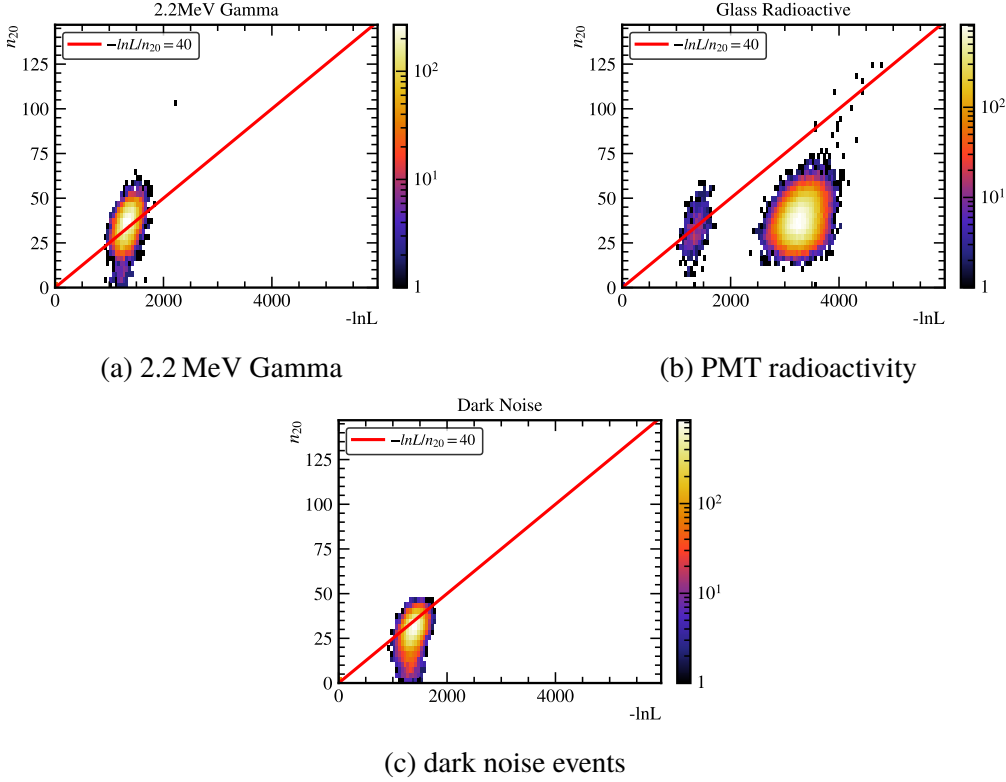
Figure 4.17 There is obvious difference between dark noise and 2.2 MeV Gamma. We can optimize it to remove dark noise events.

### 4.3.2.3 The likelihood-energy combined Criterion

We define the likelihood-energy combined criterion as  $LE$ , as shown in Eq. (4.14)

$$LE = -\ln \mathcal{L}/n_{20} \quad (4.14)$$

This criterion is employed to eliminate events stemming from PMT radioactivity. When the cut  $LE < 40$  is applied, over 99.99 % of the events from PMT radioactivity are removed, along with approximately 30 % of the 2.2 MeV Gamma.


 Figure 4.18 The relationship between  $\mathcal{L}$  and  $n_{20}$ .

#### 4.3.2.4 The goodness of reconstruction

When contemplating reconstruction, it is essential to assess the quality of both position and direction. In the case of a successfully reconstructed position, the residual time should be distributed as closely as feasible around zero. For precise direction reconstruction, PMTs adjacent to the Cherenkov ring ought to demonstrate uniform photon acceptance. In accordance with these criteria, we formulate the following two goodness metrics, presented as Eq. (4.15). Finally, we combine these two metrics to obtain the overall goodness of reconstruction, denoted as  $G_{vd} = g_v^2 - g_d^2$ .

$$g_v = \frac{\sum e^{-0.5(t_{\text{res}}/w)^2} e^{-0.5(t_{\text{res}}/\sigma)^2}}{\sum e^{-0.5(t_{\text{res}}/w)^2}} \quad (4.15)$$

$$g_d = \frac{1}{2\pi} \left[ \max \left( \phi_i - \frac{2i\pi}{N} \right) - \min \left( \phi_i - \frac{2i\pi}{N} \right) \right]$$

- $w$  and  $\sigma$ : in this work,  $w = 20$  ns and  $\sigma$  is the TTS of PMT.
- $g_v$ : The goodness of position reconstruction.
- $g_d$ : The goodness of direction, describes the uniformity of the azimuthal angle distribution, as shown in Fig. 4.19.

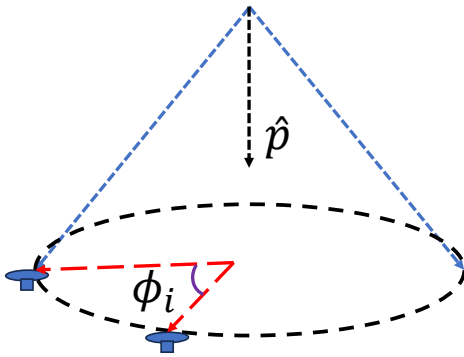


Figure 4.19 The definition of azimuthal angle in the goodness of direction calculation.

#### 4.4 The performance of reconstruction in simulation

To assess the performance of reconstruction, we simulated electrons and 2.2 MeV gamma rays and computed the resolution. The information regarding the simulated electrons and Gamma is shown in Table 4.1. The simulation is conducted based on JUNO software, version J25.1.5. In order to be as close to the actual situation as possible, we update the DCR obtained from the calibration in Sec. 3.2 into the simulation.

Table 4.1 Particles used in simulation

Particle	Energy (MeV)	Distribution
$e^-$	2, 3, 4, 5, 6, 8, 10, 15, 20	Uniformly in CD
Gamma	2.2	Uniformly in CD

We define the 68.3 % quantile of the distribution of  $R_{diff}$  as position resolution, and the 68.3 % quantile of the distribution of  $\theta_{diff}$  as angle resolution, as shown in Fig. 4.21. For 2.2 MeV Gamma, the position resolution is 1.97 m and direction resolution is 43.82°. It indicates that during the JUNO water phase, we can reconstruct Gamma rays of 2.2 MeV. That is to say, we can still reconstruct the n-H capture signal well even though the DCR is pretty high.

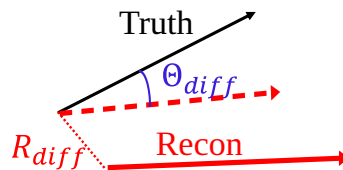


Figure 4.20  $R_{diff}$  is the distance between reconstructed position and true position,  $\theta_{diff}$  is the angle between reconstructed direction and true direction.

After calculation the resolution of different electrons, we get the relationship between

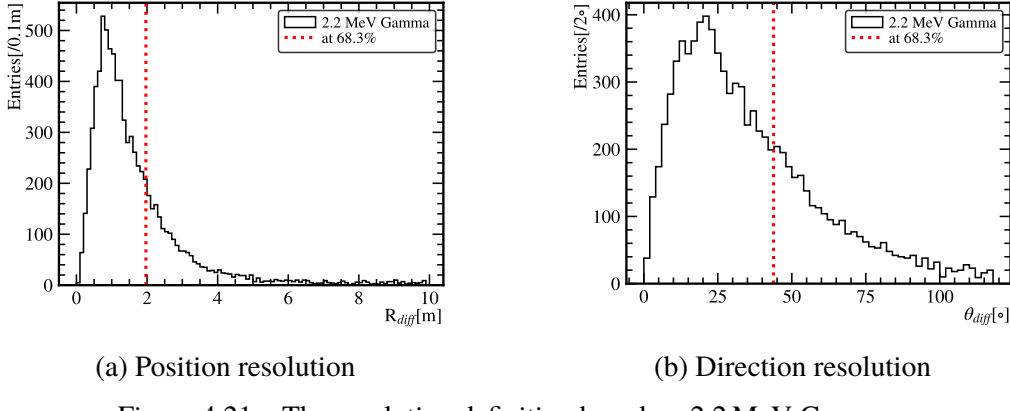


Figure 4.21 The resolution definition based on 2.2 MeV Gamma.

resolution and electron kinetic energy, as exhibited in Fig. 4.22(a) and Fig. 4.22(b). When compared to the position resolution of SK-IV, the position resolution in the water phase of JUNO is relatively lower. This can be attributed to the fact that the PMTs in JUNO exhibit a higher DCR and poorer TTS. At the low-energy regime, a comprehensive modeling of the charge response of Cherenkov has been conducted, resulting in improved directional resolution than SK-III (SK-IV's direction resolution is the same as SK-III).

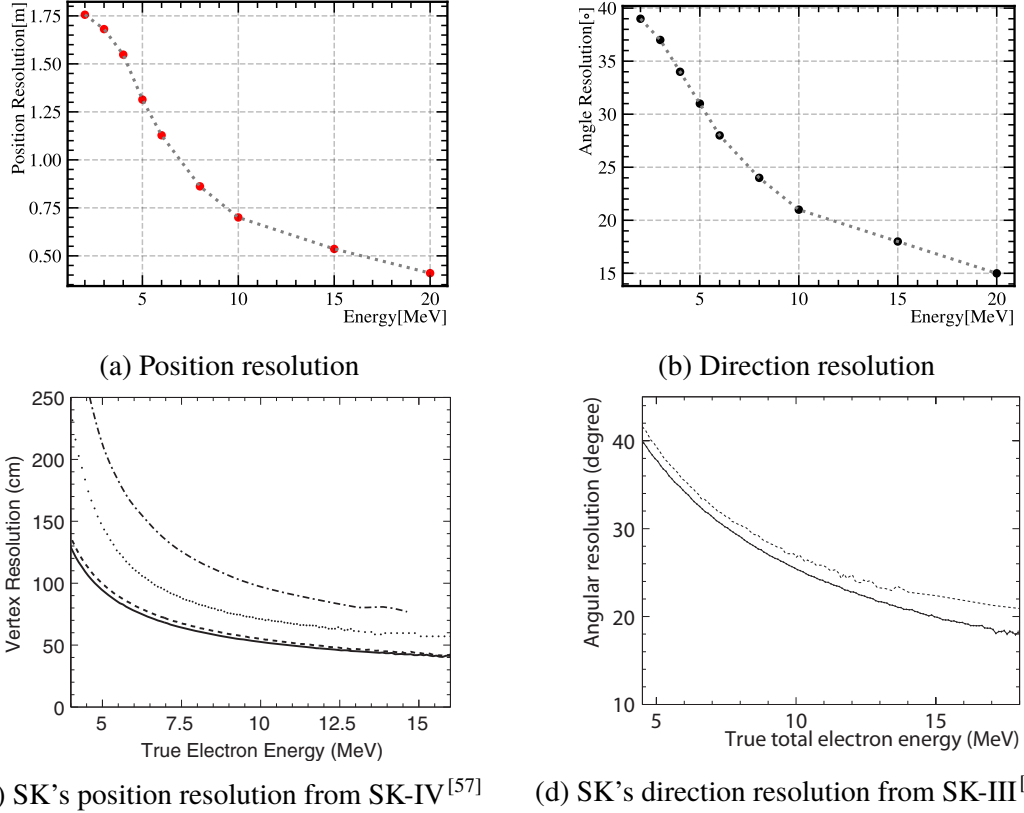
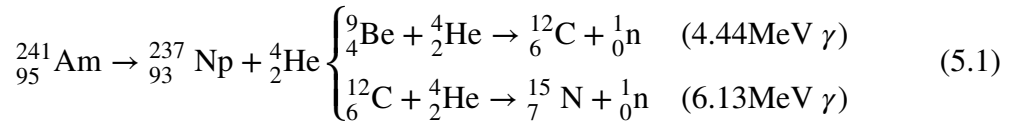


Figure 4.22 The relationship between resolution and energy of electrons.

# CHAPTER 5 THE SOURCE CALIBRATION IN WATER PHASE

## 5.0.1 The calibration information

Americium-Beryllium (AmBe) and Americium-Carbon (AmC) neutron sources serve as critical reference standards for characterizing neutron detecting capabilities. Both sources leverage the alpha decay of  $^{241}\text{Am}$ . The neutron producing process can be described as Eq. (5.1):



During the water phase, neutron source calibration was performed three times, and the summary of 14 runs are in Table. 5.1. All the calibration sources were placed along

Table 5.1 The neutron source calibration in water phase

Calibration	Date	Configuration
First	02/02	AmC, threshold=53, Run 3279, 3281, 3283, 3286, 3293
Second	02/03	AmBe, threshold=53, Run 3333, 3335, 3338, 3340, 3342
Final	02/07	AmBe, threshold=46.5, Run 3660, 3663, 3671; AmC, threshold=44, Run 3675

the z-axis, as Fig. 5.1 shown. To enhance our capability in studying low-energy events in water phase, we decouple and analyze prompt and delayed signals separately during the calibration source analysis.

## 5.1 JUNO's low-energy threshold in water phase

### 5.1.1 The reconstruction of the prompt signals

#### 5.1.1.1 The event selection before reconstruction

In this study, we take Run 3671 (calibrated with a AmBe source at the position of  $(0, 0, -10\text{ m})$ ) as an illustrative example. To mitigate the data volume, we selectively choose a subset of events from the previous findings (JUNO-doc-12539) based on Baona's

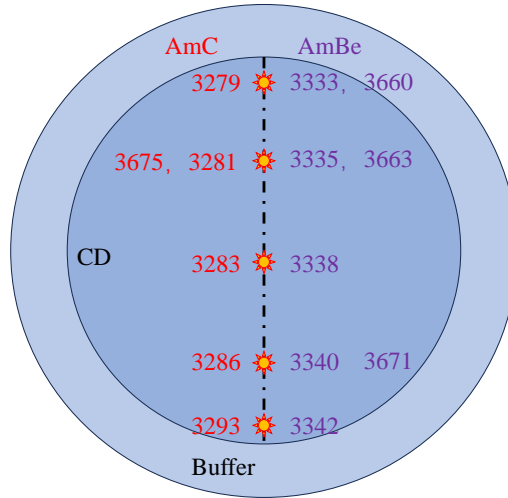


Figure 5.1 The calibration source positions in water phase.

reconstruction method. Additionally, partial background events are filtered out. After applying a fiducial volume of 17 m cut, we observed that a large number of events were downward, as depicted in Fig. 5.2.

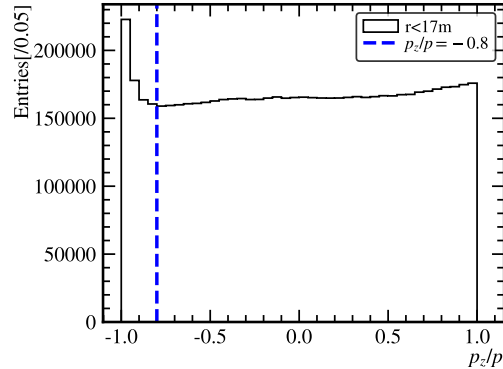


Figure 5.2 The distribution of  $p_z/p$  after applying a fiducial volume of 17 m cut.

We require additional directional cuts. Therefore, our selection criteria are as follows.

- Fiducial volume  $r < 17 \text{ m}$
- $\text{isglass} < 0.5$
- $\text{score} > 0.001$
- $p_z/p > -0.8$
- $n_{20} > 12$

To demonstrate the events selection during the cut process, we apply a cylindrical cut with a radius of 2 m along the z-axis and plot the z-coordinate distribution of events as shown in Fig. 5.3.

After event selection, additional constraints are applied to the PMT photoelectron

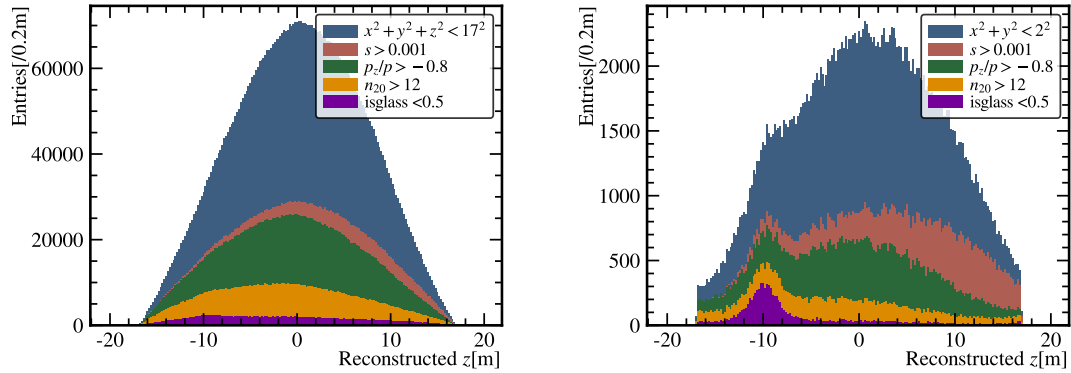


Figure 5.3 The distribution of z-coordinate in Run 3671. () shows the distribution without cylindrical cut, while () shows the distribution after the cut.

(PE) timing distribution. The PE times are binned with a width of 48 ns over the interval  $t \in [96, 576]$ ns. A 180 ns reconstruction window is then defined, comprising 36 ns before and 144 ns after the maximum bin within the search range, as illustrated in Fig. 5.4. This selection effectively suppresses dark noise contributions and improves the robustness of the vertex reconstruction.

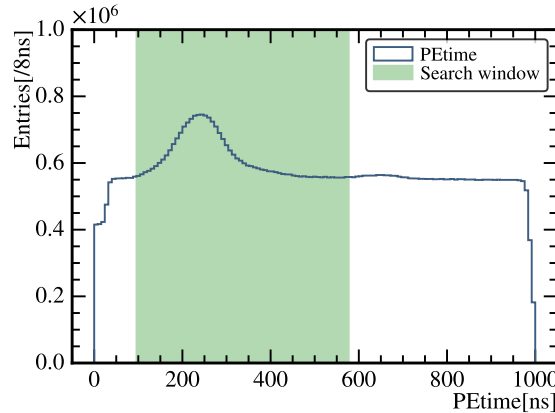


Figure 5.4 The PE time distribution in Run 3671. We search the maximum bin in the green range and select a 180 ns time window for reconstruction.

### 5.1.1.2 The position distribution of the prompt signals

The prompt signal reconstruction employs the maximum likelihood method described in Sec. 4.1. Subsequently, quality and background rejection cuts are applied to remove events with poor reconstruction performance and residual background contamination. The specific cuts are as follows:

- Fiducial volume:  $r < 16.5\text{m}$
- Unknown downwards events:  $p_z/p > -0.8$
- Signal quality:  $k > -0.85$

- Energy related:  $n_{10} - n_b > 15$  and  $n_c > 8$

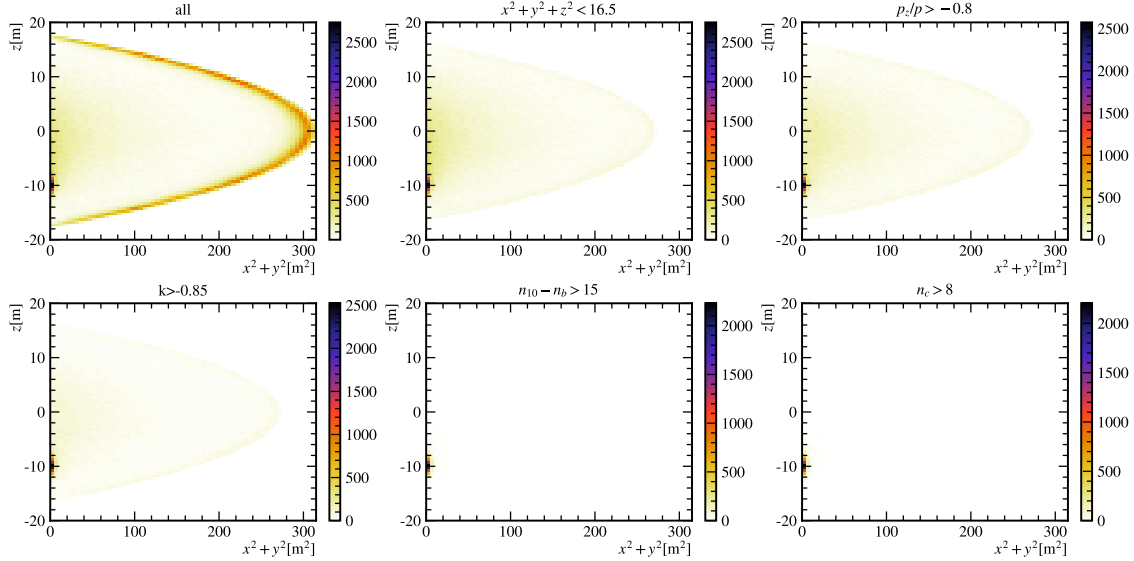


Figure 5.5 The position distribution of the prompt signals in Run 3671.

After these selection cuts, pronounced event clustering is visible near the calibration source position. Furthermore, applying a 2 m cylindrical cut along the z-axis yields a prominent peak at  $z = -10$  m in the reconstructed event distribution, as shown in Fig. 5.6.

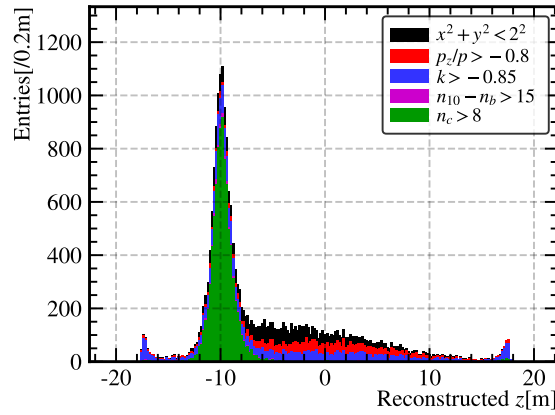


Figure 5.6 The distribution of z-coordinate in Run 3671 after 2 m cylindrical cut.

Applying the same selection cuts and analysis procedure, the reconstructed vertex position distributions of prompt signals are obtained for 14 calibration runs. As shown in Fig. 5.7, prompt signals from both AmC and AmBe sources are accurately reconstructed at their deployment positions, validating the performance of the position reconstruction algorithm. These results further demonstrate that JUNO's water phase is capable of detecting 6.1 MeV and 4.4 MeV Gamma signals with high statistical significance.

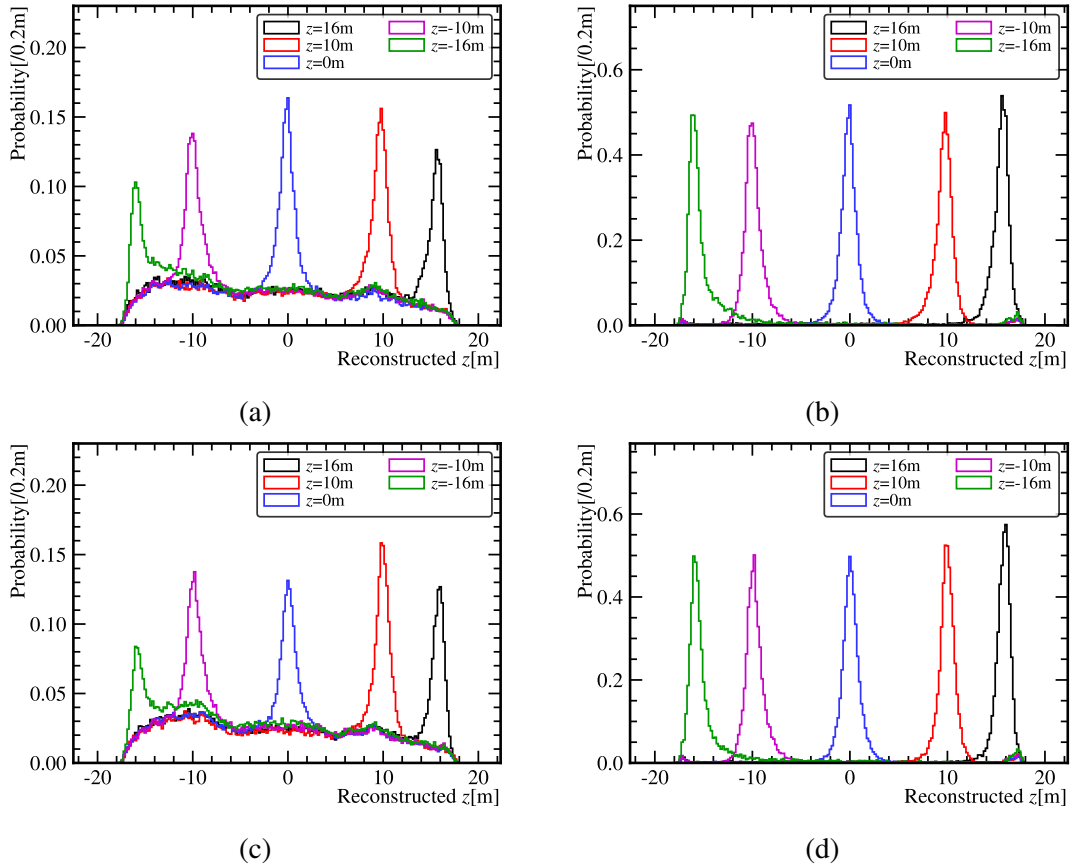


Figure 5.7 The distribution of z-coordinate in AmC and AmBe source calibration. (a) and (c) show the distribution without cylindrical cut, while (b) and (d) show the distribution after the cut of 2 m cylinder along the z-axis. (a) and (b) are the results of AmC source calibration, and (c) and (d) are the results of AmBe source calibration respectively.

### 5.1.1.3 The energy distribution of prompt signals

To obtain the energy spectrum of the prompt signals, all events within a 3 m radius of the calibration source position are selected, as shown in Fig. 5.8. To account for the influence of the background energy distribution, data collected under identical conditions but without a calibration source at the same location are used. For Run 3671, the background spectrum is derived from Run 3663. To mitigate the impact of differing data acquisition durations, the energy spectra are normalized to live time, allowing event rates to serve as the primary comparison metric. As shown in Fig. 5.9(a), substantial background contamination remains in the energy spectrum despite the application of selection cuts. After background subtraction, the  $n_{20}$  distribution for 4.4 MeV Gamma events is obtained. Similarly, for Run 3286, which utilizes an AmC source, the background spectrum is derived from Run 3281. The  $n_{20}$  distribution for 6.1 MeV Gamma events is shown in Fig. 5.9(b).

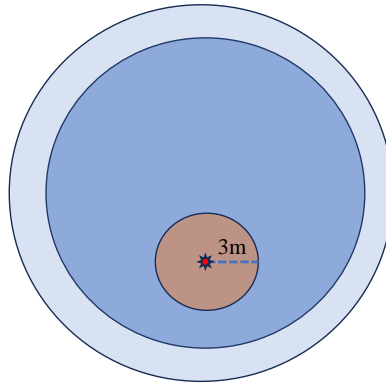


Figure 5.8 3-meter radius cut around the calibration source position

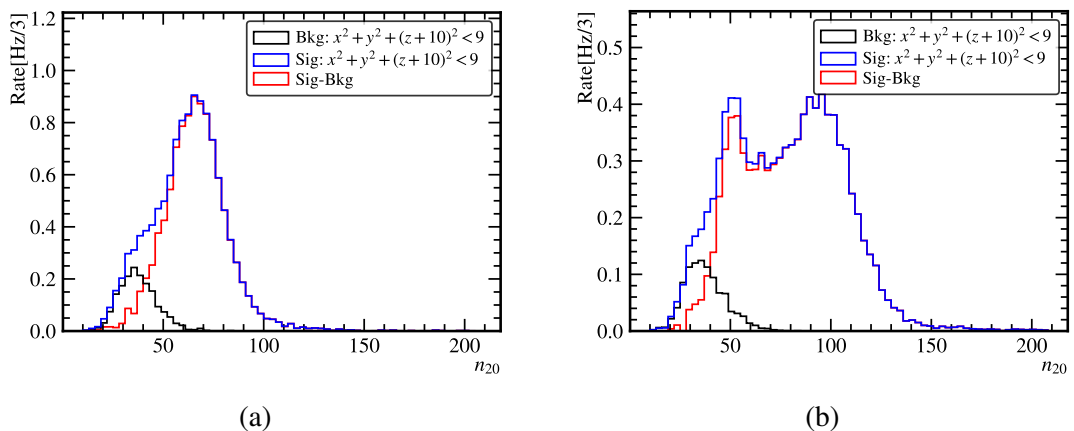


Figure 5.9 The energy distribution of prompt signals. The black line represents the background energy distribution, the blue line represents the energy distribution of prompt signals, and the red line represents the prompt signal energy distribution after subtracting the background. (a) is the result of Run 3671, representing the energy distribution of 4.4 MeV Gamma. (b) is the result of Run 3286, representing the energy distribution of 6.1 MeV Gamma.

## 5.1.2 The search for delayed signals

### 5.1.2.1 The reconstruction of delayed signals

After applying the aforementioned selection criteria, prompt signal candidates are identified. We then investigate the delayed signals arising from neutron capture events. To reconstruct these delayed signals while reducing data volume, a coincidence reconstruction algorithm is employed. As shown in Fig. 5.10, a 1000 us time window is used for delayed signal reconstruction. For the study of accidental coincidence backgrounds, additional events are reconstructed within the 1000–2000 us interval.

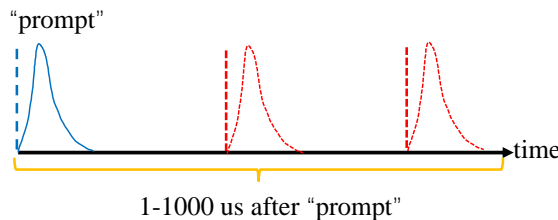


Figure 5.10 The delayed signal reconstruction time window.

### 5.1.2.2 The search for delayed signals

After the delayed signal reconstruction, we apply the following criteria to select delayed signals:

- The selection of prompt signals:
  - Energy related cut:  $n_{10} - n_b > 15$ .
  - Directional cut:  $p_z/p > -0.8$ .
  - Distance to the source:  $< 3$  m.
  - Muon veto:  $> 500$  us.
  - Background cut:  $\delta A < -50$ ,  $LE < 40$ .
- The selection of delayed signals:
  - Energy related cut:  $32 < n_{20} - n_b < 70$ .
  - Coincident distance  $dR < 6$  m.
  - Directional cut:  $p_z/p > -0.8$ .
  - muon veto:  $> 500$  us.
  - Coincident time:  $dT < 1000$  us.
  - Background cut:  $\delta A < -50$ ,  $LE < 40$ .

Following the series of selection procedures, an exponential fit,

$$f(t) = A \exp(-t/\tau) + c \quad (5.2)$$

is performed on the coincidence time distribution between prompt and delayed signals, as shown in Fig. 5.11. The extracted neutron capture lifetime is  $203 \pm 24 \mu\text{s}$ , in agreement with theoretical expectations within experimental uncertainties. In parallel, the position distributions of both prompt and delayed signals are examined. As illustrated in Fig. 5.12, events are strongly clustered around the calibration source location, consistent with the deployment geometry. These results demonstrate that the JUNO detector exhibits robust neutron detection capability during the water phase.

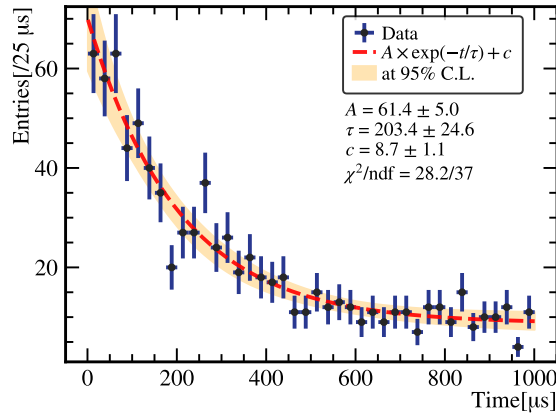


Figure 5.11 The coincident time fit.

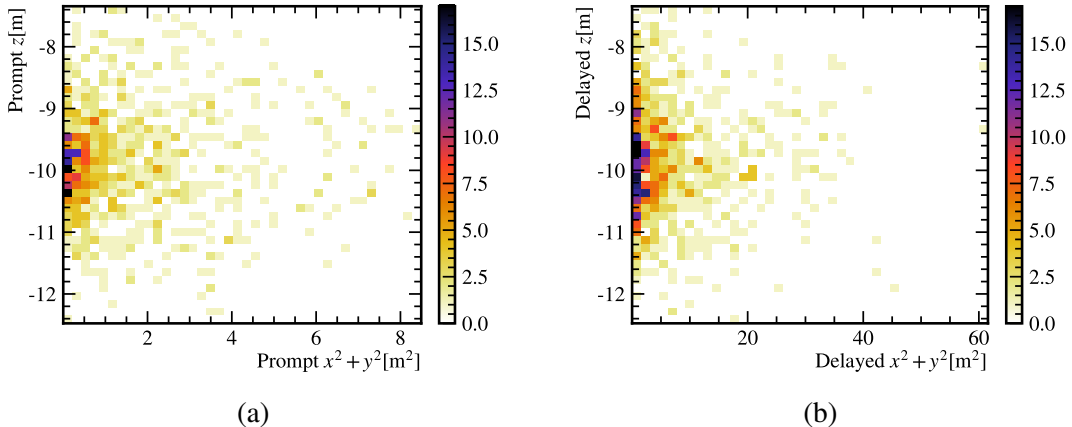


Figure 5.12 The position distribution of prompt and delayed signals. (a) is the position distribution of prompt signals, and (b) is the position distribution of delayed signals.

### 5.1.3 The low-energy threshold in water phase

Through a detailed analysis of calibration source data, distinct Gamma signals at 6.1 MeV and 4.4 MeV are identified, in addition to the characteristic 2.2 MeV Gamma

signal originating from neutron capture on hydrogen. To obtain a cleaner prompt signal energy spectrum, additional selection criteria are applied beyond the initial cuts. Specifically, prompt events are required to satisfy  $\delta A < -50$ , and, for the AmC source, the condition  $n_{10} - n_b > 20$  is imposed. These requirements enhance the purity of the prompt signal spectrum. The energy spectrum of the 4.4 MeV Gamma is shown in Fig. 5.13(a), while that of the 6.1 MeV Gamma is shown in Fig. 5.13(b). Furthermore, the energy cut used in the coincidence analysis is removed. Coincidences occurring within 1000 us are designated as signal, while those in the 1000–2000 us window are taken as background. Using this approach, the energy distribution of the 2.2 MeV Gamma from neutron capture on hydrogen is obtained, as shown in Fig. 5.13(c).

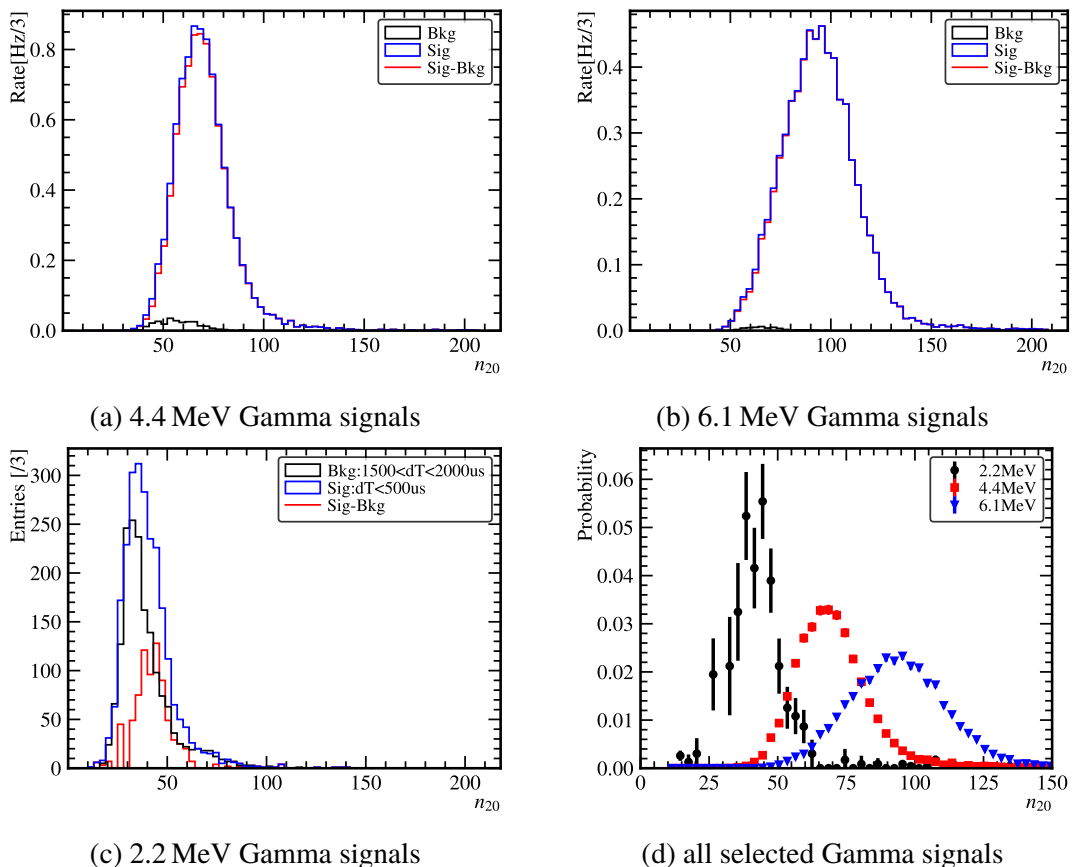


Figure 5.13 The  $n_{20}$  distributions for 2.2 MeV, 4.4 MeV, and 6.1 MeV Gamma signals, as well as the combined spectrum of all selected Gamma events.

After obtaining the energy spectra of the three characteristic signals, we perform Gaussian fitting to quantify their spectral parameters, as shown in Fig. 5.14. When we use  $n_{20}$  to estimate the energy, the light yield is  $14.0 \pm 0.1$  PE/MeV. Simultaneously, we estimate that each triggered physical event contains an average of 8.1 PE originating from PMT dark noise and so on.

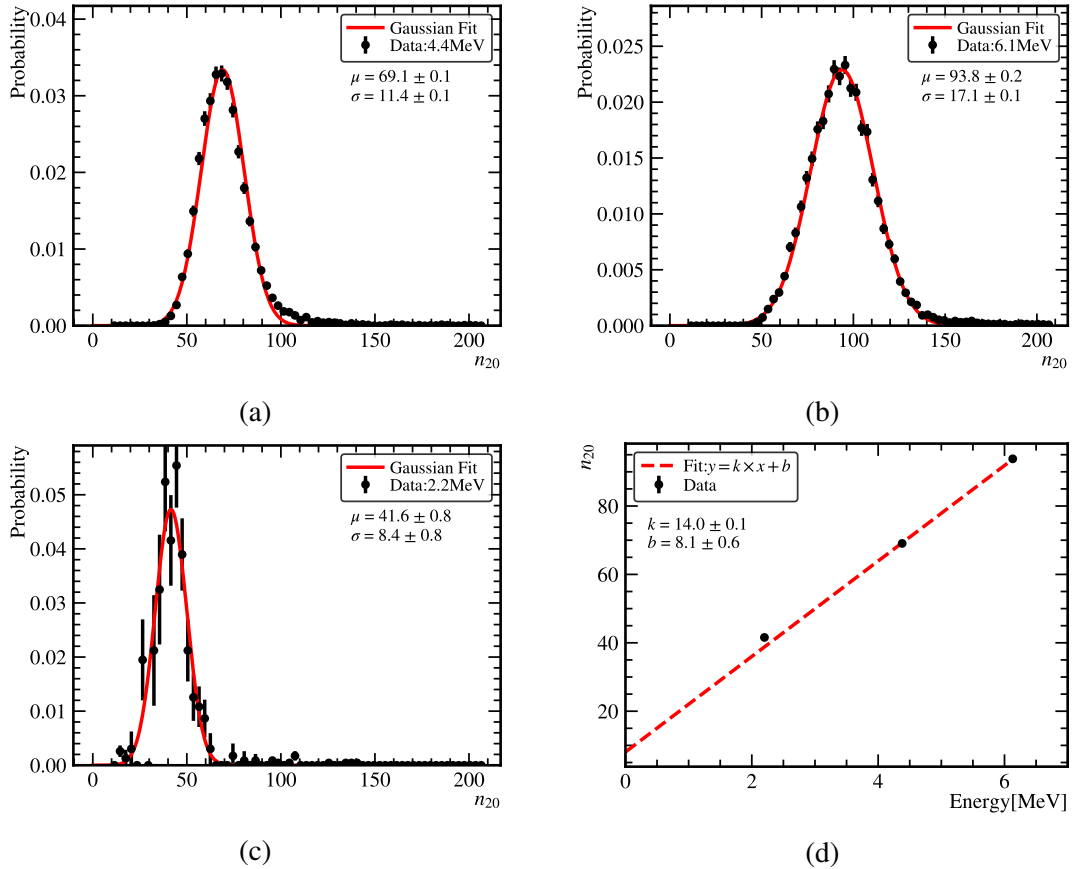


Figure 5.14 Gaussian fit of the  $n_{20}$  distribution of 4.4, 6.1 and 2.2 MeV Gamma signals. (d) is the Cherenkov light yield fit.

## 5.2 The neutron capture detecting ability of JUNO in water phase

Neutron detection efficiency and SNR are critical parameters in the design and optimization of neutron detection systems, as it directly determines the accuracy and sensitivity of experimental measurements. In this section, we will discuss the neutron detection efficiency and SNR of the JUNO detector in the water. In Sec. 5.1.2.2, the delayed signals were successfully reconstructed, and the neutron capture on hydrogen lifetime was obtained. However, the efficiency of n-H capture tagging has yet to be determined. To evaluate this, the prompt candidates are analyzed to calculate the n-H capture tagging efficiency. After prompt signal reconstruction and selection, a total of  $N_p$  prompt candidates are obtained, and the corresponding background contribution,  $N_{pb}$ , is estimated from dedicated background runs. Among these prompt candidates,  $N_0$  delayed candidates satisfy the n-H capture selection criteria. Following a lifetime fit in which the coincidence time is binned into  $N_b$  intervals, as illustrated in Fig. 5.11, the number of accidental coincidence pairs is estimated as  $c \times N_b$ . Thus, the net number of n-H capture events is calculated as  $N_{nH} = N_0 - c \times N_b$ . The tagging efficiency ( $\eta$ ) and the signal-to-noise ratio (SNR) are

defined in Eq. (5.3).

$$\eta = (N_0 - c \cdot N_b) / (N_p - N_{pb}) \quad (5.3)$$

$$\text{SNR} = (N_0 - c \cdot N_b) / \sqrt{c \cdot N_b}$$

As discussed in Sec. 4.1, the application of background suppression techniques inevitably leads to a partial loss of delayed neutron capture events. To evaluate the detector performance, a comprehensive parameter scan was conducted over an extended operational parameter space. This systematic study aims to determine both the maximum attainable neutron detection efficiency and SNR for neutron tagging. The parameters scanned for neutron tagging are summarized in Table 5.2. Following event selection, an n-H capture lifetime fit is performed. The fitted lifetime is required to satisfy the following criteria:

- Fitted lifetime falls within the range of 185–230 us. For calibration runs at  $z = -16$  m: 3293 and 3342, the neutron capture lifetime constraint has been relaxed to the range of 170–250 us, while at  $z = 16$  m: 3279 and 3333, the constraint remains at 180–230 us, as evidenced in Fig. 5.15.
- Contain the reference value of 207 us within its  $1\sigma$  uncertainty interval.

Table 5.2 Neutron Tagging Optimization Parameter Scan Specifications

Parameters	Range	Step or Point
Coincident distance ( $d R, m$ )	3–12	1
Energy related ( $n_{20}$ )	0–49	2 when $9 < n_{20} < 25$ ; 1 when $25 < n_{20} < 50$
AIC criteria ( $\delta A$ )	-70–0	5
LE criteria ( $LE$ )	36–200	200, 150, 100, 50, 45, 43, 42, 41, 40, 39, 38 ,36
Goodness ( $G_{vd}$ )	-0.1–0.15	0.02 when $G_{vd} < 0$ ; 0.01 when $G_{vd} > 0$

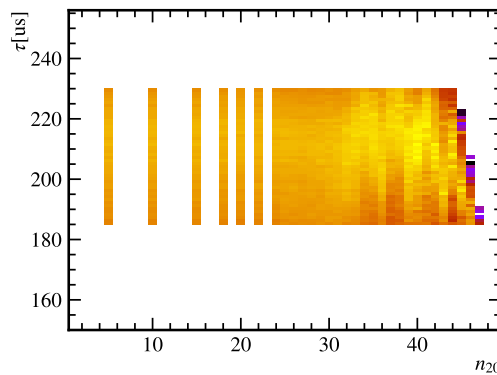


Figure 5.15 The fitted lifetime of Run 3671.

Simultaneously, we examine the  $\chi^2/ndf$  values of all fits, which consistently fall near

1.0, indicating excellent fit quality across the analyses, as shown in Fig. 5.16.

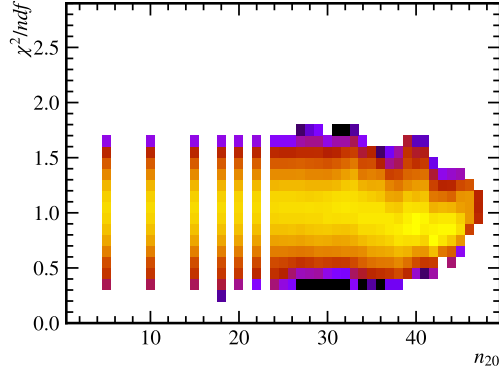


Figure 5.16  $\chi^2/ndf$  values changes with the  $n_{20}$ , but still around 1.0.

### 5.2.1 The maximum neutron detection efficiency

Maximizing neutron detection efficiency is crucial for capturing the largest possible fraction of neutron capture events, thereby improving statistical precision and extending the sensitivity of the detector to rare processes. In this context, the parameter scan results are examined to identify the configuration yielding the highest efficiency within the allowed lifetime selection criteria. As illustrated in Fig. 5.17, the maximum neutron detection efficiency achieved is 10 % in Run 3671, with the corresponding selection parameters as shown in Table 5.3.

Table 5.3 The parameters when get the highest efficiency

Parameters	Selection
Coincident distance ( $d R, m$ )	< 11 m
Energy related ( $n_{20}$ )	> 27
AIC criteria ( $\delta A$ )	< -5
LE criteria ( $LE$ )	< 200
Goodness ( $G_{vd}$ )	> 0.02

As shown in Fig. 5.18, we select the highest-efficiency events in Run 3671. The position distributions of the prompt and delayed signals are presented in Figs. 5.18(a) and 5.18(b), respectively. The prompt-signal distribution is consistent with the position of the deployed calibration source, while the delayed signals are observed to cluster around the corresponding prompt vertices. This position correlation indicates that the delayed signals originate predominantly from neutron captures on hydrogen, as expected. As illustrated in Fig. 5.19, the fitted neutron-capture lifetime is measured to be  $207.2 \pm 47.2$  us,

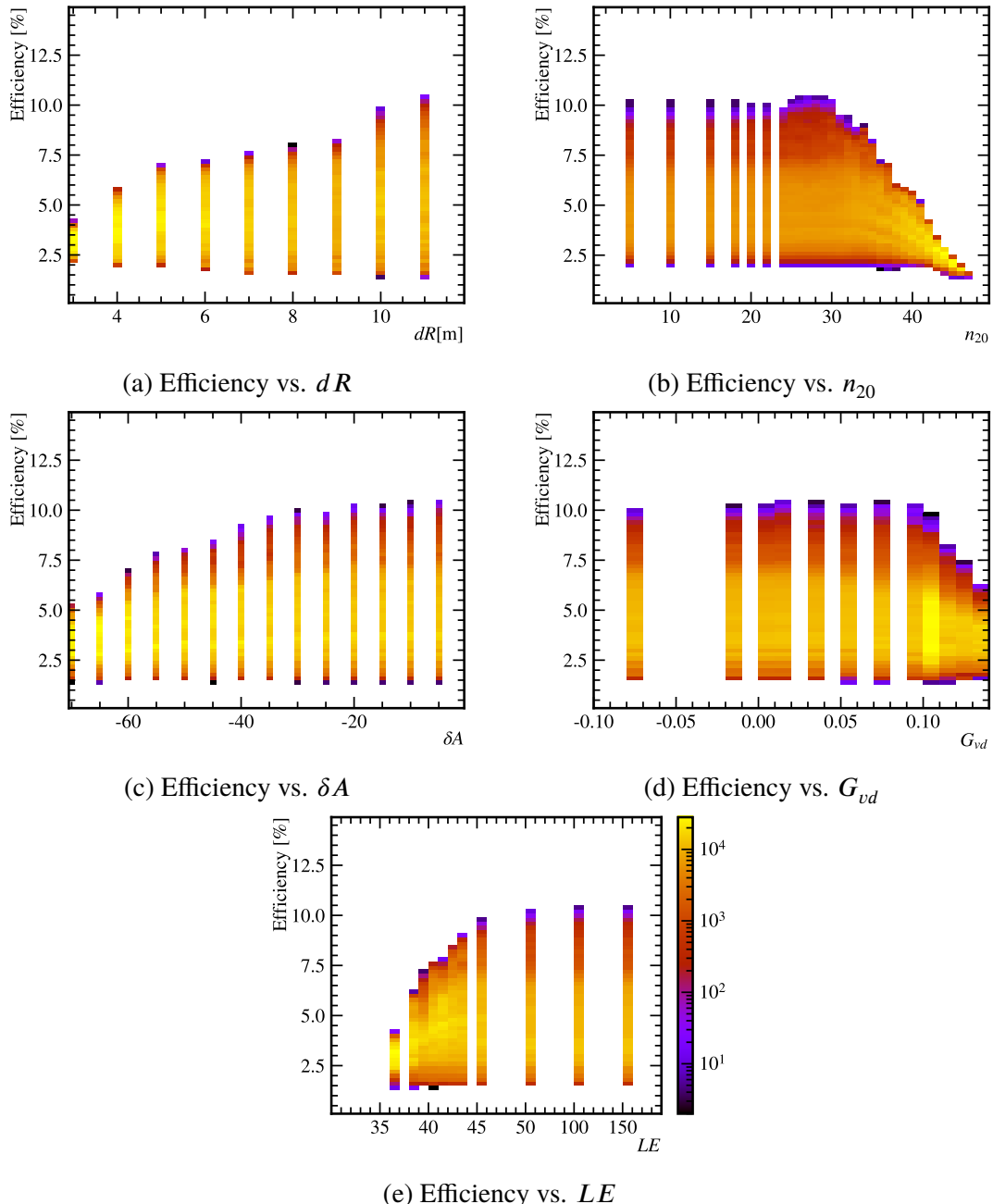


Figure 5.17 Neutron detection efficiency as a function of five key selection parameters in Run 3671. The maximum efficiency achieved is 11.7 %.

in agreement with the theoretical expectation. The resulting fit yields a  $\chi^2/\text{ndf}$  of 27.3/30, demonstrating good fit quality.

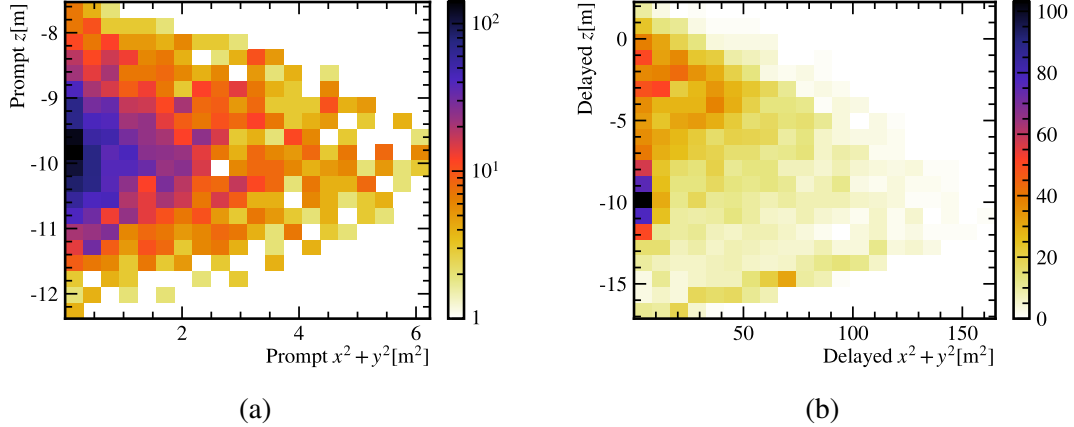


Figure 5.18 The position distribution when getting the highest efficiency in Run 3671. (a) is the position distribution of the prompt signals, and (b) is of the delayed signals.

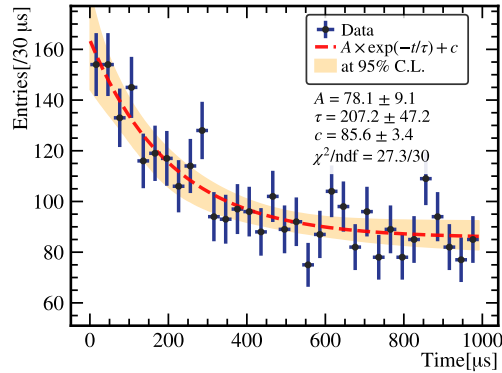


Figure 5.19 The lifetime fit when getting the highest efficiency events in Run 3671.

As illustrated in Fig. 5.20, neutron detection efficiency exceeding 10 % has been experimentally achieved, as validated through comprehensive calibration campaigns with AmBe and AmC neutron sources. During the calibrations on February 2-nd, the higher MM-trigger threshold resulted in an overall lower neutron detection efficiency compared to results of calibrations on February 2-nd. Simultaneously, significant asymmetry is observed between the positive and negative z-axis regions: detection efficiency in the negative z-axis is notably lower than in the positive z-axis, with the most pronounced deficit occurring at the 16 m position. This demonstrates clear non-uniformity in JUNO's detector performance during the water phase.

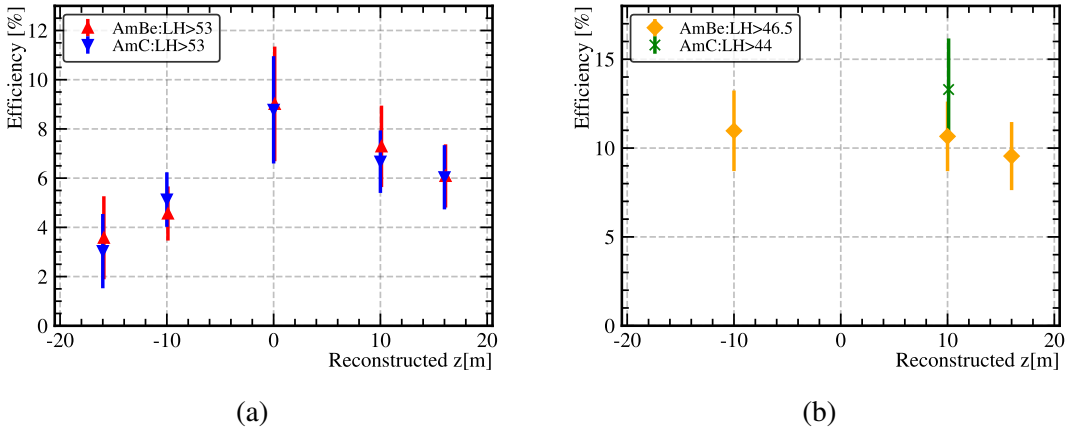


Figure 5.20 The final highest neutron detection efficiency in all 14 calibration runs. (a) is the result of calibrations on February 2-nd, and (b) is of calibrations on February 7-th.

### 5.2.2 The highest neutron detection signal-to-noise ratio

Maximizing SNR is essential for enhancing the clarity of true signal events relative to background fluctuations, thereby improving measurement accuracy and extending the detector's capability to resolve subtle physical effects. In this context, the parameter scan results are analyzed to identify the configuration yielding the highest SNR within the defined event selection criteria. As illustrated in Fig. 5.21, the maximum SNR achieved is over 40 in Run 3671, with the corresponding selection parameters summarized in Table 5.4.

**Table 5.4 The parameters when get highest SNR**

Parameters	Selection
Coincident distance ( $dR, m$ )	< 5 m
Energy related ( $n_{20}$ )	> 35
AIC criteria ( $\delta A$ )	< -10
LE criteria ( $LE$ )	< 39
Goodness ( $G_{vd}$ )	> 0.12

Similarly, as shown in Fig. 5.22 and 5.23, when operating at maximum SNR, the distributions of prompt and delayed signals remain consistent with expectations, and neutron capture lifetime fitting demonstrates excellent agreement with reference values.

As shown in Fig. 5.24, all 14 calibration runs demonstrate robust SNR performance. However, the calibrations on February 7-th exhibit significantly smaller statistical uncertainties due to higher neutron detection efficiency, resulting in substantially greater data volume for analysis.

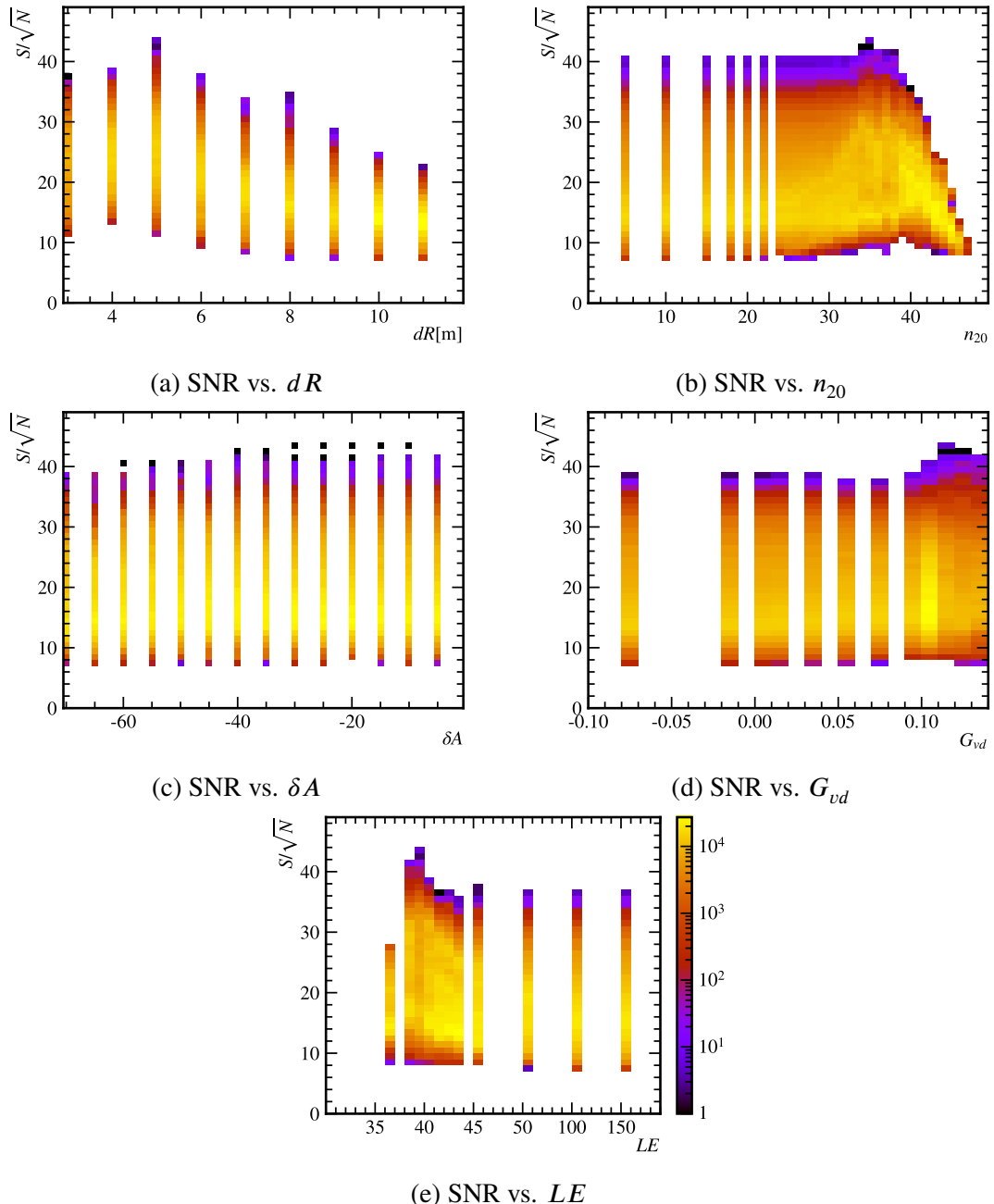


Figure 5.21 Neutron detection SNR as a function of five key selection parameters in Run 3671. The maximum SNR achieved is over 40.

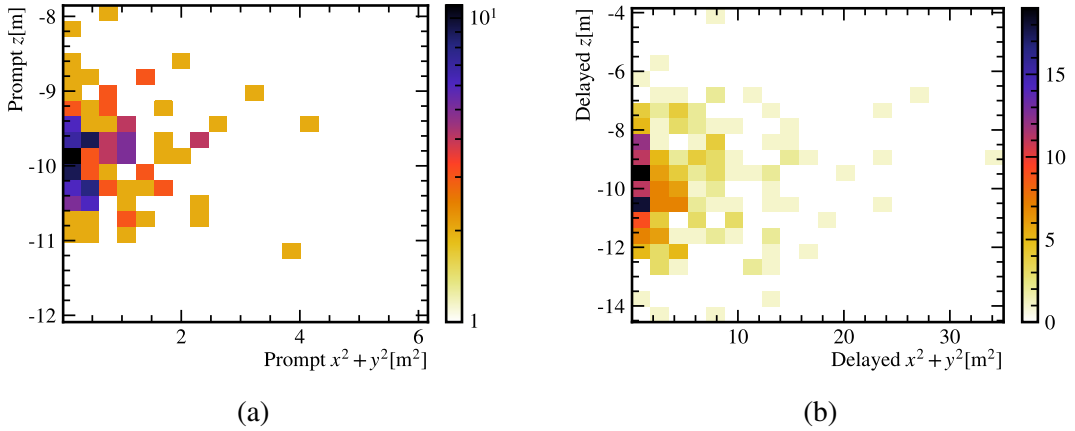


Figure 5.22 The position distribution when getting the highest SNR in Run 3671. (a) is the position distribution of the prompt signals, and (b) is of the delayed signals.

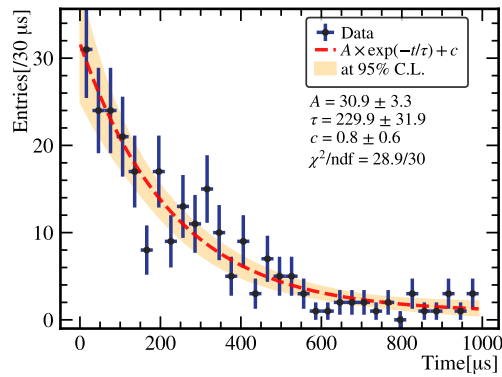


Figure 5.23 The lifetime fit when getting the highest SNR in Run 3671.

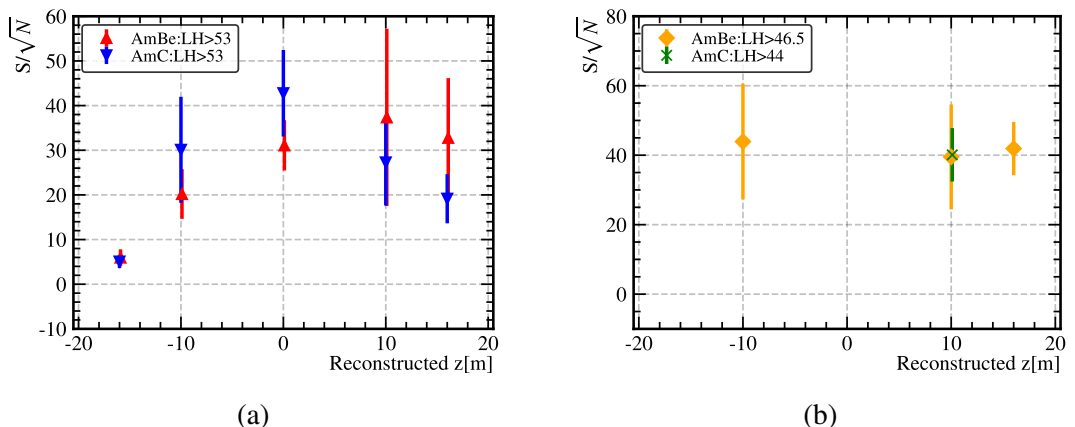


Figure 5.24 The final highest neutron detection SNR in all 14 calibration runs. (a) is the result of calibrations on February 2-nd, and (b) is of calibrations on February 7-th.

### 5.2.3 The balance between neutron detection efficiency and SNR

Based on these results, we observe the relationship between SNR and neutron detection efficiency, as shown in Fig. 5.25. The maximum achievable efficiency exceeds 10 %, while the SNR is lower than 20. This demonstrates a fundamental trade-off: stringent selection criteria yield excellent SNR at the cost of reduced efficiency, whereas relaxed cuts achieve high neutron detection efficiency but introduce significant background contamination.

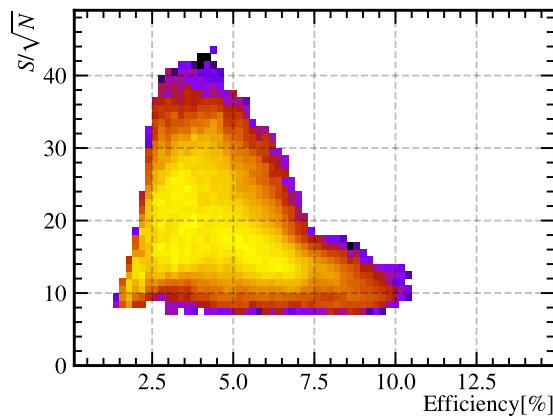


Figure 5.25 The relationship between SNR and neutron detection efficiency. The maximum efficiency exceeds 10 %, and the maximum SNR surpasses 40.

# CHAPTER 6 THE MEASUREMENT OF SPALLATION NEUTRON YIELD IN WATER PHASE

From Sec. 5.1, we have demonstrated JUNO’s neutron detection capability during its water phase. In the absence of calibration sources, this capability enables the detection of spallation neutrons produced by cosmic-ray muons traversing the detector. Because of the MM trigger threshold, we just use Run 3639 (around 2 h) and 3677 (around 5 h) for this measurement.

## 6.1 The reconstruction of muon track

Our muon reconstruction comes from Machine Learning (JUNO-doc-13818), based on Global trigger data, around 7 h. To better characterize muon properties, we define the following parameters, as shown in Fig. 6.1.

- $D_{tc}$ : Distance from the CD center to the muon track
- $L_t$ : Track length  $L_t = 2 \times \sqrt{R_{CD}^2 - D_{tc}^2}$ ,  $R_{CD} = 17.7$  m
- Distance from events to muon track:  $dR$

From the distribution of  $D_{tc}^2$  as shown in Fig. 6.2(a), we observe cosmic-ray muons uniformly traversing the Central Detector. The Total PE distribution reveals that the majority of muons deposit between  $10^5$  and  $10^6$  PE, while a small fraction exhibit total PE counts below  $10^5$ , as evidenced in Fig. 6.2(b). Fig. 6.2(c) demonstrates a strong correlation between muon track length and total PE for primary muons, forming a concentrated distribution band. However, events with  $< 10^5$  PE despite long reconstructed tracks likely originate from PMT flasher artifacts or electronic noise mimicking muon signals. Therefore, we implement a selection cut requiring muon candidates to have total PE  $> 10^5$ . After the cut of  $D_{tc} < 17.7$  m and Total PE  $> 10^5$ , the muon event rate is 4.03 Hz, which is consistent with the result of simulation ( $0.004$  Hz/m<sup>2</sup>)<sup>[59]</sup>. Also, the average energy of muon is 207 GeV.

## 6.2 The search for spallation neutron

Similar to Sec. 5.1.2.1, we also use coincident reconstruction for spallation neutron, as shown in Fig. 6.3. For accidental coincident backgrounds, we reconstruct all events

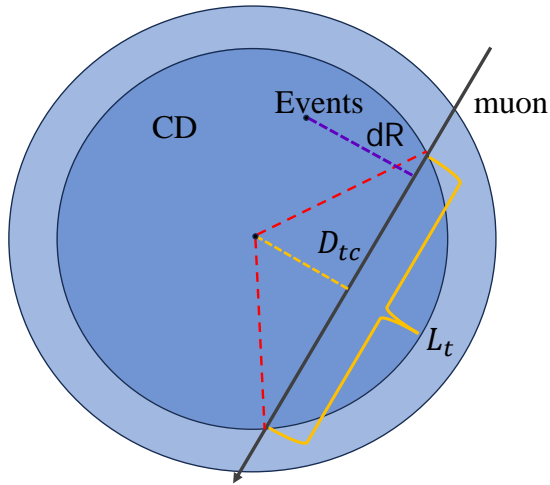


Figure 6.1 The definition of parameters used in spallation neutron search.

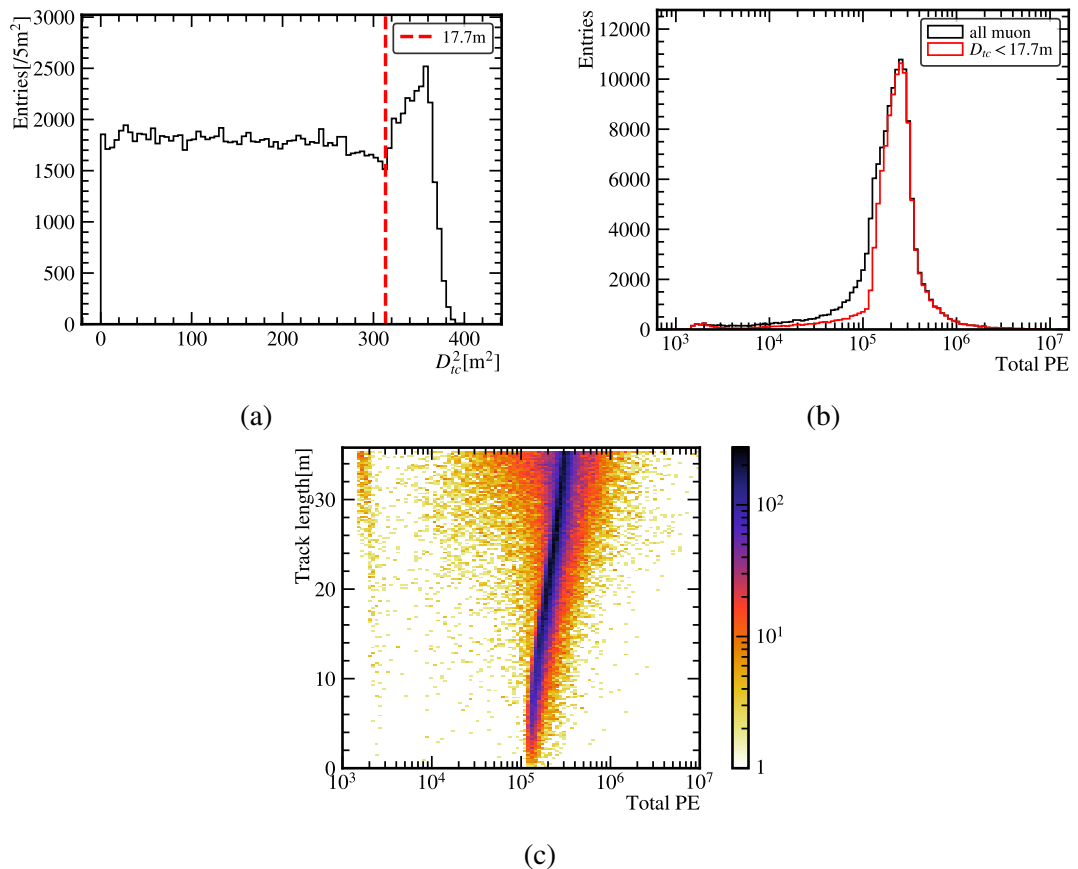


Figure 6.2 (a) shows the distribution of  $D_{tc}^2$ , (b) evidences the total PE of muons and (c) demonstrates the relationship between total PE and the track length of muons.

in 20–2000 us after muons. In 0–20 us, events are influenced by baseline, after-pulse and Michel electrons, and would not be included in our study.

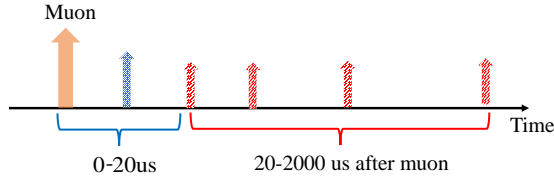


Figure 6.3 The coincident reconstruction of spallation neutrons

Validated through AmBe and AmC calibration, we get some basic cut for spallation neutrons:

- Fiducial volume:  $r < 16 \text{ m}$
- Background cut:  $\delta A < -60, LE < 50, G_{vd} > 0.1$
- Energy related:  $n_{20} < 70$

After applying basical cuts, we observe residual downward events clustered near the detector center, as illustrated in Fig. 6.4. To suppress this unknown background component, we implement an additional directional cut based on reconstructed direcition  $p_z/p > -0.75$ .

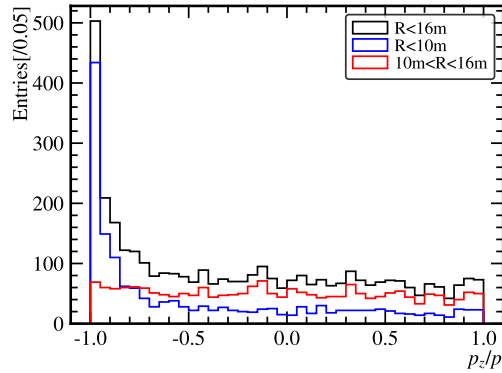


Figure 6.4 The distribution of  $p_z/p$  in different regions

For the coincident distance and energy cut, we choose the events in 50–650 us as signals and in 1400–2000 us as background. After background subtraction, the distribution of  $dR$  reveals significant event clustering within 6 m, as evidenced in Fig. 6.5. This observation justifies implementing a position correlation cut of  $dR < 6 \text{ m}$  to isolate true spallation neutron capture events. Similarly, in the  $n_{20}$  distribution after background subtraction as shown in Fig. 6.6, we observe a prominent peak around 35 PE. Using Gaussian fitting, the measured peak position is 36.3 PE. This contrasts with the expected value of 41 PE from that in calibration sources and the light-yield curve estimation of 38.9 PE. The

primary reason for this discrepancy lies in the calibration sources measuring light yield at fixed positions, whereas the current result represents the average PE expectation within 16 m across the detector. Despite the numerical difference, these results remain consistent within the context of detector-scale estimation. Finally, we decide to use a cut of energy:  $30 < n_{20} < 70$ .

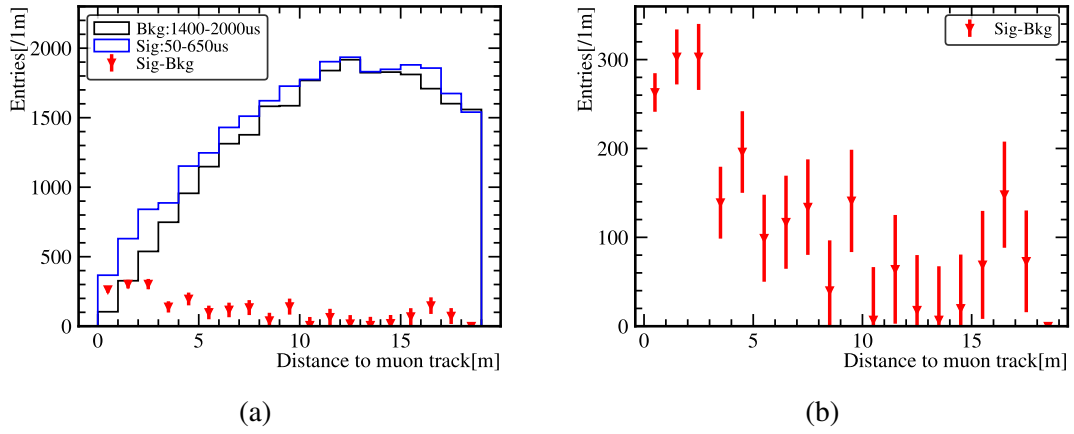


Figure 6.5 The coincident distance distribution.

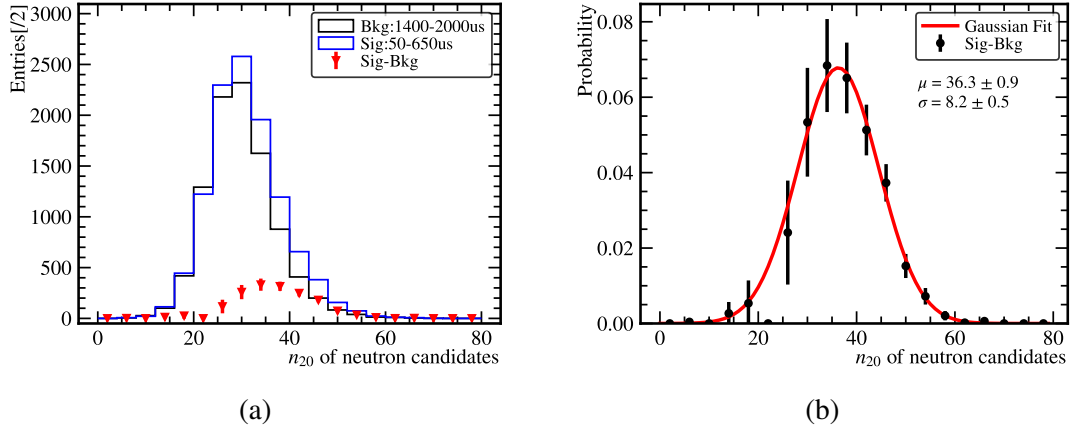


Figure 6.6 The distribution of energy related parameter  $n_{20}$

At this stage, we calculate the number of spallation neutrons using capture lifetime fitting in [30, 930 us], as shown in Fig. 6.7. From the fit result,  $987 \pm 119$  spallation neutron events are selected. We similarly examine the position distribution of selected events. By using coincidences within the 1100–2000 us window as background and subtracting them. In both background and selected events, we observe event clustering at the detector center. After background subtraction, we obtain the position distribution of spallation neutrons. The position distribution in the upper hemisphere of the detector exceeds that in the lower hemisphere. This asymmetry aligns with the detector non-uniformity observed during calibration source studies.

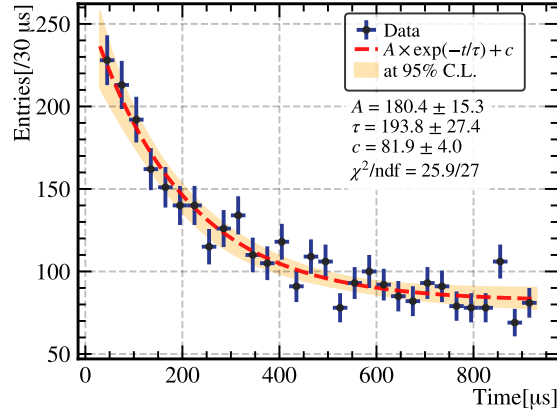


Figure 6.7 The lifetime fitting of spallation neutron.

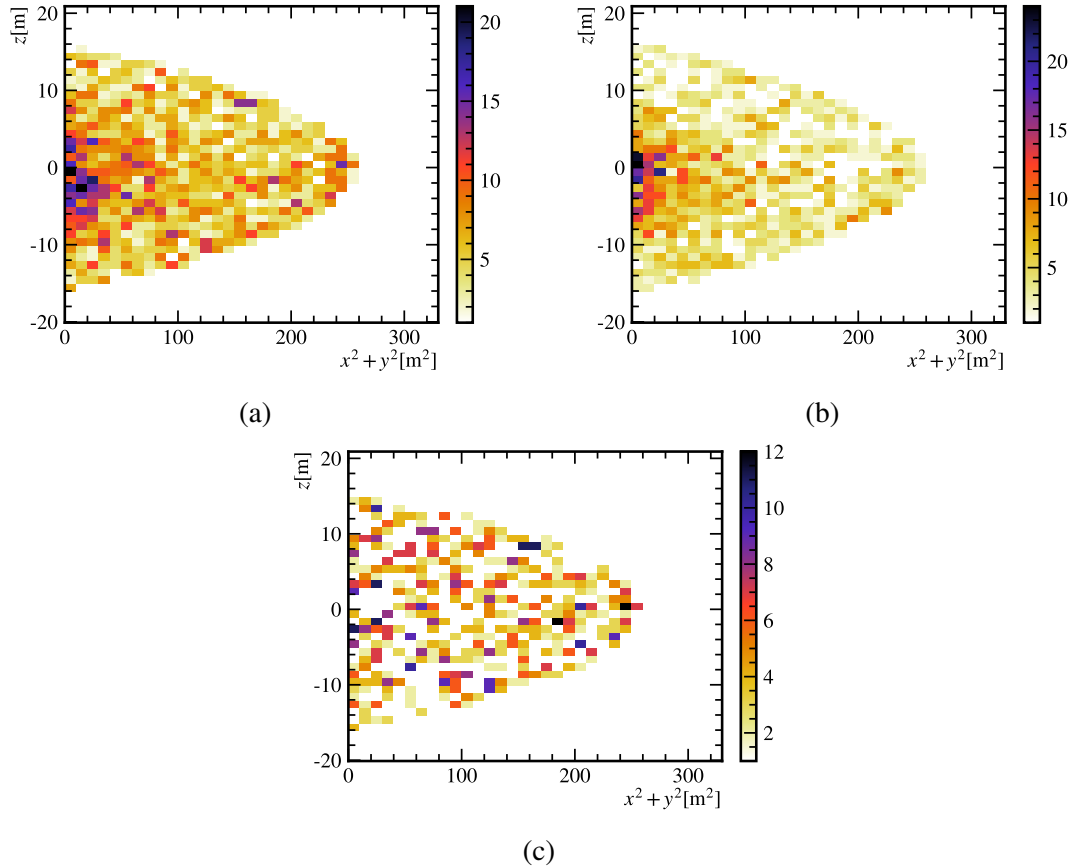


Figure 6.8 The position distribution. (a) evidences the distribution of the selected events. (a) shows the distribution of the background events in 1100–2000  $\mu$ s after muon. (c) displays the result of histogram subtraction between two distributions

### 6.3 The spallation neutron yield calculation

By combining data from the previous 14 calibration runs, we can estimate the average neutron detection efficiency within a 16-meter radius of the detector. We employed an  $R^3$ -weighted position averaging method to compute the position-dependent neutron detection efficiency, yielding a volume-averaged efficiency of  $3.3 \pm 0.4\%$ , and the final efficiencies in our study are in Table. 6.1. The spallation neutron yield  $Y_n$  is defined as the neutron production rate per unit muon track length and per unit density, as defined in Eq. (6.1).

$$Y_n = \frac{N_n}{\rho N_{\text{muon}} L_{t,\text{ave}}} = \frac{N_n}{\rho \Sigma_{\text{muon}} L_t} \quad (6.1)$$

Only consider the statistical uncertainty, the spallation neutron yield is  $Y_n = (2.31 \pm 0.41(\text{stat.})) \times 10^{-4} \mu^{-1} \text{g}^{-1} \text{cm}^2$ .

Table 6.1 The efficiencies in spallation neutron search

	Efficiency
Neutron Tag	$3.3 \pm 0.4\%$
Fiducial volume	73.9 %
Coincident time window	85.4 %
Direction cut	87.5 %

Simultaneously, there are three primary sources of systematic uncertainty. The first kind comes from the muon track reconstruction. We found a systematic 0.2 % bias between reconstructed muon track lengths and their true values, as shown in Fig. 6.9. Consequently, we attribute a 0.2 % systematic uncertainty to muon track reconstruction in our analyses. The second source of systematic uncertainty originates from neutron count variations induced by coincident distance selection. We perform parameter scans across multiple coincidence distances, as evidenced in Fig. 6.10 and quantified the systematic uncertainty using the maximum deviation from the central value obtained at different coincident distances. The final source of systematic uncertainty stems from detector inhomogeneity and discrepancies between simulation and experimental data. During AmBe and AmC calibrations, the neutron detection efficiency at  $z = -16 \text{ m}$  approaches zero, as shown in Fig. 6.11(a). To quantify the impact of this local efficiency anomaly on the global average efficiency, we perform a parameter scan across a  $5\sigma$  range of efficiency uncertainty (0 to 1.2 %) based on the fitting results at this position. The range in the resulting detection efficiency is then adopted as the systematic uncertainty, as shown in Fig. 6.11(b).

All the systematic efficiencies are summarized in Table 6.2. Our final result of spallation neutron yield measurement is  $Y_n = (2.31 \pm 0.22(\text{sys.}) \pm 0.41(\text{stat.})) \times 10^{-4} \mu^{-1} \text{g}^{-1} \text{cm}^2$ . As shown in Fig. 6.12, our measurements in the water phase demonstrate statistically significant consistency with Super-Kamiokande's benchmark results across key neutron detection parameters, validating the calibration methodology and detector performance.

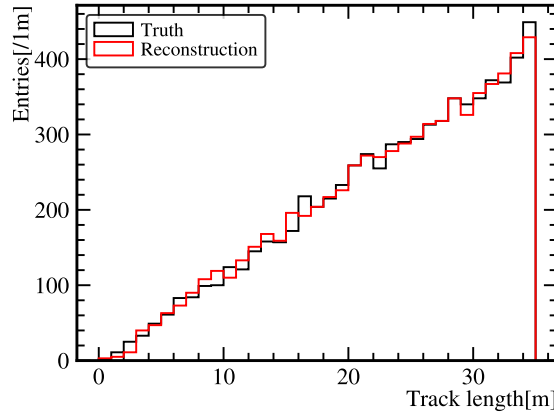


Figure 6.9 The track length distribution of reconstructed muon and their truth.

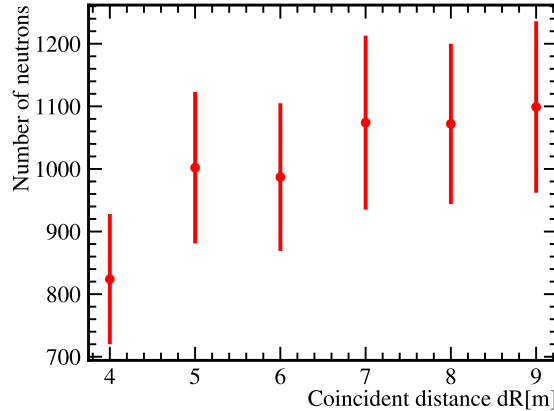


Figure 6.10 We scan  $dR$  from in 3–9 m, and calculate the number of neutrons.

Table 6.2 The systematic uncertainty in spallation neutron search

	uncertainty
Muon track reconstruction	0.2 %
Number of spallation neutrons	$\pm 92$
The detection efficiency	$\pm 0.3 \%$

### 6.3.1 Cross check using water-pool reconstructed muon

In order to cross-check the muon reconstruction in the water phase, we repeat the analysis using the water pool muon reconstruction method (JUNO-doc-13604). Except

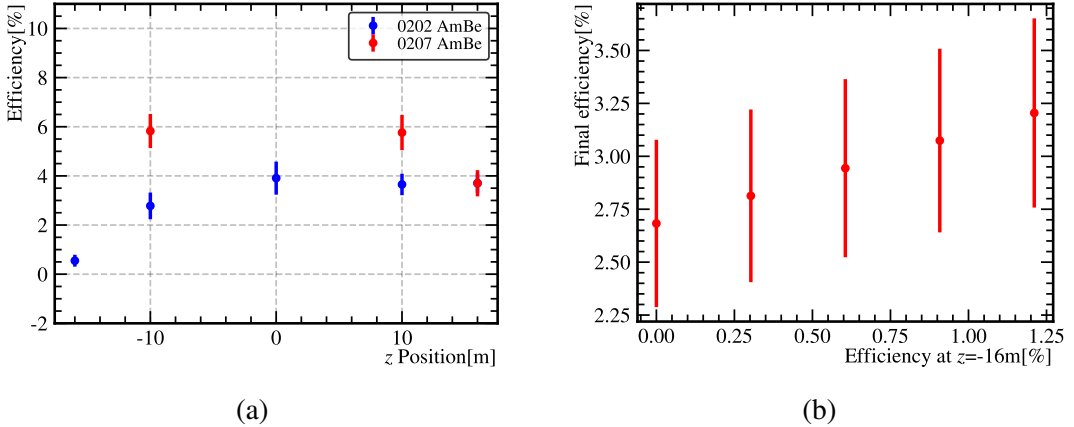


Figure 6.11 The estimation of uncertainty from efficiency. (a) evidences the efficiency estimated from AmBe calibration with the same selection of spallation neutron. (b) shows that the final efficiency is influenced by the efficiency at  $z = -16\text{ m}$ .

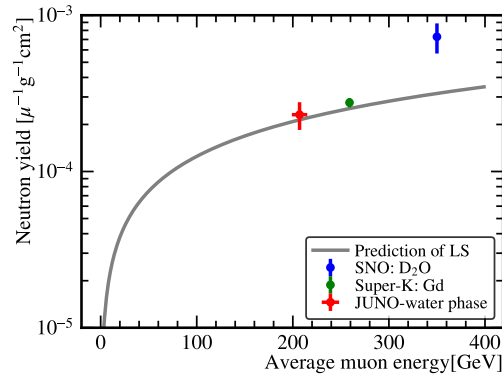


Figure 6.12 The final yield measurement. The result of SK comes from<sup>[60]</sup>, of SNO comes from<sup>[61]</sup> and the prediction of LS is from<sup>[62]</sup>.

for the removal of the muon selection cut, all other selection criteria remain identical to those applied when using CD muons. The final result is  $Y_n = (2.32 \pm 0.19(\text{sys.}) \pm 0.44(\text{stat.})) \times 10^{-4} \mu^{-1}\text{g}^{-1}\text{cm}^2$ , as shown in Fig. 6.13 and 6.13(c). Those two results are consistent with each other.

### 6.3.2 The prediction of $Y_n$ in water

At present, regarding the research on the muon-induced spallation neutron yield, multiple underground experiments have completed the measurements. Among them, most experiments measured the yield in LS. SK<sup>[60]</sup> was the first to complete the measurement of the yield in the water phase, and SNO<sup>[61]</sup> experiment completed the measurement of the yield in heavy water. The relevant results are summarized in Tab. 6.3.

In LS, the yield of spallation neutrons is positively correlated with the average energy of muons and can be described by an empirical formula, as shown in Eq. (6.2)<sup>[62,64,70-71]</sup>.

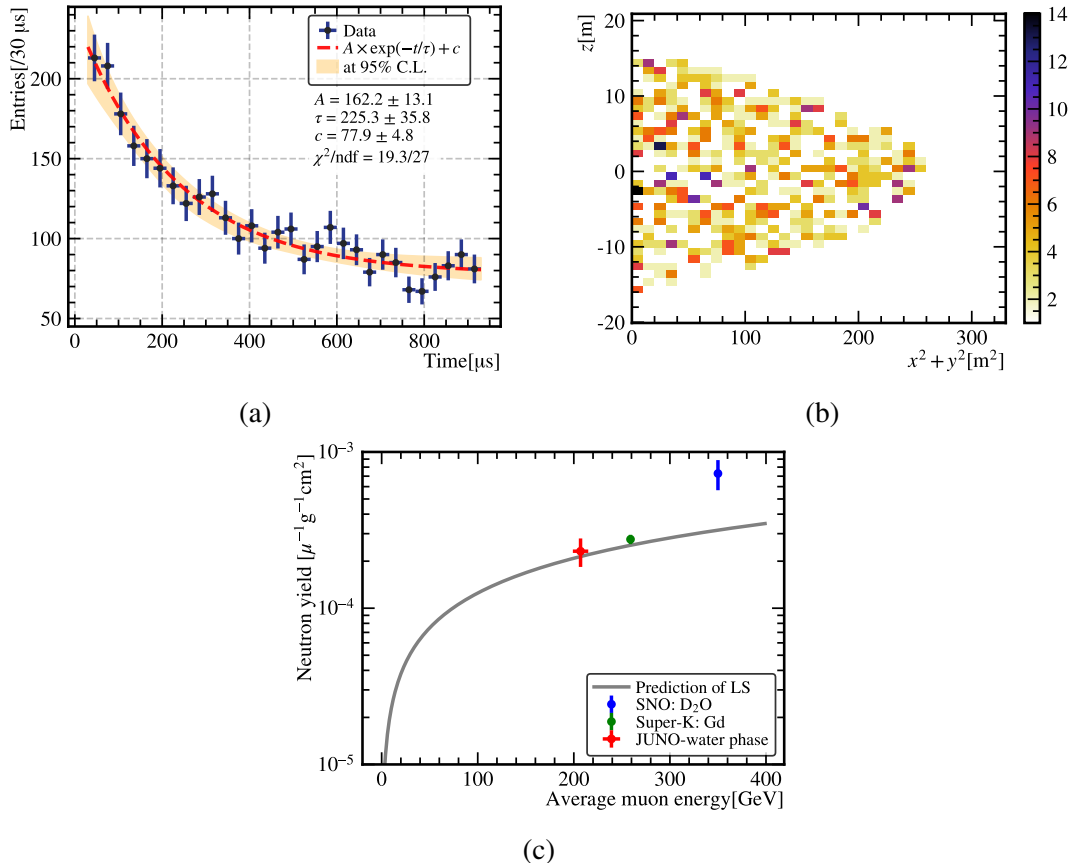


Figure 6.13 (a) is the lifetime fitting of spallation neutrons using WP muons. (b) is the position distribution after extracting background. (c) is the yield of spallation neutron using WP muons.

Table 6.3 The measurement of spallation neutron yield

Target	Experiment	$E_\mu$ (GeV)	$Y_n$ ( $\mu^{-1} \text{g}^{-1} \text{cm}^2$ )
LS	Hertenberger <sup>[63]</sup>	13	$(2.0 \pm 0.7) \times 10^{-5}$
LS	Boehm <sup>[64]</sup>	16.5	$(3.6 \pm 0.4) \times 10^{-5}$
LS	DayaBayEH2 <sup>[65]</sup>	$64.7 \pm 3.9$	$(10.22 \pm 0.87) \times 10^{-5}$
LS	Aberdeen <sup>[66]</sup>	$89.8 \pm 2.9$	$(1.19 \pm 0.29) \times 10^{-4}$
LS	DayaBayEH3 <sup>[65]</sup>	$143.0 \pm 8.6$	$(1.703 \pm 0.122) \times 10^{-4}$
LS	KamLAND <sup>[67]</sup>	$268 \pm 8$	$(2.8 \pm 0.3) \times 10^{-4}$
LS	Borexino <sup>[68]</sup>	280	$(3.10 \pm 0.11) \times 10^{-4}$
LS	JNE <sup>[69]</sup>	$\sim 360$	$(3.37 \pm 1.44) \times 10^{-4}$
Water (Gd)	SK <sup>[60]</sup>	$259 \pm 9$	$(2.76 \pm 0.26) \times 10^{-4}$
Water	This work	207	$(2.31 \pm 0.45) \times 10^{-4}$
Hevey Water	SNO <sup>[61]</sup>	$363 \pm 1.2$	$(7.28 \pm 1.59) \times 10^{-4}$

Wang, Y.-F. et al<sup>[62]</sup> and Mei. et al<sup>[71]</sup>, Kudryavtsev. et al<sup>[72]</sup> and Daya Bay<sup>[65]</sup> used some yield measurement to fit and their fit results are in Tab. 6.4.

$$Y_n(E_\mu) = a_\mu E_\mu^{b_\mu} \quad (6.2)$$

Table 6.4 The fitted parameters of Eq. (6.2)

	Fitted $a_\mu (10^{-6} \mu^{-1} g^{-1} cm^2)$	Fitted $b_\mu$
Wang Y.-F. et al	4.14	0.74
Mei. et al	3.824	0.849
Kudryavtsev	3.2	0.79
Daya Bay	4.0	0.77
This work	3.36	0.793

As shown in Fig. 6.14, with the exception that the fitting results of Mei et al. deviate notably from these experiments, the other three fitting results are generally in agreement with the experimental measurements, despite some minor discrepancies. Meanwhile, the three prediction results incorporate the results of the two measurements in water phase. This indicates that the predicted curve of the neutron yield of LS as a function of the average muon energy can approximately characterize the neutron yield of the water phase. Additionally, calculations were performed based on the two measurement results from the water phase of JUNO and SK, and the result is  $a_\mu = 3.36 \times 10^{-6} \mu^{-1} g^{-1} cm^2$ ,  $b_\mu = 0.793$ .

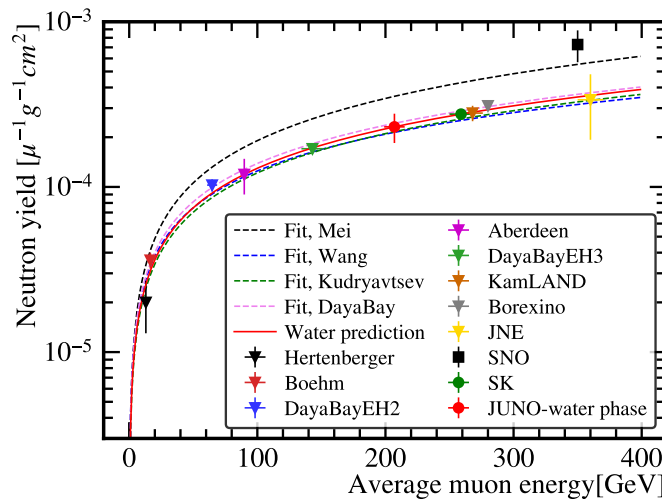


Figure 6.14 The inverted triangle markers denote the measurements outcome in LS, the square markers represent the measurement results in heavy water, and the circular markers indicate the measurement findings in water. The dashed line depicts the yield curve derived from fitting the measurement results in LS, while the red solid line represents the yield prediction curve computed using the measurement results in the water phase.

# CHAPTER 7 THE OBSERVATION OF SOLAR NEUTRINO

## 7.1 Searching for Solar neutrino signals

### 7.1.1 The dataset

In order to search for solar neutrinos, we used the data from the MM trigger. During the data acquisition process in the water phase, the detector and the trigger system were still in the commissioning phase. Consequently, the data acquisition conditions were unstable. As a result, only a limited amount of data was available for the search of solar neutrinos. To address this, we carefully selected datasets with relatively high data acquisition quality and, to the greatest extent possible, performed calibrations both before and after data acquisition. After selection, there were 9 runs in total, and the information of each run is shown in the Tab. 7.1. The total lifetime is 18.13 h and more than 15 h of data were taken at night.

Table 7.1 The runs used for solar neutrinos

Run number	lifetime (h)	Time (date/h)	MM Trigger threshold
3322	1.15	0203/00	threshold=53
3323	0.69	0203/01	threshold=53
3413	2.76	0203/23	threshold=53
3415	0.48	0204/03	threshold=54.5
3416	3.20	0204/03	threshold=54.5
3530	1.43	0205/23	threshold=46.5
3531	1.34	0206/01	threshold=46.5
3639	2.18	0207/17	threshold=47
3677	4.88	0208/01	threshold=44

### 7.1.2 The selection in preliminary reconstruction

Given that likelihood-based reconstruction is time-consuming, we conduct event selection based on preliminary reconstruction. This approach aims to eliminate certain dark noise background events and radioactive background events from the PMT surface. The criteria are in following.

- Fiducial volume  $r < 17 \text{ m}$

- $\text{isglass} < 0.5$
- $\text{score} > 0.001$
- $p_z/p > -0.8$
- $n_{20} > 12$

### 7.1.3 The energy selection

In the water phase, solar neutrinos engage in elastic scattering (ES) with electrons. As a result of this scattering process, the scattered electrons acquire energy and emit Cherenkov light, which is subsequently detected. Based on previous research, the mass of electron neutrinos is found to be less than 0.31 eV at 90 % CL<sup>[73]</sup>. When observing neutrinos within the MeV energy range, the kinetic energy  $E_{k,\nu}$  is significantly greater than mass  $E_\nu$ , i.e.,  $E_{k,\nu} \gg E_\nu$ . During the calculation in ES, the mass of the neutrino itself can be neglected. Under such circumstances, the neutrino can be equivalently treated as Gamma. Consequently, the screening conditions can be derived from the calibration of the Gamma source, enabling us to determine the reasonableness of the remaining events. From Sec. 5.1.3, we can get the relationship between Gamma energy and  $n_{20}$  is  $n_{20} = 14E + 8.1$ . When the energy scale of Gamma is applied to neutrinos, it becomes possible to directly bypass the recoil electrons, directly estimate the corresponding neutrino energy and optimize the selection of neutrino signals. As shown in Fig. 7.1, we have a cut of energy:  $93 < n_{20} < 233$ , corresponding to the neutrino energy range of 6.1 – 16 MeV.

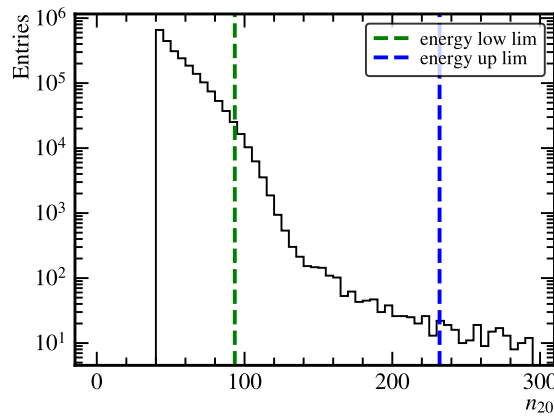


Figure 7.1 The selection of energy of solar neutrinos.

### 7.1.4 The position selection

Following the energy screening, it was observed that a substantial number of events converged at the center of the detector, as shown in Fig. 7.2(a). Analogous to the scenario depicted in Fig. 7.2(b), the events at the center exhibited a downward tendency. Given that the search for solar neutrinos is highly direction-dependent, rather than implementing a direction cut, we chose an additional cylindrical region at the center of the detector for screening, as illustrated in Fig. 7.2(a). Our final FV cut is:

- $x^2 + y^2 > 50 \text{ m}^2$
- $r < 14 \text{ m}$

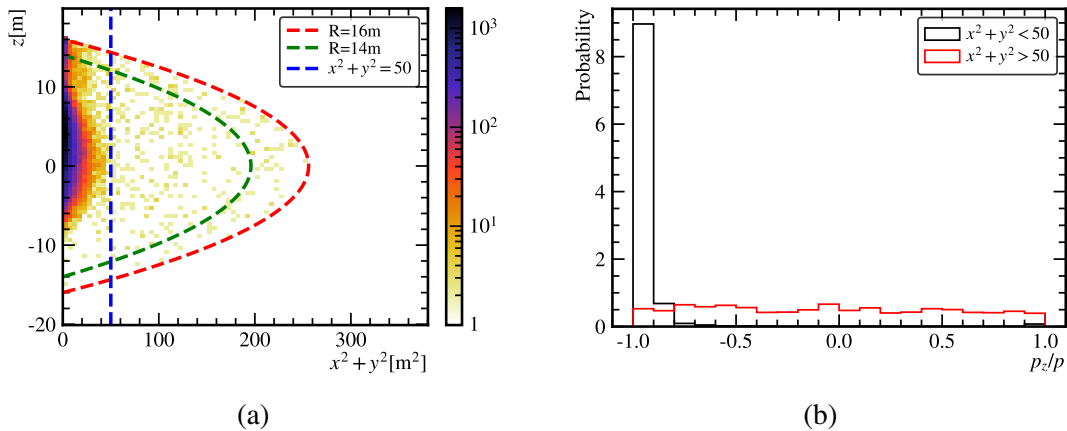


Figure 7.2 The position selection of solar neutrino. (a) shows the final FV selection, while (b) shows direction distribution in different regions.

### 7.1.5 The muon spallation cut

For solar neutrinos, the most significant background comes from the electrons produced by the decay of radioactive isotopes generated by the reaction of cosmic ray muons with oxygen atoms. The main types of backgrounds are shown in Tab. 7.2. Among these, the Gamma or electron signals with energies spanning from 5 to 20 MeV significantly disrupt the solar neutrino signals. Simultaneously, this portion of the signals predominantly originates from the decay of these nuclides. Consequently, it can be approximately estimated that the time lies within the range of 1 to 1000 ms following the muon. Through the simulation of muons, we are able to extract electrons or Gammas with these specific characteristics, as shown in Fig. 7.3. Subsequently, we can analyze their time and position distributions, which in turn aids us in optimizing reasonable cuts. This optimization aims to minimize the impact caused by the spallation background to the greatest extent possible.

Taking into account the resolution of the reconstruction, position cuts were imple-

Table 7.2 The main types of spallation isotopes and the primary processes that produce them<sup>[74]</sup>. We use the measured yield of spallation neutrons to scale the yields of other isotopes based on simulation.

Isotope	Lifetime (s)	Decay mode	Energy (MeV)	$N_{sim}$	Scaled Yield ( $10^{-7} \mu^{-1} g^{-1} cm^2$ )
n	0.0002	n-H	2.2	266910	2310
$^{11}_4 Be$	19.9	$\beta^-$	11.51	47	0.407
		$\beta^- \gamma$	9.41+2.1( $\gamma$ )		
$^{16}_7 N$	10.3	$\beta^-$	10.44	2003	17.334
		$\beta^- \gamma$	4.27+6.13( $\gamma$ )		
$^{15}_6 C$	3.53	$\beta^-$	9.77	294	2.544
		$\beta^- \gamma$	4.51+5.30( $\gamma$ )		
$^8_3 Li$	1.21	$\beta^-$	~13.0	78	0.675
$^8_5 B$	1.11	$\beta^+$	~13.9	23	0.199
$^9_3 Li$	0.26	$\beta^-$	13.6	42	0.363
		$\beta^- + n$	~10		
$^9_6 C$	0.18	$\beta^+ + p$	3-15	6	0.052
$^8_2 He$	0.17	$\beta^- \gamma$	9.67+0.98( $\gamma$ )	4	0.034
		$\beta^- + n$			
$^{12}_4 Be$	0.034	$\beta^-$	11.71	72	0.623
$^{12}_5 B$	0.029	$\beta^-$	13.37	800	6.923
$^{13}_5 B$	0.025	$\beta^-$	13.44	457	3.955
$^{14}_5 B$	0.02	$\beta^- \gamma$	14.55+6.09( $\gamma$ )	277	2.397
$^{12}_7 N$	0.016	$\beta^+$	16.38	250	2.164
$^{13}_8 O$	0.013	$\beta^+ + p$	8-14	167	1.445
$^{11}_3 Li$	0.012	$\beta^-$	20.62	2	0.017
		$\beta^- + n$	~16		

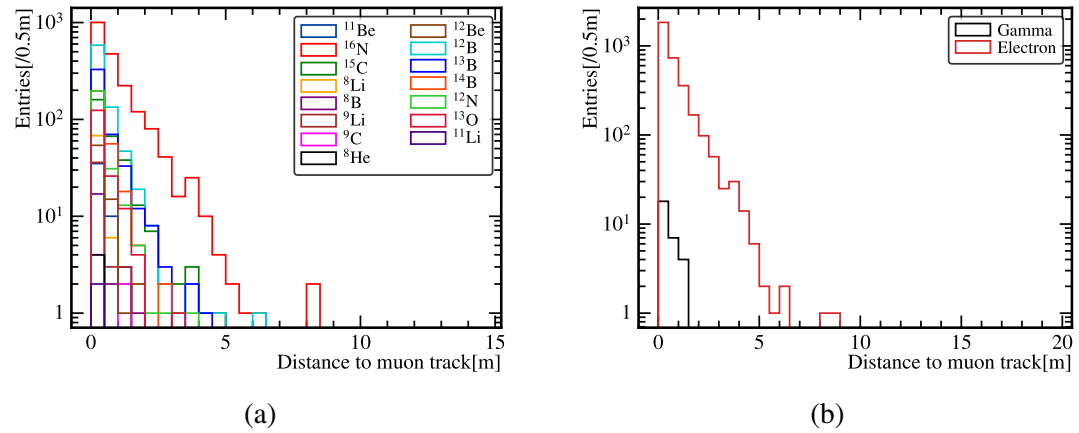


Figure 7.3 The distribution of the distance between spallation isotopes (a), electrons or Gammas (b) and the muon track.

mented on the spallation background, which was then partitioned into two components:

- Time cut: >5 ms after muon
- Position cut: >15 m from muon track if there is a muon before events in 1–1000 ms, as shown in Fig. 7.4.

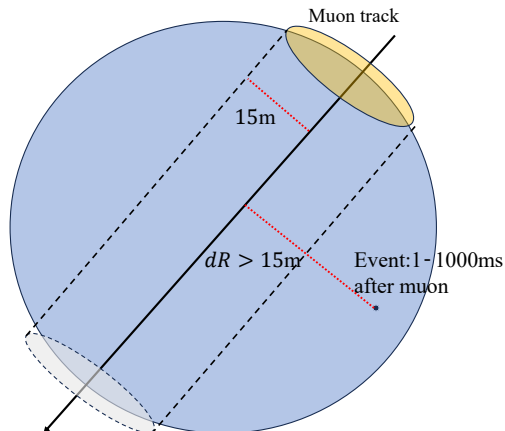


Figure 7.4 The position cut of spallation background.

### 7.1.6 The observation of solar neutrino signals

## REFERENCES

- [1] Breitenberger E. Scintillation spectrometer statistics[J]. Progress in nuclear physics, 1955, 4: 56-94.
- [2] Chen L, et al. Optimization of the electron collection efficiency of a large area MCP-PMT for the JUNO experiment[J/OL]. Nucl. Instrum. Meth. A, 2016, 827: 124-130. <https://www.sciencedirect.com/science/article/pii/S0168900216303308>. DOI: <https://doi.org/10.1016/j.nima.2016.04.100>.
- [3] Bellamy E, et al. Absolute calibration and monitoring of a spectrometric channel using a photomultiplier[J/OL]. Nucl. Instrum. Meth. A, 1994, 339(3): 468-476. <https://www.sciencedirect.com/science/article/pii/016890029490183X>. DOI: [https://doi.org/10.1016/0168-9002\(94\)90183-X](https://doi.org/10.1016/0168-9002(94)90183-X).
- [4] Tao S X, et al. Secondary electron emission materials for transmission dynodes in novel photomultipliers: A review[J]. Materials, 2016, 9(12): 1017.
- [5] Furman M, Pivi M. Probabilistic model for the simulation of secondary electron emission[J]. Physical review special topics-accelerators and beams, 2002, 5(12): 124404.
- [6] Bruining H, De Boer J. Secondary electron emission: Part I. Secondary electron emission of metals[J]. Physica, 1938, 5(1): 17-30.
- [7] Ushio Y, et al. Secondary electron emission studies on MgO films[J]. Thin Solid Films, 1988, 167(1-2): 299-308.
- [8] Jokela S J, et al. Secondary Electron Yield of Emissive Materials for Large-Area Micro-Channel Plate Detectors: Surface Composition and Film Thickness Dependencies[J]. Physics Procedia, 2012, 37: 740-747.
- [9] Olano L, Montero I. Energy spectra of secondary electrons in dielectric materials by charging analysis[J/OL]. Results in Physics, 2020, 19: 103456. <https://www.sciencedirect.com/science/article/pii/S2211379720319173>. DOI: <https://doi.org/10.1016/j.rinp.2020.103456>.
- [10] Mane A U, et al. An Atomic Layer Deposition Method to Fabricate Economical and Robust Large Area Microchannel Plates for Photodetectors[J]. Physics Procedia, 2012, 37: 722-732.
- [11] Guo L, et al. Effects of secondary electron emission yield properties on gain and timing performance of ALD-coated MCP[J]. Nucl. Instrum. Meth. A, 2021, 1005: 165369.
- [12] Nathan R, Mee C. The energy distribution of photoelectrons from the K<sub>2</sub>CsSb photocathode [J/OL]. physica status solidi (a), 1970, 2(1): 67-72. <https://api.semanticscholar.org/CorpusID:97164824>.
- [13] Zhu Y, et al. The mass production and batch test result of 20" MCP-PMTs[J/OL]. Nucl. Instrum. Meth. A, 2020, 952: 162002. <https://www.sciencedirect.com/science/article/pii/S0168900219303833>. DOI: <https://doi.org/10.1016/j.nima.2019.03.057>.
- [14] Zhang A, et al. Performance evaluation of the 8-inch MCP-PMT for Jinping Neutrino Experiment[J/OL]. Nucl. Instrum. Meth. A, 2023, 1055: 168506. DOI: [10.1016/j.nima.2023.168506](https://doi.org/10.1016/j.nima.2023.168506).

---

## REFERENCES

---

- [15] Matsuoka K. Development and production of the MCP-PMT for the Belle II TOP counter[J/OL]. Nucl. Instrum. Meth. A, 2014, 766: 148-151. <https://www.sciencedirect.com/science/article/pii/S0168900214005026>. DOI: <https://doi.org/10.1016/j.nima.2014.05.003>.
- [16] Krauss S, et al. Performance of the most recent Microchannel-Plate PMTs for the PANDA DIRC detectors at FAIR[J/OL]. Nucl. Instrum. Meth. A, 2023, 1057: 168659. <https://www.sciencedirect.com/science/article/pii/S0168900223006496>. DOI: <https://doi.org/10.1016/j.nima.2023.168659>.
- [17] Cao Z, et al. Upgrading Plan Towards Multi-messenger Observation with LHAASO[J/OL]. EPJ Web of Conferences, 2019. <https://api.semanticscholar.org/CorpusID:181399433>.
- [18] Kishimoto N, et al. Lifetime of MCP-PMT[J/OL]. Nucl. Instrum. Meth. A, 2006, 564(1): 204-211. <https://www.sciencedirect.com/science/article/pii/S0168900206006991>. DOI: <https://doi.org/10.1016/j.nima.2006.04.089>.
- [19] Lehmann A, et al. Latest Technological Advances with MCP-PMTs[J]. J. Phys.: Conf. Ser., 2022, 2374(1): 012128.
- [20] Cao W, et al. Secondary electron emission characteristics of the Al<sub>2</sub>O<sub>3</sub>/MgO double-layer structure prepared by atomic layer deposition[J/OL]. Ceramics International, 2021, 47(7): 9866-9872. DOI: [10.1016/j.ceramint.2020.12.128](https://doi.org/10.1016/j.ceramint.2020.12.128).
- [21] Zhang Z, et al. Effect of Al<sub>2</sub>O<sub>3</sub>/MgO Composite Layer on the Properties of Microchannel Plate [J]. Surface Technology, 2021, 50(6): 199-205.
- [22] Abusleme A, et al. Mass testing and characterization of 20-inch PMTs for JUNO[J]. The European Physical Journal C, 2022, 82(12): 1168.
- [23] Orlov D, et al. High collection efficiency MCPs for photon counting detectors[J/OL]. JINST, 2018, 13(01): C01047. DOI: [10.1088/1748-0221/13/01/C01047](https://doi.org/10.1088/1748-0221/13/01/C01047).
- [24] Zhang H, et al. Gain and charge response of 20" MCP and dynode PMTs[J]. JINST, 2021, 16 (08): T08009.
- [25] Yang Y, et al. MCP performance improvement using alumina thin film[J]. Nucl. Instrum. Meth. A, 2017, 868: 43-47.
- [26] Tan H H. A statistical model of the photomultiplier gain process with applications to optical pulse detection[J/OL]. The Telecommunications and Data Acquisition Report, 1982. <http://hdl.handle.net/10150/612894>.
- [27] Bartlett M S, Harris T E. The Theory of Branching Processes[M/OL]. Springer Berlin, 1963. <https://api.semanticscholar.org/CorpusID:90485223>.
- [28] Woodward P M. A statistical theory of cascade multiplication[J/OL]. Mathematical Proceedings of the Cambridge Philosophical Society, 1948, 44(3): 404-412. DOI: [10.1017/S0305004100024403](https://doi.org/10.1017/S0305004100024403).
- [29] Prescott J. A statistical model for photomultiplier single-electron statistics[J]. Nuclear Instruments and Methods, 1966, 39(1): 173-179.
- [30] Kalousis L. Calibration of the Double Chooz detector and cosmic background studies[D]. University of Strasbourg, 2012.

---

## REFERENCES

---

- [31] Kalousis L, et al. A fast numerical method for photomultiplier tube calibration[J]. JINST, 2020, 15(03): P03023.
- [32] Bruining H. Physics and applications of secondary electron emission[M]. Pergamon Press, 1954.
- [33] Baroody E. A theory of secondary electron emission from metals[J]. Physical Review, 1950, 78(6): 780.
- [34] Dekker A, Van der Ziel A. Theory of the production of secondary electrons in solids[J]. Physical Review, 1952, 86(5): 755.
- [35] Wolff P A. Theory of secondary electron cascade in metals[J/OL]. Phys. Rev., 1954, 95: 56-66. <https://link.aps.org/doi/10.1103/PhysRev.95.56>.
- [36] Kanaya K, et al. Secondary electron emission from insulators[J/OL]. J. Phys. D: Appl. Phys., 1978, 11(17): 2425. <https://dx.doi.org/10.1088/0022-3727/11/17/015>.
- [37] Vaughan J. A new formula for secondary emission yield[J/OL]. IEEE Transactions on Electron Devices, 1989, 36(9): 1963-1967. DOI: 10.1109/16.34278.
- [38] Luo F J, et al. Design & Optimization of the HV divider for JUNO 20-inch PMT[A]. 2023.
- [39] Nelson, Rick. High-Definition Oscilloscopes Optimize Vertical Resolution[J/OL]. EE-Evaluation Engineering Online, 2016[Aug. 31, 2016]. <https://www.electronicdesign.com/technologies/test-measurement/article/21206728/high-definition-oscilloscopes-optimize-vertical-resolution>.
- [40] Xu D, et al. Towards the ultimate PMT waveform analysis for neutrino and dark matter experiments[J/OL]. JINST, 2022, 17(06): P06040. <https://dx.doi.org/10.1088/1748-0221/17/06/P06040>.
- [41] Wang Y, et al. The Fast Stochastic Matching Pursuit for Neutrino and Dark Matter Experiments [A]. 2024. arXiv: 2403.03156.
- [42] Gagunashvili N D. Comparison of weighted and unweighted histograms[J]. Statistics, 2012: 43-44.
- [43] Gelman A, Hill J. Analytical methods for social research: Data Analysis Using Regression and Multilevel/Hierarchical Models[M]. Cambridge University Press, 2006.
- [44] Cowan G. Statistical Data Analysis[M]. Illustrated edition ed. Oxford: New York: Oxford University Press, 1997.
- [45] Chen P, et al. Photoelectron backscattering in the microchannel plate photomultiplier tube[J]. Nucl. Instrum. Meth. A, 2018, 912: 112-114.
- [46] Beck A H. Physical Electronics: Handbook of Vacuum Physics[M]. Elsevier, 1966.
- [47] Jorgensen B. The Theory of Dispersion Models[M/OL]. Taylor & Francis, 1997. [https://books.google.co.jp/books?id=0gO7bgs\\_eSYC](https://books.google.co.jp/books?id=0gO7bgs_eSYC).
- [48] Fukuda S, Y. Fukuda E I, T. Hayakawa, et al. The Super-Kamiokande detector[J/OL]. Nucl. Instrum. Meth. A, 2003, 501(2): 418-462. <https://www.sciencedirect.com/science/article/pii/S016890020300425X>. DOI: [https://doi.org/10.1016/S0168-9002\(03\)00425-X](https://doi.org/10.1016/S0168-9002(03)00425-X).

---

## REFERENCES

---

- [49] Patterson R, Laird E, Liu Y, et al. The extended-track event reconstruction for MiniBooNE [J/OL]. Nucl. Instrum. Meth. A, 2009, 608(1): 206-224. <https://www.sciencedirect.com/science/article/pii/S0168900209012480>. DOI: <https://doi.org/10.1016/j.nima.2009.06.064>.
- [50] Jiang M, Abe K, Bronner, et al. Atmospheric neutrino oscillation analysis with improved event reconstruction in Super-Kamiokande IV[J/OL]. Progress of Theoretical and Experimental Physics, 2019, 2019(5): 053F01. <https://doi.org/10.1093/ptep/ptz015>.
- [51] Liu X, Dou W, Xu B, et al. First-principle event reconstruction by time-charge readouts for TAO [J/OL]. Eur. Phys. J. C, 2025, 85(4): 438. DOI: 10.1140/epjc/s10052-025-14161-6.
- [52] Yu P, et al. Multi-threaded Simulation Software for the JUNO Experiment[A]. 2025. arXiv: 2503.20219.
- [53] Dou W, Xu B, Zhou J, et al. Reconstruction of point events in liquid-scintillator detectors subjected to total internal reflection[J/OL]. Nucl. Instrum. Meth. A, 2023, 1057: 168692. DOI: 10.1016/j.nima.2023.168692.
- [54] Lele S R, Dennis B, Lutscher F. Data cloning: easy maximum likelihood estimation for complex ecological models using Bayesian Markov chain Monte Carlo methods[J]. Ecology Letters, 2007, 10(7).
- [55] Shiozawa M. Reconstruction algorithms in the Super-Kamiokande large water Cherenkov detector[J/OL]. Nucl. Instrum. Meth. A, 1999, 433(1): 240-246. <https://www.sciencedirect.com/science/article/pii/S0168900299003599>. DOI: [https://doi.org/10.1016/S0168-9002\(99\)00359-9](https://doi.org/10.1016/S0168-9002(99)00359-9).
- [56] David P, Buckley T R. Model Selection and Model Averaging in Phylogenetics: Advantages of Akaike Information Criterion and Bayesian Approaches Over Likelihood Ratio Tests[J]. Systematic Biology, 2004(5): 793-808.
- [57] Abe K, et al. Solar Neutrino Measurements in Super-Kamiokande-IV[J/OL]. Phys. Rev. D, 2016, 94: 052010. <https://link.aps.org/doi/10.1103/PhysRevD.94.052010>.
- [58] Abe K, et al. Solar neutrino results in Super-Kamiokande-III[J/OL]. Phys. Rev. D, 2011, 83: 052010. <https://link.aps.org/doi/10.1103/PhysRevD.83.052010>.
- [59] JUNO physics and detector[J/OL]. Progress in Particle and Nuclear Physics, 2022, 123: 103927. <https://www.sciencedirect.com/science/article/pii/S0146641021000880>. DOI: <https://doi.org/10.1016/j.ppnp.2021.103927>.
- [60] Shinoki M, et al. Measurement of the cosmogenic neutron yield in Super-Kamiokande with gadolinium loaded water[J/OL]. Phys. Rev. D, 2023, 107(9): 092009. DOI: 10.1103/PhysRevD.107.092009.
- [61] Aharmim B, Ahmed S N, et al. Cosmogenic neutron production at the Sudbury Neutrino Observatory[J/OL]. Phys. Rev. D, 2019, 100: 112005. <https://link.aps.org/doi/10.1103/PhysRevD.100.112005>.
- [62] Wang Y F, Balic V, Gratta G, et al. Predicting neutron production from cosmic-ray muons[J/OL]. Phys. Rev. D, 2001, 64: 013012. <https://link.aps.org/doi/10.1103/PhysRevD.64.013012>.
- [63] Hertenberger R, Chen M, Dougherty B L. Muon-induced neutron and pion production in an organic liquid scintillator at a shallow depth[J/OL]. Phys. Rev. C, 1995, 52: 3449-3459. <https://link.aps.org/doi/10.1103/PhysRevC.52.3449>.

---

## REFERENCES

---

- [64] Boehm F, Busenitz J, Cook B, et al. Neutron production by cosmic-ray muons at shallow depth [J/OL]. *Phys. Rev. D*, 2000, 62: 092005. <https://link.aps.org/doi/10.1103/PhysRevD.62.092005>.
- [65] An F P, Balantekin A B, et al. Cosmogenic neutron production at Daya Bay[J/OL]. *Phys. Rev. D*, 2018, 97: 052009. <https://link.aps.org/doi/10.1103/PhysRevD.97.052009>.
- [66] Blyth S C, Chan Y L, Chen X C, et al. Measurement of cosmic-ray muons and muon-induced neutrons in the Aberdeen Tunnel Underground Laboratory[J/OL]. *Phys. Rev. D*, 2016, 93: 072005. <https://link.aps.org/doi/10.1103/PhysRevD.93.072005>.
- [67] Abe S, Enomoto S, Furuno K, et al. Production of radioactive isotopes through cosmic muon spallation in KamLAND[J/OL]. *Phys. Rev. C*, 2010, 81: 025807. <https://link.aps.org/doi/10.1103/PhysRevC.81.025807>.
- [68] Bellini G, Benziger J, Bick D, et al. Cosmogenic Backgrounds in Borexino at 3800 m water-equivalent depth[J/OL]. *Journal of Cosmology and Astroparticle Physics*, 2013, 2013(08): 049. <https://dx.doi.org/10.1088/1475-7516/2013/08/049>.
- [69] Zhang X, Li J, Chen S, et al. Study of neutron production for 360 gev cosmic muons[J/OL]. *Phys. Rev. D*, 2024, 110: 112017. <https://link.aps.org/doi/10.1103/PhysRevD.110.112017>.
- [70] Araújo H, Kudryavtsev V, Spooner N, et al. Muon-induced neutron production and detection with GEANT4 and FLUKA[J/OL]. *Nuclear Instruments and Methods in Physics Research Section A: Accelerators, Spectrometers, Detectors and Associated Equipment*, 2005, 545 (1): 398-411. <https://www.sciencedirect.com/science/article/pii/S0168900205005838>. DOI: <https://doi.org/10.1016/j.nima.2005.02.004>.
- [71] Mei D M, Hime A. Muon-induced background study for underground laboratories[J/OL]. *Phys. Rev. D*, 2006, 73: 053004. <https://link.aps.org/doi/10.1103/PhysRevD.73.053004>.
- [72] Kudryavtsev V, Spooner N, McMillan J. Simulations of muon-induced neutron flux at large depths underground[J/OL]. *Nuclear Instruments and Methods in Physics Research Section A: Accelerators, Spectrometers, Detectors and Associated Equipment*, 2003, 505(3): 688-698. <https://www.sciencedirect.com/science/article/pii/S0168900203009835>. DOI: [https://doi.org/10.1016/S0168-9002\(03\)00983-5](https://doi.org/10.1016/S0168-9002(03)00983-5).
- [73] Collaboration† K, Aker M, Batzler D, et al. Direct neutrino-mass measurement based on 259 days of katrin data[J/OL]. *Science*, 2025, 388(6743): 180-185. <https://www.science.org/doi/abs/10.1126/science.adq9592>.
- [74] Li S W, Beacom J F. First calculation of cosmic-ray muon spallation backgrounds for MeV astrophysical neutrino signals in Super-Kamiokande[J/OL]. *Phys. Rev. C*, 2014, 89: 045801. <https://link.aps.org/doi/10.1103/PhysRevC.89.045801>.